2011

Passive Wireless Saw Sensors With New And Novel Reflector Structures Design And Applications

Nikolai Kozlovski
University of Central Florida

Passive Wireless Saw Sensors with New and Novel Reflector Structures: Design and Applications

by

Nikolai Yurevich Kozlovski
B.S. University of Central Florida, 2004
M.S. University of Central Florida, 2006

A dissertation submitted in partial fulfillment of the requirements
for the degree of Doctor of Philosophy
in the Department of Electrical and Computer Engineering
in the College of Engineering and Computer Science
at the University of Central Florida
Orlando, Florida

Spring Term
2011

Major Professor: Arthur R. Weeks

ABSTRACT

Surface acoustic wave (SAW) devices are a solution for today's ever growing need for passive wireless sensors. Orthogonal frequency coding (OFC) together with time division multiplexing (TDM) provides a large number of codes and coding algorithms producing devices that have excellent collision properties. Novel SAW noise-like reflector (NLR) structures with pulse position modulation (PPM) are shown to exhibit good auto- and cross-correlation, and anti-collision properties.

Multi-track, multi-transducer approaches yield devices with adjustable input impedances and enhanced collision properties for OFC TDM SAW sensor devices. Each track-transducer is designed for optimum performance for loss, coding, and chip reflectivity. Experimental results and theoretical predictions confirm a constant Q for SAW transducers for a given operational bandwidth, independent of device and transducer embodiment.

Results on these new NLR SAW structures and devices along with a new novel 915 MHz transceiver based on a software radio approach was designed, built, and analyzed. Passive wireless SAW temperature sensors were interrogated and demodulated in a spread spectrum correlator system using a new adaptive filter. The first-ever SAW OFC four-sensor operation was demonstrated at a distance of 1 meter and a single sensor was shown to operate up to 3 meters. Comments on future work and directions are also presented.

Dedicated to my wife, Evgenia, and our son, Andrew.

ACKNOWLEDGMENTS

First, I would like to thank my wife, Evgenia, and our son, Andrew, for their patience with an absent husband and father, especially during past two years. I thank them for letting me pursue my academic and career goals. I love you both for understanding and support.

It has been a truly great privilege to work with Dr. Donald C. Malocha. I would like to thank him for providing me with guidance and encouragement during my graduate studies at University of Central Florida. He gave me every opportunity to become a better engineer.

This work would not be possible without the support of my colleagues at the Consortium for Applied Acoustoelectronic Technology. In particular, I would like to thank N. Saldanha, D. Gallagher, M. Gallagher and former colleague, D. Puccio.

It is my pleasure to thank the committee for their support, especially, Dr. Arthur Weeks for his help with the system and proofreading countless revisions of my papers and the dissertation.

I would like to thank NASA and Dr. Youngquist for supporting me and our group financially. I thank Mnemonics Inc, especially Madjid Belkerdid and TJ Mears, for their help with the final prototype of the system.

Finally, I owe my gratitude to my parents and the extended family for their love and support. I have come a long way and you have always been there for me.

TABLE OF CONTENTS

LIST OF FIGURES

LIST OF TABLES

LIST OF ACRONYMS

AWGN	—	Additive White Gaussian Noise
BAW	—	Bulk Acoustic Wave
BPF	—	Band-pass Filter
CDMA	—	Code Division Multiple Access
COM	—	Coupling of Modes
IDT	—	Interdigital Transducer
IF	—	Intermediate Frequency
IL	—	Insertion Loss
$LiNbO_3$	—	Lithium Niobate
$LiTaO_3$	—	Lithium Tantalate
LO	—	Local Oscillator
MCAR	—	Cross-correlation-to-auto-correlation Ratio
MDS	—	Minimum Detectable Signal
NLR	—	Noise-like Reflector
OFC	—	Orthogonal frequency coding
PN	—	Pseudo-noise
PPM	—	Pulse Position Modulation
Q (factor)	—	Quality (factor)
RF	—	Radio-frequency
RFID	—	Radio-frequency Identification
RND	—	Random
SAW	—	Surface Acoustic Wave
SNR	—	Signal-to-noise Ratio
TCD	—	Temperature Coefficient of Delay
TDM	—	Time Division Multiplexing
TDMA	—	Time Division Multiple Access
UWB	—	Ultra-wide Band

CHAPTER 1
INTRODUCTION

Surface acoustic wave (SAW) sensors have been gaining popularity in the past several years. Various sensors embodiments have been studied to measure physical properties, such as temperature, pressure, and strain, as well as chemical and biological elements [1, 2, 3, 4]. The SAW sensors often offer unique properties such as passive, wireless operation as well as being radiation hard. This thesis will present the first results for an operational spread spectrum SAW sensor system. The research is based on the use of SAW device coding for an RFID tag and an adaptive filter for temperature extraction in a correlator receiver. Novel SAW device coding, analysis and configurations will be shown. Experimental results of various SAW structures and system performance parameters will be given.

The principles of operation of the basic SAW elements are discussed in Chapter 2. This chapter also provides an overview of current competing technologies. Orthogonal frequency coding (OFC) is used in the design of the devices used in this dissertation [5] and fundamentals and advantages are presented. Sensitivity to ex-

ternal stimuli presents itself as a change in surface wave velocity, which results in frequency and time domain scaling of the device response. A matched filter approach for extracting the velocity change is discussed in this chapter.

Modeling is a very important step in the product development cycle. Chapter 3 presents two models; the synthesis model, used for just the SAW transducer design and the coupling of modes model that accounts for various second order effects [6, 7, 8]. Both models use a hybrid matrix approach to represent the device. These matrices can then be used to build up a signal flow graph of the entire device, which can then be solved using primarily Mason's gain formula [9]. This approach is discussed in detail and also demonstrates the approach used for modeling apodized and multi-track devices.

Unlike with powered sensors, passive sensors are unable to adjust the amount of the return energy or turn off and on again transmission of the signal in order to avoid collisions with other sensors. Chapter 4 discusses device coding requirements and provides coding techniques that yield systems with high code diversity and low multi-device collisions. This chapter presents noise like reflector structures (NLR) as well as OFC approaches to device coding. A technique is demonstrated using OFC and TDM that yields a multi-device system with excellent collision properties.

Inter-device reflections and antenna impedance matching are addressed in Chapter 5. Multi-track, multi-transducer embodiments acoustically separate SAW elements within the device which results in reduced inter reflections. Using various transducer configurations, the input impedance of the sensor can be tuned to conjugately match the antennas impedance resulting in reduced mismatch losses.

Chapter 6 presents an operational 915 MHz OFC SAW sensor interrogator system. A module-by-module discussion of the transceiver is provided and key system parameters are discussed. Also, implemented OFC sensors are presented along with their key parameters. This chapter provides range-noise analysis and multi-sensor operation is demonstrated with four simultaneously interrogated sensors.

Finally, Chapter 7 will list important conclusions and will discuss possible areas of future OFC SAW sensor research.

CHAPTER 2
BACKGROUND

2.1 Surface Acoustic Wave Principles

Piezoelectricity was discovered in 1880 by two brothers, Pierre and Paul-Jacques Curie, and was named by Wilhelm Hankel in 1881 [10]. Surface acoustic wave (SAW) was first studied and modeled by Lord Rayleigh in 1885 [11]. In his paper, he described the surface acoustic wave (mode) of propagation and its properties. Shown in Figure 2.1 is a schematic representation of a Rayleigh wave (SAW). For the wave propagating left to right, motion of the molecule at the surface of the substrate is counterclockwise.

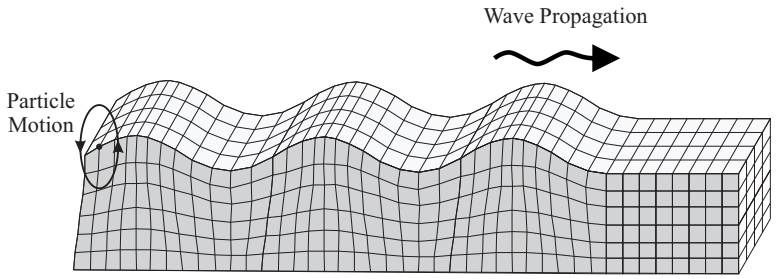

Figure 2.1: Schematic representation of a Rayleigh wave (SAW), circle indicates the direction of motion of the individual molecules of the substrate.

An interdigital transducer (IDT) was invented by White and Voltmer, and in 1965 they demonstrated the first SAW delay line filter [12]. Shown in Figure 2.2(a) is a schematic drawing of a SAW IDT. A RF signal applied to the IDT will warp the piezoelectric material underneath. As the input RF signal alternates, the SAW waves are generated. If the period of the input RF signal is equal to the time it takes a SAW to travel under one period of the transducer, the generated surface waves will add in phase and propagate out of the acoustical ports of the transducer; otherwise, the waves will add out of phase and will be attenuated [12]. Principle of the SAW IDT operation is depicted in Figure 2.2(b).

Another important SAW element is a reflector grating (Bragg reflector) [13]. The Bragg reflector was first used in optics and it consisted of multiple layers of various materials with varying refractive index. Depending on the layers thickness, periodicity and the refractive index, light of some wavelengths would go through and another would reflect [14]. The concept of Bragg reflectivity has been applied to

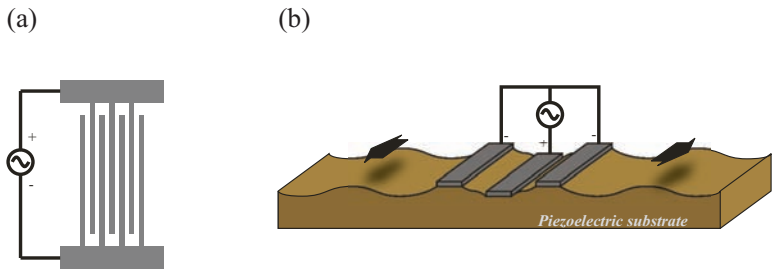

Figure 2.2: (a) Schematic representation of SAW IDT and (b) principle of operation of the IDT (b).

SAW devices and was implemented via periodic structures (i.e. metallic structures) as shown in Figure 2.3(a) [15]. Part of the forward traveling wave is reflected at each edge of each electrode of the reflector grating. If the period of the reflector grating is an integer multiple of the wavelength of the forward traveling wave, the reflectivity at the wavelength (frequency) will be maximum. For an off-frequency wave reflection will be attenuated or none at all and the wave will pass underneath the reflector grating with little loss.

What makes SAW devices so attractive is that their typical free surface velocity is on the order of $3 \times 10^3 \frac{m}{s}$, compared to free space velocity of approximately $3 \times 10^8 \frac{m}{s}$, which yields a factor of 10^5 difference in wavelength and device implementation using SAW versus micro-strip lines, at frequencies between 70 MHz and 2.5 GHz. The key parameters of piezoelectric substrates is the free surface velocity, coupling coefficient, which determines how well electrical energy is coupled into mechanical

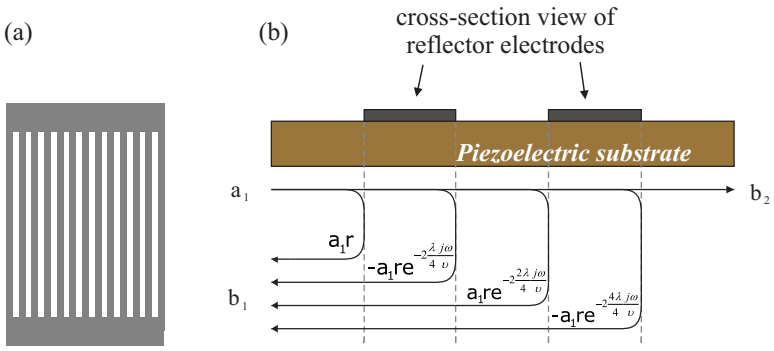

Figure 2.3: (a) Schematic drawing of SAW reflector grating and (b) principle of operation of the grating (b).

energy and back, temperature sensitivity, and maximum temperature of operation. Most common substrates and their parameters are given in Table 2.1. One can note that for temperature sensor applications up to 350°C Y,Z $LiNbO_3$offers good sensitivity and high coupling. For temperatures higher than 350°C one might choose Y,X langasite. For tag applications or sensors other than temperature one might choose quartz; however, low coupling would yield devices with higher loss or narrower operational bandwidth.

2.2 Sensor Field

The topic of sensors is becoming more and more popular. Sensors can make machines more robust, safe and efficient. Sensors can also make human interaction with

Table 2.1: Common piezoelectric substrates for use with SAW devices and their key parameters [16].

Material Name	**Crystal Cut**	**Coupling Coefficient**	**Temperature Sensitivity**	**SAW Velocity**	**Maximum Temperature**
$LiNbO_3$	Y,Z	4.6%	94 ppm/°C	3488 m/s	$\sim$ 350°C
$LiNbO_3$	128°Y,X	5.6%	72 ppm/°C	3992 m/s	$\sim$ 350°C
$LiTaO_3$	Y,Z	0.74%	35 ppm/°C	3230 m/s	$\sim$ 350°C
Quartz	ST	0.16%	0 ppm/°C	3152 m/s	570°C
Langasite	Y,X	0.37%	38 ppm/°C	2330 m/s	$>$ 1000°C
Langasite	138°Y,26°X	0.34%	$\sim$ 0 ppm/°C	2743 m/s	$>$ 1000°C

electronic devices more intuitive and friendly; today, a smart phone can have over 10 sensors. While for certain applications list of commercially available sensors is quite extensive, some requirements such as being passive, wireless, radiation hard, and able to work in high or cryogenic temperatures can quickly narrow down the number of viable solutions to none.

Sensors can be divided into two major groups: wired and wireless. The wireless group can then be further divided into following most popular subgroups: battery powered, energy harvesting, passive resonant, passive SAW delay line, and passive RFID based sensors.

Battery powered senors typically use resistive sensing elements. An active element reads the sensor output and transmits it via wireless interface. One of the popular battery power sensors is an outdoor temperature sensor for weather stations shown in Figure 2.4(a). Another type of wireless sensor is energy harvesting sensor. Typically, such sensor operates via conversing of chemical, thermal, mechanical, fluidic motion, electromagnetic, or optical energy into electrical energy. Shown in Figure 2.4(b) is a passive wireless switch developed by EnOcean, that converts mechanical energy of flipped switch into electrical energy that is enough to send a signal to the lamp controlled by the switch. A major drawback of these two types of sensors is that

they are typically expensive, they are not radiation hard, they have high number of possible failure points, and cannot operate under extreme temperatures.

Passive wireless sensors resonance-based are currently available on the market. They are typically implemented using micro-strip networks, SAW or BAW devices [17, 18]. The reader for the resonant sensors will typically emit a high power CW signal, which will cause the sensor to start ringing. Once the CW is turned off, the sensor's output frequency is recorded. Change in the measured frequency is a function of the frequency or other desired parameter. While being suitable for some applications, their drawbacks include lack of security and coding, typically small range due to closed loop gain requirements, and high sensitivity to noise and multi-path. A schematic drawing of a passive wireless resonance-based SAW sensor is given

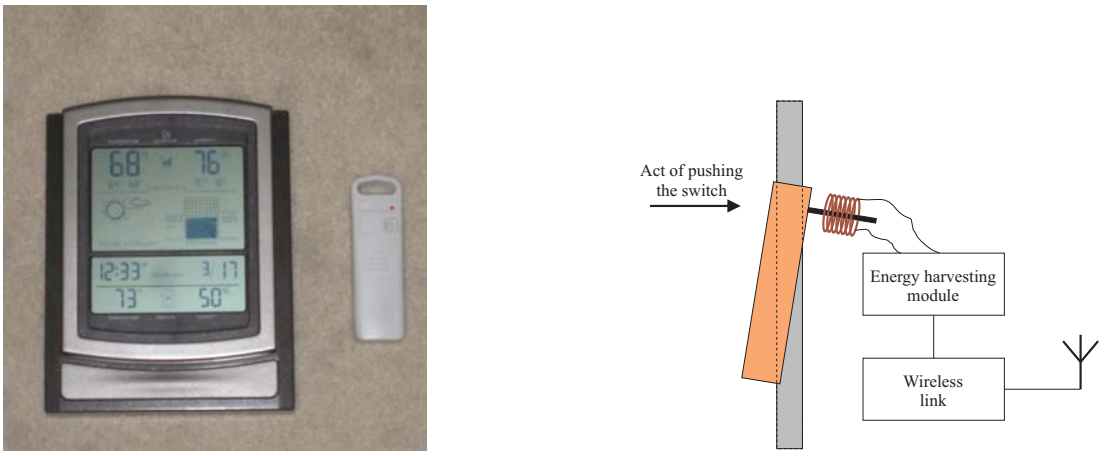

(a) (b)

Figure 2.4: Examples of (a) battery powered and (b) energy harvesting sensors (energy harvesting wireless on-off switch).

in Figure 2.5(a). A delay line based SAW sensor is shown in Figure 2.5(b). The SAW delay line itself acts as a wireless platform with an antenna attached to one port of the delay and a sensing load to the second port. The sensing load changes amplitude and phase of the device response [19, 20]. While sensitivity to noise and multi-path issues can be reduced using chirped transducers, lack of coding and low accuracy of reading make this approach impractical for some applications. Passive wireless TDMA and CDMA SAW approaches will be discussed in following section.

2.2.1 CDMA and TDMA Surface Acoustic Wave Sensors

In recent years, passive wireless SAW-based sensors started to become a viable solution for todays demanding sensing applications. The use of SAW delay line sensors

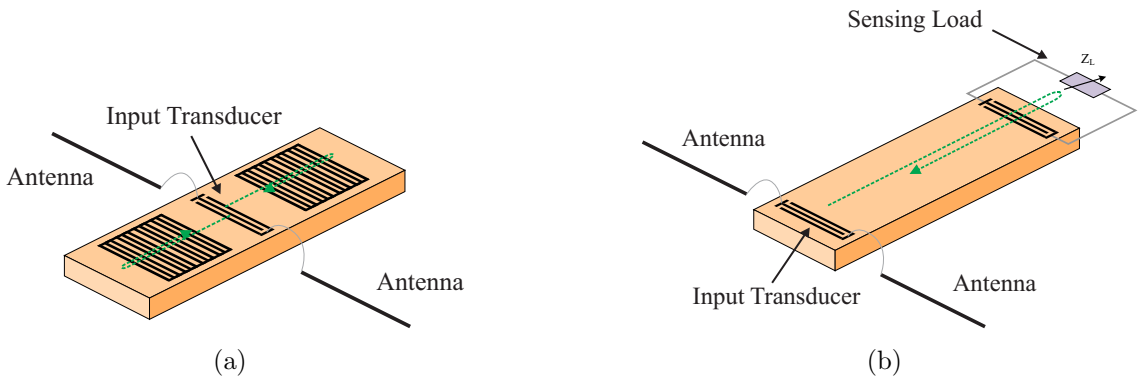

Figure 2.5: Schematic drawings of a passive wireless SAW (a) resonance and (b) delay line sensors.

have been previously reported in the literature, with various system performance results [21, 22, 23, 24, 25, 26, 27]. CDMA, TDMA and OFC sensors have also been discussed and can be grouped in the class of spread spectrum signaling formats that provide coding for RF identification [28, 29, 26, 30, 27].

As a background, the most common approach to SAW RFID tags use a code division multiple access (CDMA) approach, with the device schematic shown in Fig. 2.6. In principle, the device is excited with a single carrier RF burst that generates a surface wave that propagates to the reflectors, which then is partially reflected from each of the in-line, unweighted reflectors. An amplitude shift keying (ASK) or phase shift keying (PSK) receiver can be used with this device in order to determine the reflected pulse locations that indicate the device code and/or the sensed information [4, 26, 20, 31, 25]. Alternatively, tag identification and sensor readout can be accomplished by applying the tag response to a matched filter based on the bit locations and phases [23, 32].

The desired impulse response is a series of reflected pulses with time locations corresponding to the physical locations of the reflectors. Typical SAW CDMA devices used for RFID have 30-60 dB insertion loss (IL) due to use of single frequency Bragg reflectors having low reflectivity per chip that minimize distortion effects[31].

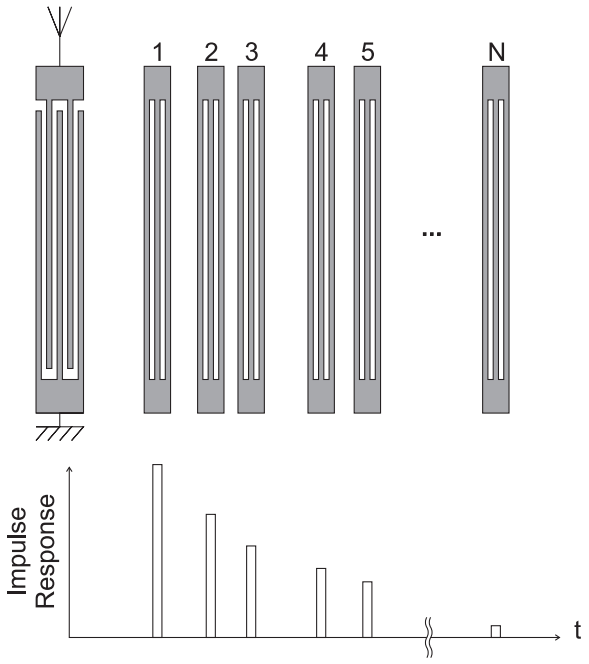

Figure 2.6: Schematic drawing and impulse response of single frequency SAW ID tag, all reflector gratings are in one track besides the input transducer.

SAW-based sensors and tags offer a wide range of advantages over alternative technologies. They can be designed to operate wirelessly which reduces the need of having wires, which is especially important when monitoring moving and or rotating parts. Passive SAW devices enable long term, operation in applications when battery replacement is impossible such as monitoring concrete and fiber glass structures internally. SAW devices are also radiation hard (EM and gamma), which enables them to be used in space applications. While SAW-based sensors might experience temporary glitches, silicon based devices and MEMS will be permanently damaged when exposed to such radiation. Fabrication cost of SAW devices is significantly lower when compared to complex MEMS devices at present state. Operation at extreme temperatures (from cryo to >1000°C) is also one of the advantages of SAW based devices over silicon based.

2.3 Orthogonal Frequency Coding

2.3.1 Principles

Two finite time length functions are called orthogonal if their cross correlation at time $t = 0$ is zero as

$$\int_{\tau_1}^{\tau_2} h(t) \cdot g(t)\, dt = 0, \tag{2.1}$$

where $h(t)$ and $h(t)$ are the two orthogonal functions. For uniform reflectors, whose ideal frequency domain impulse responses can be represented as a sampling function, the orthogonality rule of Equation 2.1 yields reflector responses whose peaks in frequency domain coincide with nulls of their respective orthogonal reflectors as shown in Figure 2.7. All OFC reflectors of the same set have constant time response length. Mathematically, relationship between OFC reflector time response length and their frequencies is expressed as

$$f_k = f_0 + \frac{N}{\tau_c}, \tag{2.2}$$

where f_0 is the center frequency of the first OFC reflector, f_k is the center frequency of the k^{th} OFC reflector ($k > 0$), τ_c is response time length of the reflector, and N positive integer number. It is also important to note that product $f_i \cdot \tau_c$ is an integer number that corresponds to number of electrodes in the k^{th} reflector.

The orthogonality rule ensures that each reflector is transparent to all other reflectors at their center frequencies.

A schematic of an OFC RFID tag with 7 chips, each having a different Bragg frequency, is shown in Fig. 2.8. The multi-frequency OFC chip reflectors are nearly transparent outside their Bragg frequency, allowing low loss (<10 dB) and reduced second order effects. OFC easily operates ultra-wide-band (UWB) and needs only a few chips for most sensor applications.

OFC has many code combinations with relatively few chips because of the possibility of using both frequency and PN coding. As an example, a OFC device with 8 chips has an equivalent number of possible codes as a 23-chip, PN-CDMA device [33]. For commercial tagging applications, large codes are necessary, however, sensor applications usually require a much smaller code set and 4 to 8 chips may be sufficient. Work has been previously published on passive wireless OFC SAW sensors [34, 35, 5, 33].

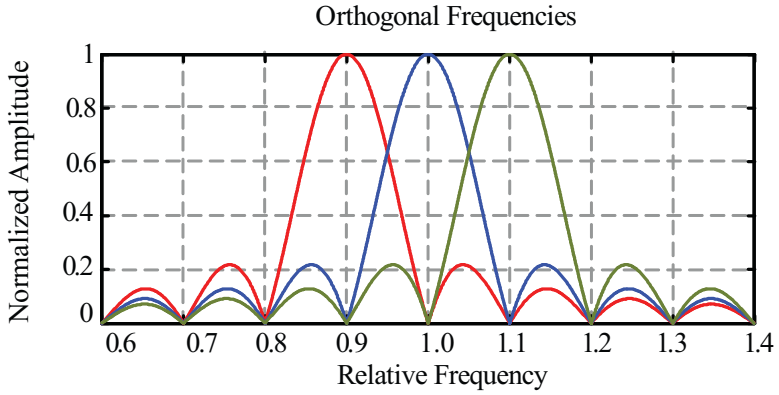

Figure 2.7: Ideal frequency domain impulse response of the OFC reflectors of the consecutive frequencies f_1, f_2, and f_3 shown in red, blue and green respectively.

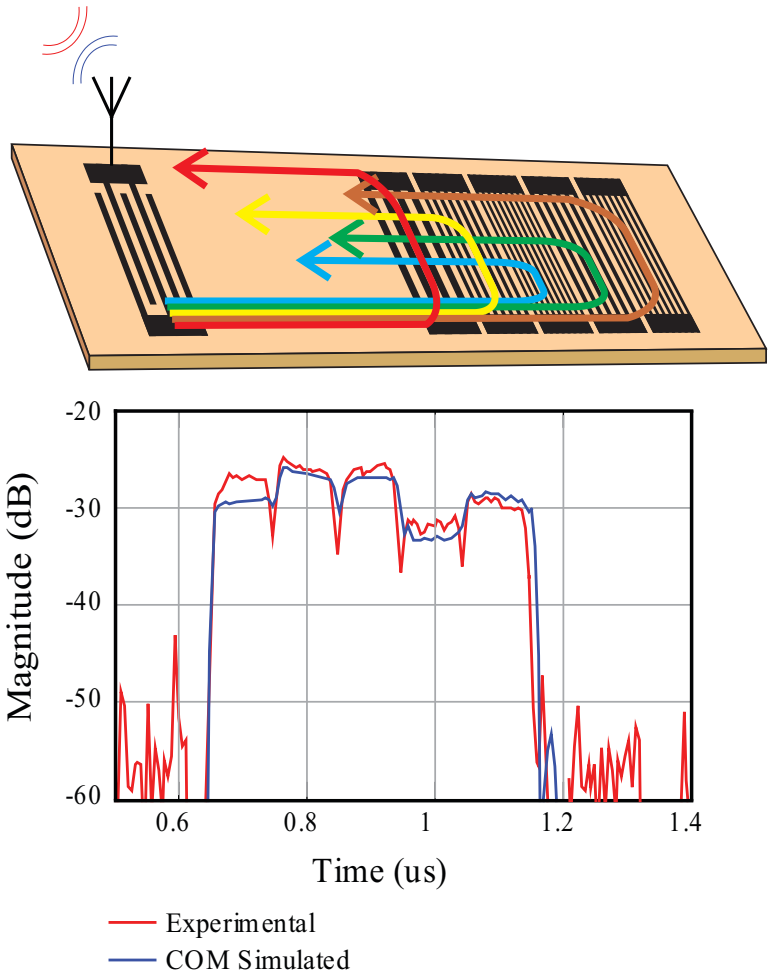

Figure 2.8: Sample single-sided SAW sensor with 7 OFC chips.

2.3.2 Ideal SAW Reflector Response Model

Once reflector structures are physically defined, mapping from physical dimensions to time domain is performed and Equations 2.3 through 2.5 are applied to produce simple model prediction of time and frequency responses. The following equations determine the ideal reflector response model given the reflector definitions, as

$$f_k = \frac{v}{p_k}, \tag{2.3}$$

$$\tau_{c_k} = 2\frac{p_k}{v}, \tag{2.4}$$

where f_k is the center frequency of the k^{th} reflector, τ_{c_k} is the impulse response length of the k^{th} reflector, v is the SAW velocity, and p_k is the electrode-gap width (typically half-wavelength) of the k^{th} reflector

$$\tau_{p_k} = 2\frac{x_k}{v}, \tag{2.5}$$

where x_k is additional spacing between k^{th} and $(k-1)^{th}$ reflectors. In the case of a reflector, τ_{c_k} and τ_{p_k} are double of the physical dimension calculated delay since this

is a round trip reflection. Once mapping from physical dimensions into time domain is completed, and the ideal reflector response is calculated as

$$\tau_{pos_1} = \tau_{p_1}, \tag{2.6}$$

$$\tau_{pos_k} = \sum_{i=1}^{k-1} (\tau_{c_i} + \tau_{p_i}) + \tau_{p_i} \quad for \quad k = 2, 3, 4, ..., \tag{2.7}$$

where τ_{pos_k} is the position of the k^{th} reflector with respect to the start of the first reflector of the array. The time domain response is then defined as

$$h(t) = \sum_{k=1}^{N} Sin\left(2\pi f_k \left(t - \tau_{pos_k}\right)\right) Rect\left(\frac{t - \tau_{pos_k}}{\tau_{c_k}}\right), \tag{2.8}$$

and frequency domain response as

$$\begin{aligned} H(f) = &\sum_{k=1}^{N} j \frac{Sinc\left(\tau_{c_k}\left(f + f_k\right)\right)}{2\tau_{c_k}} e^{-j2\pi f \tau_{pos_k}} + \\ &+ \sum_{k=1}^{N} j \frac{Sinc\left(\tau_{c_k}\left(f - f_k\right)\right)}{2\tau_{c_k}} e^{-j2\pi f \tau_{pos_k}}. \end{aligned} \tag{2.9}$$

2.4 Temperature Extraction

An adaptive matched filter technique can be used to extract temperature information from the sensor. A change of device temperature varies the SAW velocity and translates into scaling of the frequency and the time domain responses, which can be measured as a time scaling factor. At the reference temperature, the time scaling factor, α, is one 1, and it deviates linearly as temperature coefficient of delay (TCD) of the substrate and cut used. TCD is defined as

$$R(T) = R(T_0)(1 + TCD \cdot \Delta T), \tag{2.10}$$

where $R(T)$ is measured physical parameter, $R(T_0)$ is the physical parameter at reference temperature, and ΔT is deviation of temperature from the reference temperature ($\Delta T = T - T_0$). The time scaling factor can then be defined as

$$\alpha = 1 + TCD \cdot \Delta T. \tag{2.11}$$

For Y,Z $LiNbO_3$, TCD is -94 ppm/°C [34]. An ideal reflector response model is used to synthesize an ideal matched filter for the SAW OFC reflector bank. This reference signal is used in a software-defined correlator. To measure the change in the SAW

velocity, a set of matched filters is generated as functions of temperature, which is essentially the same function but scaled in time domain given as

$$h_{correlation}(t) = h_{mf}(\alpha \cdot t) * h_{reflection}(t), \tag{2.12}$$

or in frequency domain as

$$H_{correlation}(f) = \frac{1}{\alpha} H_{mf}\left(\frac{f}{\alpha}\right) \cdot H_{reflection}(f), \tag{2.13}$$

where $h_{reflection}$ and $H_{reflection}$ is the received signal in time and frequency domains respectively, and h_{mf} and H_{mf} is a matched filter (an ideal representation of the reflected signal as shown in Equation 2.8 and Equation 2.9 respectively). The time scaling factor, α, is swept over the required range such that $h_{correlation}$ is maximized, which corresponds to the temperature of the sensor [22, 36]. Shown in Figure 2.9 is a block diagram description of the temperature extraction algorithm.

Information presented in this chapter is crucial in understanding of work accomplished in this dissertation. OFC is the core enabling technology for passive wireless SAW sensors.

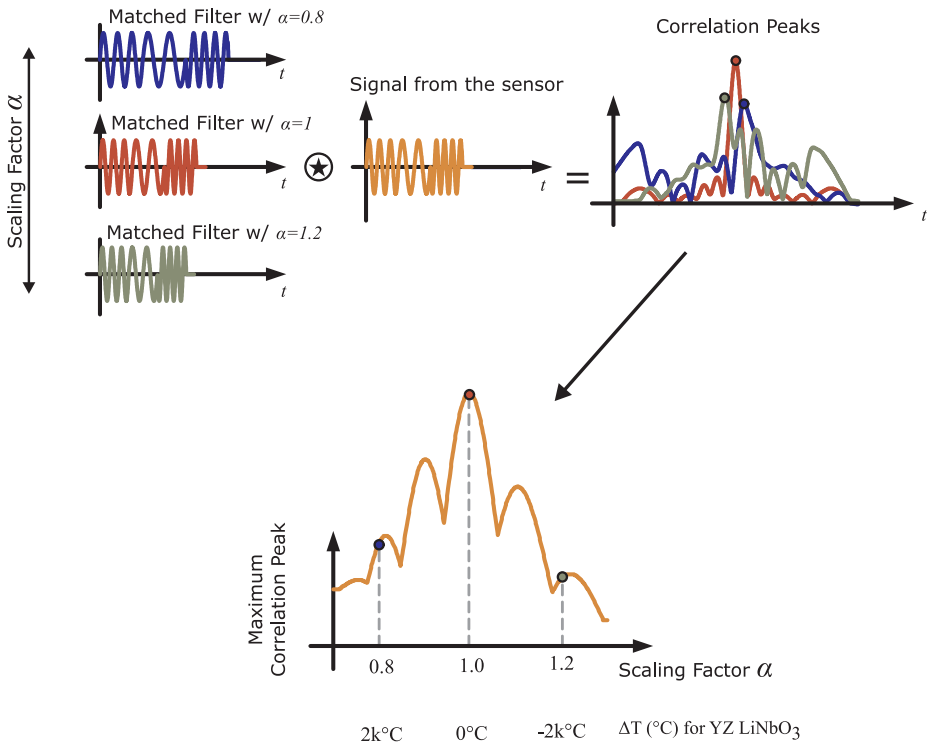

Figure 2.9: Principle of operation of the adaptive matched OFC ideal filter response to maximize the correlation waveform and extract the SAW sensor temperature. Conceptually, a series of matched filters are synthesized corresponding to differing temperatures. These signals are correlated with the received signal and the correlation signal is determined versus time. The maximum correlation peak is plotted versus scaling factor to determine the sensor temperature.

CHAPTER 3
DEVICE MODELING

Modeling is a very important step in SAW device development cycle. While there are several models available to simulate SAW devices, an accurate and common model is the coupling of modes (COM) model, which originated in the field of optics [37, 38]. In the 1980's, the COM model was applied to reflector gratings and interdigital transducer (IDT) [39, 40]. Since then, the SAW COM model has gained popularity and has been extended to include many second order effects [7, 8]. The hybrid P-matrix is used to represent various types of SAW elements. P-matrices of individual SAW elements are put together as a flow graph to form the device. The COM and electrostatic modeling and parameters are used to define the P-matrix elements. Flow graph solution, element-cascading and optimization techniques will be demonstrated in this chapter. While the complete COM equations have been developed by others, in order to establish a fundamental understanding of transducer design principles, an electrostatic-based transducer synthesis model will be discussed [41]. The result of this model is also a hybrid P-matrix that can be use with the same signal-flow

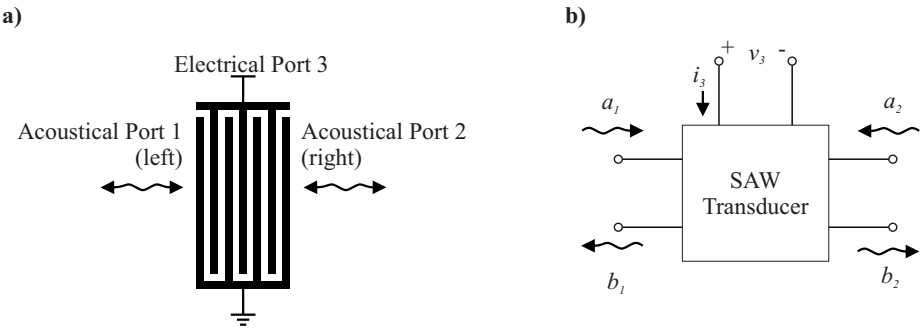

Figure 3.1: Shown in figure is (a) a schematic drawing of a SAW transducer and (b) a model view of an IDT with two acoustic and one electric ports.

device model. Also in this chapter, modeling of apodized reflectors and transducers will be discussed.

3.1 SAW Elements

3.1.1 Non-reflecting, lossless Interdigital Transducer

A schematic drawing of a SAW transducer is shown in Figure 3.1.a. A model view with incident and reflected waves at the acoustic ports and current and voltage of the electric port is shown in Figure 3.1.b.

The transducer can be represented as a P-matrix as

$$\begin{bmatrix} b_1 \\ b_2 \\ i_3 \end{bmatrix} = \begin{bmatrix} P_{11} & P_{12} & P_{13} \\ P_{21} & P_{22} & P_{23} \\ P_{31} & P_{32} & P_{33} \end{bmatrix} \cdot \begin{bmatrix} a_1 \\ a_2 \\ v_3 \end{bmatrix}, \tag{3.1}$$

where P_{11}, P_{12}, P_{21} and P_{22} is the 2×2 scattering parameter matrix of the acoustical ports, P_{13} and P_{23} are the voltage-to-SAW transfer elements, P_{31} and P_{32} are the SAW-to-voltage transfer elements and P_{33} is the admittance of the electrical port of the IDT.

The simple IDT admittance element can be calculated based on the electrical properties of the transducer layout electromechanical properties, and energy arguments of the substrate as [41]

$$G_{a0} = \pi k^2 f_0 C_0 W_a N_{eff}^2, \tag{3.2}$$

$$X(f) = \pi (f - f_0) \tau_C, \tag{3.3}$$

$$G_a(f) = G_{a0} \left[\frac{Sin(X(f))}{X(f)} \right]^2, \tag{3.4}$$

$$B_a(f) = G_{a0}\left[\frac{Sin(2X(f)) - 2X(f)}{2X(f)^2}\right]^2, \tag{3.5}$$

$$C_s = C_0 W_a N, \tag{3.6}$$

and

$$Y(f) = G_a(f) + jB_a(f) + j2\pi f C_s, \tag{3.7}$$

where f_0 is center frequency, τ_C is time response length, k^2 is the material coupling coefficient, C_0 is the substrate electrode capacitance, W_a is the acoustic aperture, N is the total number of IDT electrodes and N_{eff} is the effective number of synchronous electrode pairs. From the energy arguments for a loss-less non-reflecting transducer its P-matrix can be derived as

$$P_{33}(f) = Y(f), \tag{3.8}$$

$$P_{13}(f) = \sqrt{\frac{1}{2}G_a(f)}e^{-j\pi\tau_c f} = P_{23}(f), \tag{3.9}$$

and

$$P_{31}(f) = -2P_{13}(f) = P_{21}(f). \tag{3.10}$$

For a non-reflecting IDT reflection coefficients of the S-parameter matrix of the acoustical port are zero, or [41]

$$P_{11}(f) = P_{22}(f) = 0. \tag{3.11}$$

Assuming that the IDT coupling is low, acoustical parameters from one acoustical port to the other can be modeled as a delay as

$$P_{21}(f) = e^{-j2\pi\tau_c f} = P_{12}(f). \tag{3.12}$$

.

3.1.2 Other Structures

The other two elements that will be used in the synthesis model are a delay path and an ideal edge reflector. The hybrid P-matrix for a simple delay is expressed as

$$\begin{bmatrix} b_1 \\ b_2 \\ 0 \end{bmatrix} = \begin{bmatrix} 0 & e^{-j2\pi f\frac{L}{v}} & 0 \\ e^{-j2\pi f\frac{L}{v}} & 0 & 0 \\ 0 & 0 & 0 \end{bmatrix} \cdot \begin{bmatrix} a_1 \\ a_2 \\ 0 \end{bmatrix}, \tag{3.13}$$

where v is the delay path surface velocity. The P-matrix of an ideal edge reflector is expressed as

$$\begin{bmatrix} b_1 \\ b_2 \\ 0 \end{bmatrix} = \begin{bmatrix} -1 & 0 & 0 \\ 0 & -1 & 0 \\ 0 & 0 & 0 \end{bmatrix} \cdot \begin{bmatrix} a_1 \\ a_2 \\ 0 \end{bmatrix}. \tag{3.14}$$

3.2 Signal Flow Representation

A signal-flow graph approach will be used to simulate an entire device. First each device is represented as a three- or two-port signal-flow graph as demonstrated in Figure 3.2. Then incident nodes are connected to the reflected nodes of the acoustic ports of adjacent elements as shown in Figure 3.2 highlighted in red. If two or more transducers are assigned to the same electrical port, they are connected as shown in Figure 3.3 for electrically in parallel (green) and serially (purple) connected ports, respectively. For transducers connected electrically in parallel, incident node

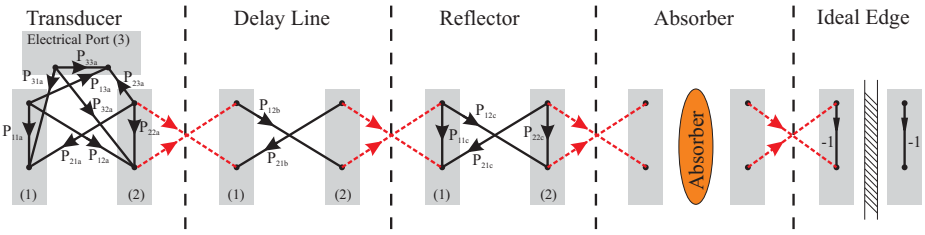

Figure 3.2: Signal-flow graph representation of SAW elements: transducer, delay, reflector, absorber, and an ideal edge. Shown in red are element connection going from reflected port of one element to the incident port of an adjacent SAW element.

of electrical port of first transducer is connected to the incident node of electrical port of second transducer and reflected node of electrical port of second transducer is connected to the reflected node of electrical port of first transducer, in which case, the newly formed common electrical port has the same nodes as the first transducer. For transducers connected electrically in series reflected node of electrical port of first transducer is connected to the incident node of electrical port of second transducer, in which case, the newly formed electrical port will have incident node of first transducer and reflected node of the second transducer. It is important to distinguish between device port and transducer electrical port. For example, a device might have two device ports and three transducers (each transducer has one electrical port). The electrical ports of first and second transducers can be connected to the first device port and electrical port of third transducer is connected to the second device port.

Once the signal-flow graph for the entire single-track device is completed, the device solution can be represented as a simple hybrid P-matrix as given in Equation 3.15

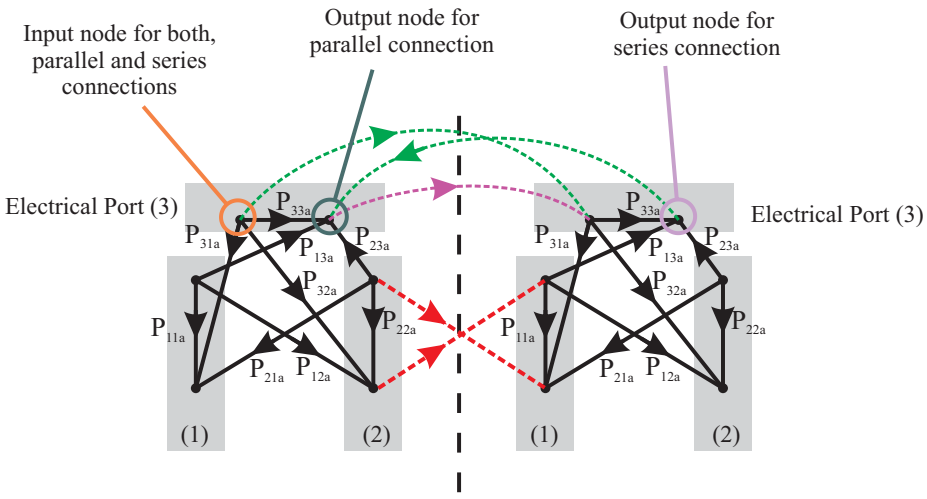

Figure 3.3: Signal-flow graph representation of two transducers that are assigned to the same electrical port connected in parallel (green) and in series (purple).

$$\begin{bmatrix} b_1 \\ b_2 \\ i_3 \\ \vdots \\ i_{n+2} \end{bmatrix} = \begin{bmatrix} \overbrace{\begin{matrix} P_{11} & P_{12} \\ P_{21} & P_{22} \end{matrix}}^{\text{Acoustical-only S-Parameter}} & \begin{matrix} P_{13} & \cdots & P_{1,n+2} \\ P_{23} & \cdots & P_{2,n+2} \end{matrix} \\ \begin{matrix} P_{31} & P_{32} \\ \vdots & \vdots \\ P_{n+2,1} & P_{n+2,2} \end{matrix} & \overbrace{\begin{matrix} P_{33} & \cdots & P_{3,n+2} \\ \vdots & \ddots & \vdots \\ P_{n+2,3} & \cdots & P_{n+2,n+2} \end{matrix}}^{\text{Electrical-only Y-Parameter}} \end{bmatrix} \begin{bmatrix} a_1 \\ a_2 \\ v_3 \\ \vdots \\ v_{n+2} \end{bmatrix}. \tag{3.15}$$

where n is number of unique ports in the device. Generally, only the admittance sub-matrix (Y-parameter) is of interest. Values of all elements of the Y-parameters can be computed using Mason's gain formula as [9]

$$G = P_{n,m} = \frac{i_n}{v_m} = \frac{\sum_{k=1}^{N} G_k \Delta_k}{\Delta}, \tag{3.16}$$

where $G = P_{n,m}$ is an element of the admittance sub-matrix of the hybrid P-parameter, N is number of forward paths, G_k is the gain of a k^{th} forward path, Δ_k is one less sum of all loop gains non-touching forward path G_k, and Δ is one less

sum of all loop gains plus sum of products of all non-touching loop gains taken two at a time.

3.2.1 Optimization

For a long multi-element devices, the process of calculating all forward path and loop gains can become very time consuming. One way to reduce the computational times is to combine adjacent SAW elements two at a time, until only a small structure remains. The following combinations of elements are most straight forward to cascade: two elements with acoustical ports only, one element with acoustical port and one element with an electrical port, two elements with electrical ports assigned to the same port of the complete device. Combining elements that are connected to different device ports creates an additional level of complexity and is not cost effective computationally. The two elements are removed from the device model and are treated as a stand-alone element. Their P-matrix is computed and is inserted into the original device in place of the two removed elements. An example of this optimization method in action is given in Figure 3.4. In step 1, two acoustic-only devices are combined together to produce a computed acoustic-only element. In step 2, the computed element is cascaded with a transducer to produce a computed element

with an electrical port, which is assigned to the same device port. In step 3, since the new computed is assigned to the same device port as the following transducer, they too can be cascaded together. The next element in the device has an electrical port which is not assigned to the same device port; therefore, these two elements cannot be cascaded, so, in step 4, the next pair of the elements that can be cascaded is found until there are none left.

3.3 Multi-Track Devices

It is possible, to have device with multiple acoustical tracks and interconnected transducers between the tracks as shown in Figure 3.5. The number of ports and their assigned names must be the same across all tracks. Separated tracks are computed as separate devices. If ports across multiple tracks are connected in parallel, as shown in Figure 3.5.a, the Y-parameters of separate tracks are simply added together. If ports are connected in series, as shown in Figure 3.5.b, Y-parameters must first be converted to Z-parameters that can be added together. For mixed connections, as shown in Figure 3.5.c, a custom equation needs to be determined.

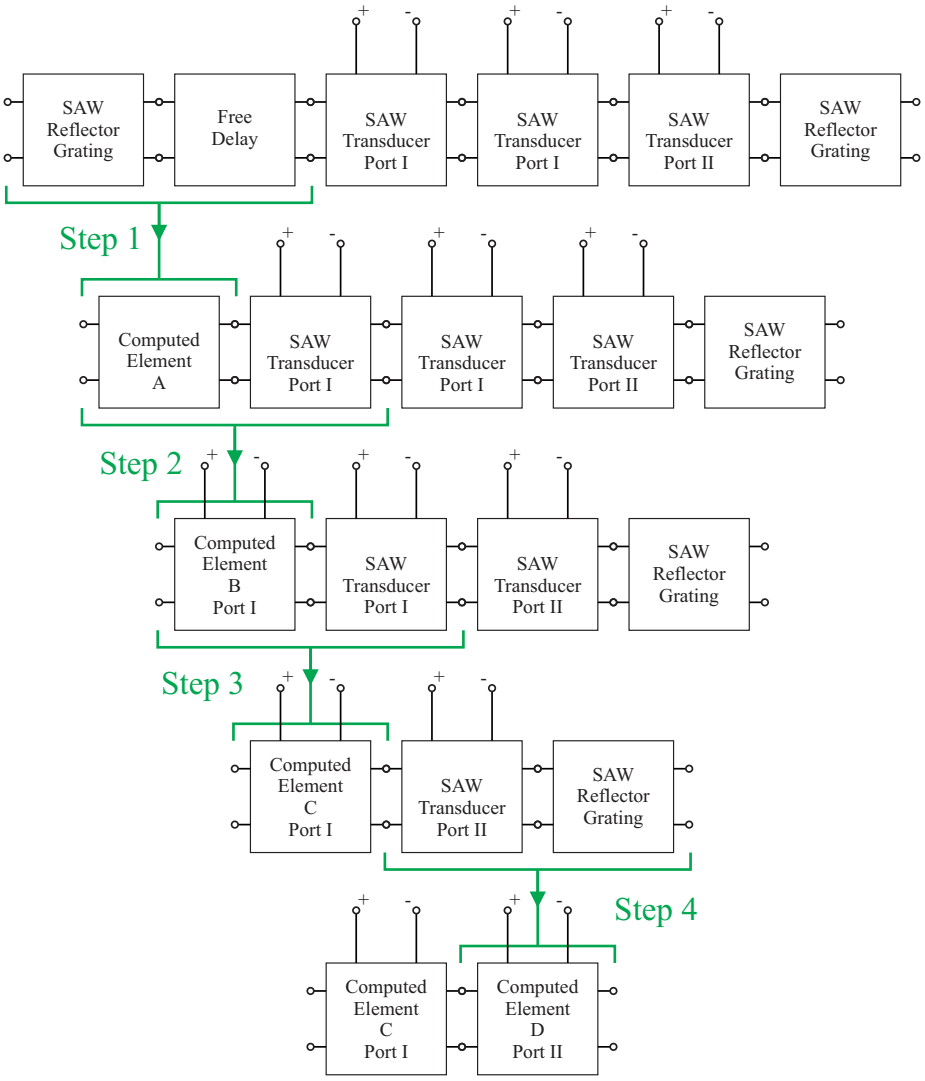

Figure 3.4: Example of cascading adjacent SAW elements to reduce the size of the final device.

3.4 Modeling of Apodized Reflectors

Apodization is a useful tool when precise control over the envelop function in time or profile in frequency is needed. Apodized devices can be tuned to have flatter pass- or reflect-bands, lower side-lobes, or a different bandwidth for the same response time length.

In order to simulate an apodized reflector using the COM model, each track is divided into sub-tracks in such way that each sub-track has only uniform portion of the reflector as shown in Figure 3.6. Free space delay is added before and/or after the uniform portion of the reflector (as shown in Figure 3.7.a) and the sub-track is then

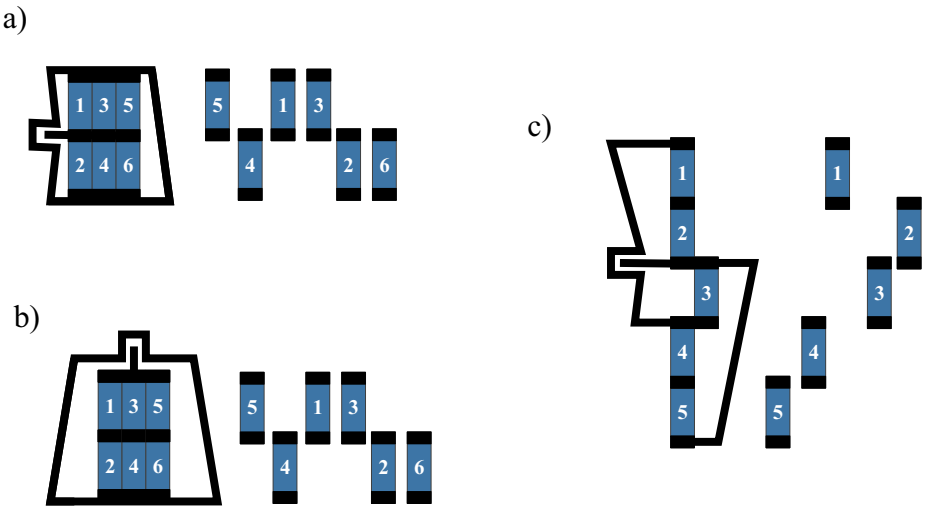

Figure 3.5: Examples of multi-track devices: electrical ports of the two track connected in a) parallel, b) series, and c) electrical ports of multiple tracks with mixed connection types.

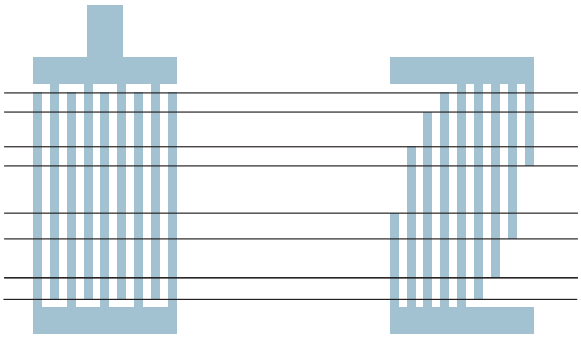

Figure 3.6: COM model apodized reflector representation as series of tracks.

simulated as a separate device. Once each sub-track is calculated the Y-parameters can be added together for the final result.

Since the free surface velocity differs from the surface velocity under the grating, there will be a phase difference from one sub-track to the other. In order to reduce this difference, half of the delay is metalized but this only occurs when total delay is longer than a single electrode-gap pair as shown in Figure 3.7.b.

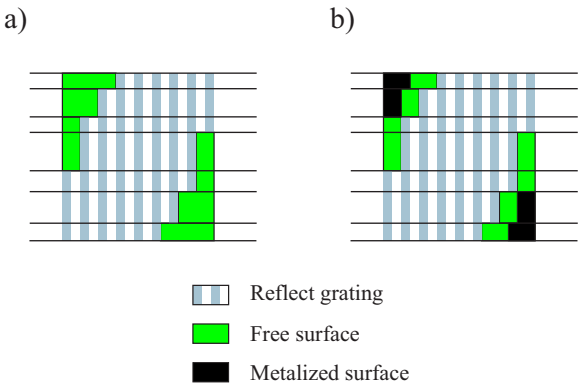

Figure 3.7: Example of sub-track representation (a) with free surface delays and (b) half free and half metalized surface delays.

Figure 3.8 compares a simulation of a uniform reflector (dotted blue curve) to a simulation of apodized reflector modeled with free surface delays (dashed green curve) and with apodized reflector modeled with half free half metalized surface delays (solid red curve). Both apodized reflectors had Hamming window envelope applied to them. It can be noted that the apodized reflector without metalized delays has a very non-symmetric response and a highest side-lobe only 5 dB lower than the uniform reflector. In contrast, the apodized reflector modeled with compensated metalized delays has a very symmetric response with highest side-lobe nearly 25 dB lower than the one of the uniform reflector.

3.5 Examples

Illustrated in Figure 3.9(a) is a sample device consisting of a transducer with 9 MHz bandwidth, a delay, and a reflector with 13.5 MHz bandwidth. The center frequency for both reflector and transducer is approximately 247 MHz. The COM model was used to compute the Y-parameters which was then converted to an S-parameters [42]. Shown in Figure 3.9(b) is a reflection coefficient simulated using COM model simulation of just the transducer (solid green curve) and the compete device (dotted

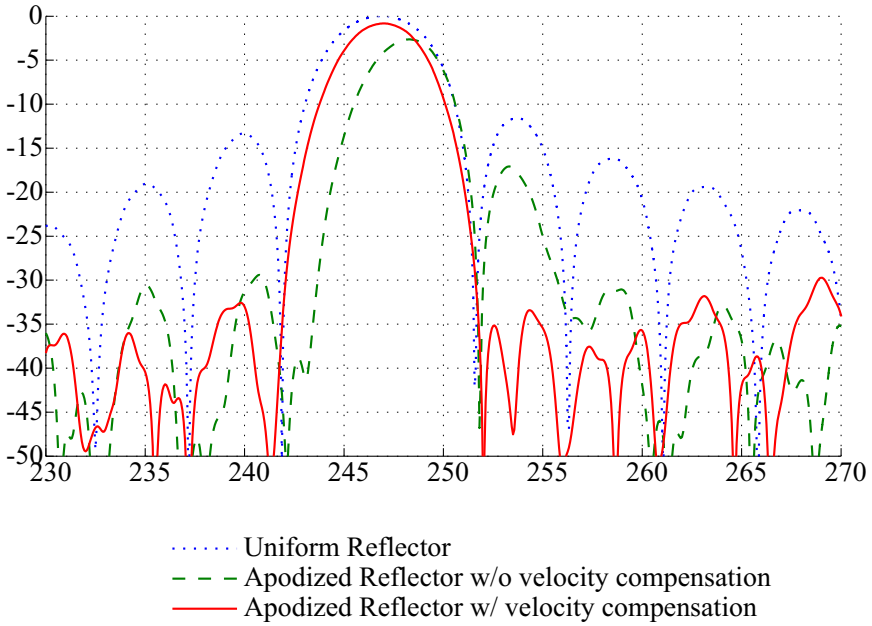

Figure 3.8: Comparison of a uniform reflector (blue dotted curve) with apodized reflector modeled with free surface delays (dashed green curve) and with apodized reflector modeled with half free half metalized surface delays (solid red curve).

blue curve). In the frequency domain, the reflector response shows up as a ripple on top of the transducer response.

A dual track device is shown in Figure 3.10. The transducers and reflectors bandwidths are similar to the device in Figure 3.9; however, the center frequencies of the two tracks chosen in such way that the transducers are orthogonal to each other. The transducers are electrically in parallel and acoustically isolated. Shown in Figure 3.11(a) and Figure 3.11(b) is the impulse response of the multi-track device in the frequency and time domains respectively. In the frequency domain, the two responses are neat to each other. Since the tracks are acoustically separate from each other, there is no inter-chip reflections, as can be seen in time domain plot. The main reflection of the first reflector is at 1.5 μs and its triple-transit response at 3

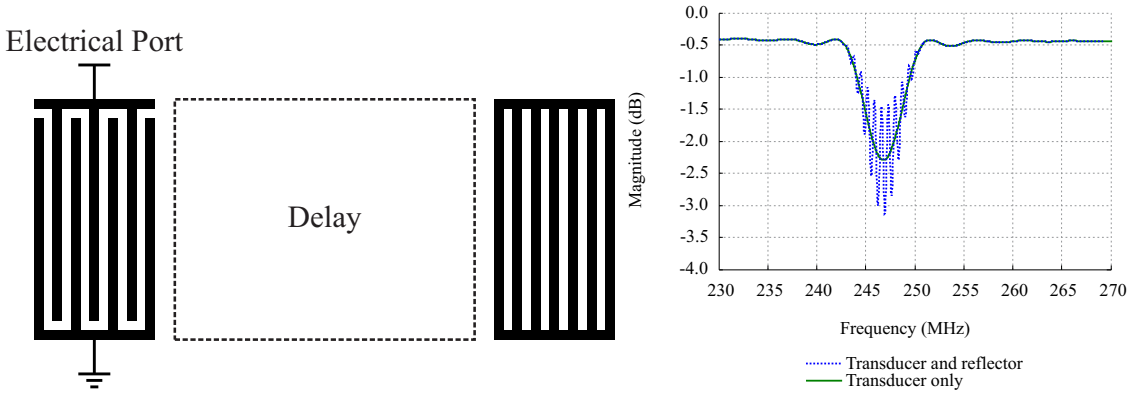

(a) Layout (b) Reflection at the electrical port

Figure 3.9: Simple, single track tag/sensor device example.

μs. Response of the second reflector comes in at 2 μs with the triple transit trailing at 4 μs.

To demonstrate the versatility of the signal-flow graph approach, the device of Figure 3.10 is reconfigured and now the two transducer-reflector pairs are in the same acoustical path as shown in Figure 3.12(a). The time domain impulse response of the device is shown in blue in Figure 3.13. One can note, since all transducers and reflectors are within the same acoustical path, there are now multiple inter reflections present. Adding an absorber, as shown in Figure 3.12(b), acoustically separates the transducer-reflector pairs and, since the transducers are still connected electrically in parallel, yields the same result as in dual track case as can be seen from the dotted green curve of Figure 3.13.

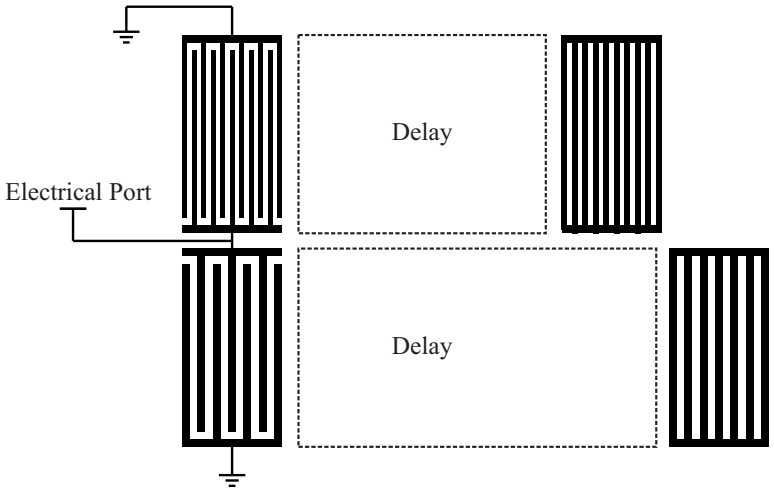

Figure 3.10: Simple, dual track, orthogonal tag/sensor device example.

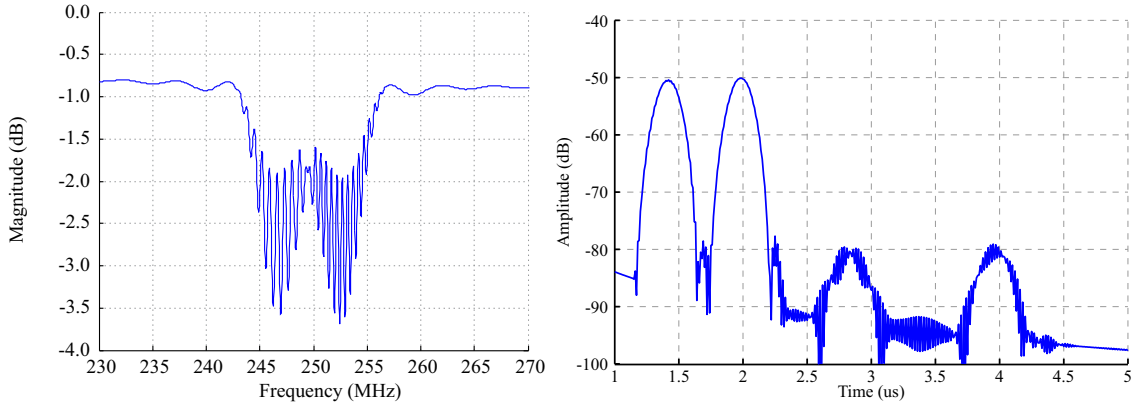

(a) Frequency domain (b) Time domain

Figure 3.11: Impulse response of the simple, dual track, orthogonal tag/sensor device given in Figure 3.10.

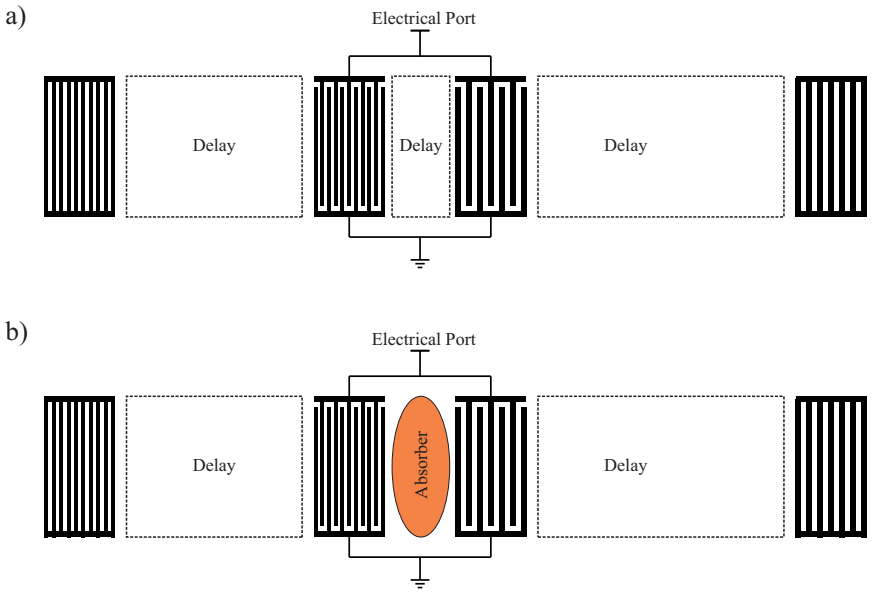

Figure 3.12: Device example.

3.6 Summary

This chapter has presented signal-flow graph representation of SAW devices using elements that are expressed as hybrid P-matrices. P-matricies can be calculated from previously developed COM equations (when used signal-flow graph solution, this model will be referred to as COM model). An electrostatic expression for the P-matrix for the transducer has been presented, when used with the signal-flow graph solution this model is referred to as the synthesis model. Also, modeling of apodized reflectors has been demonstrated for the purposes of bandwidth shaping and side-lobe reduction.

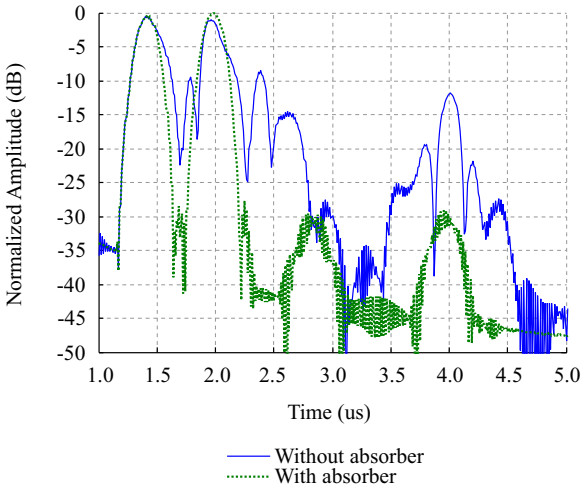

Figure 3.13: Device example.

CHAPTER 4
SAW NOISE-LIKE REFLECTORS AND DEVICE CODING

There are several properties that a good passive wireless reflective tag or sensor should have; good auto-correlation (narrow peak, low side-lobes), minimized code collision (low cross-correlation) with other codes, and low loss [36]. Current schemes for finding good codes for multi tag or sensor environments are complex and system dependent due to the asynchronous nature of the SAW system, which often limits system performance.

Nature has provided numerous examples of the use of periodic, pseudo-periodic and aperiodic structures to attain certain desired properties. One example is the definition of an electronic material as single-crystal (periodic), poly-crystalline (pseudo-periodic) or amorphous (aperiodic). In a material, such as a semiconductor, the structure has a profound effect on the material properties and movement of an electron through the material. The effect of a material structure on the electron propagation is analogous to that of the light propagating in certain optical structures,

which has been termed photonic materials or structures. The same analogy is true for an acoustic mode propagating in certain structures, termed phononic structure.

A large body of work has analyzed or showed initial results of wave propagation in phononic crystals. Some work has focused on creation of acoustic band gaps in phononic crystals [43, 44, 45, 46], guiding of waves using phononic crystals has been experimentally demonstrated [47, 48], and SAW effects in phononic structures have been studied [49, 50, 51]. Nelin described phase apodization in crystals to generate a phononic structure response, which may also have application in future phononic SAW structures [49]. Dhar and Rogers used lithography to fabricate phononic structures on crystals [52].

This chapter will introduce a study of some SAW phononic structures and their SAW propagation properties. The structures will consist of periodic, pseudo-periodic and aperiodic reflectors that have interesting frequency and time domain characteristics. It is possible to produce some new and unique one dimensional phononic structures using similar concepts developed for orthogonal frequency coded (OFC) SAW devices [28]. The chapter will provide definitions of the structures, a basic theory and predictions based on a coupling of modes (COM) formulation. Experimental results of devices fabricated on Y,Z $LiNbO_3$ will be compared to theoretical predictions.

The motivation for this research is to develop a system for wireless, passive interrogation of SAW multi-sensors. A SAW device platform, which has RFID encoding for identification of 4-100 devices, has low loss and good range, can accommodate differing on-board sensor functions, and can operate in a wide range of space and ground-based applications. The device approach chosen uses SAW orthogonal frequency coded (OFC) reflectors and transducers in a delay line embodiment to provide an RFID tag [28]. This presentation will focus on new SAW OFC device efforts for the device platform that provides the communication link for the sensor system [4, 26, 20, 31, 25].

4.1 Definitions and Theory

4.1.1 AWGN and Noise-like Reflector (NLR) Structures

As a conceptual model for NLR structures, additive white Gaussian noise (AWGN) was examined. Since the power spectrum of AWGN is constant, its autocorrelation produces a peak at time t=0, and zero everywhere else. The lack of correlation side-lobes is highly desirable since the time domain autocorrelation energy is tightly confined around a point, which is a goal of coding schemes [53].

The device embodiment studied assumes a single SAW transducer connected to an antenna, and a SAW reflector delayed from the transducer. The transducer input admittance is the sum of the electrical input admittance, with no reflector, plus a term which is a function of the transducer coupling and the delayed reflector response. This can be converted to scattering parameters of the transducer electrical port, $S_{11}(f)$. The frequency dependent reflected wave can be written as following product

$$A_1(f) = \alpha \cdot P_{31}(f) \cdot \Gamma(f) \cdot P_{13}(f), \tag{4.1}$$

where $P_{31}(f)$, $P_{13}(f)$ are P-matrix parameters of electrical-to-acoustical port conversion and vice versa, $\Gamma(f)$ is the reflected wave from the SAW grating, and a delay between the reflection grating and the transducer can be included in α. Since the delay between the reflector grating and the transducer only offsets the correlation, assuming no loss, α is set to unity without loss of generality.

When calculating the cross-correlation, the matched filter function consists only of the grating reflection response. Therefore, the cross-correlation takes the form of

$$H_{cc}(f) = A_1 \cdot \Gamma^*(f). \tag{4.2}$$

Substituting equation (4.1) into the equation (4.2) results in a simplified form of $H_{cc}(f)$ as

$$H_{cc}\,(f) = P_{31}(f) \cdot \Gamma(f) \cdot P_{13}(f) \cdot \Gamma^{*}(f). \tag{4.3}$$

Assuming, for the moment, a constant magnitude of 1 for $\Gamma(f)$, equation (4.3) is simplified further as

$$\begin{aligned} H_{cc}(f) &= P_{31}(f) \cdot \Gamma(f) \cdot \Gamma^{*}(f) \cdot P_{13}(f) \\ &= P_{31}(f) \cdot P_{13}(f). \end{aligned} \tag{4.4}$$

The relationship between P_{13} and P_{31} is [41]

$$P_{13}(f) = -2P_{31}(f). \tag{4.5}$$

Applying equation (4.5) to equation (4.4) results in the final simplified expression for the transducer's cross-correlation as

$$H_{cc}(f) = -2P_{31}^2(f) \tag{4.6}$$

From this point on, the expression in equation (4.6) will be referenced as the transducer effect. Given that the reflection of the grating was assumed to have a constant magnitude and random phase (AWGN), the transducer effect can dominate the shape of the correlation peak.

To determine the effects of transducer band-limiting, an AWGN simulation was conducted and sampled at $f_s = 2$ GHz. Noise was then band-limited at center frequency, $f_0 = 250$ MHz. Two types of transducers were simulated assuming simple, ideal time responses: an unapodized IDT (Rect time function and Sinc frequency response) and cosine apodized IDT. Two transducer effects are of interest: 1) the narrower the bandwidth, the larger the correlation peak width ($BW = \gamma/\tau$, where γ is a constant depending on time window), and 2) the transducer time response changes the time domain correlation shape. Both of these effects are as expected from Fourier transform theory and need to be considered in final designs. Unfortunately, the idealized AWGN auto-correlation properties can never by obtained because of the band-limiting effects of the SAW transducer, as well as practical device and system limitations associated with RF components bandwidth, antenna bandwidth,

and necessary matching networks bandwidth. However, understanding the limitation will aid in optimizing a design.

4.1.2 Primitive Cell Structure Definition

All devices are composed of multiple, individually defined, primitive structures that are composed of an electrode and gaps that define a period, p, as shown in Figure 4.1.

The relationships that map from physical dimensions into the time domain for the primitive cell are given in the following parameters as

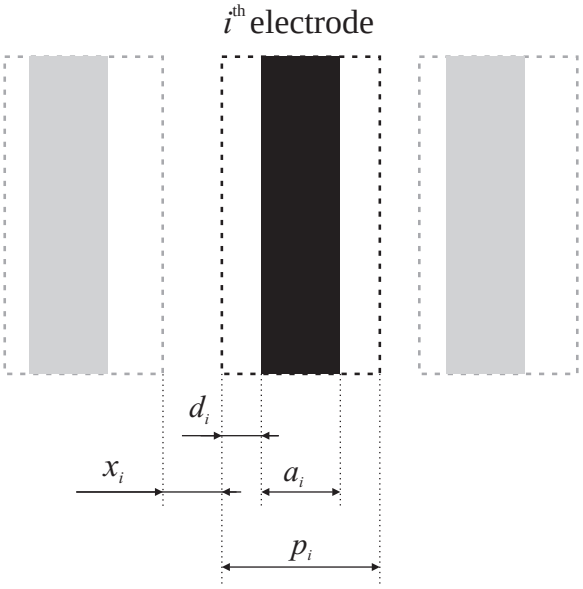

Figure 4.1: Definition of ith Electrode (Primitive Structure)

$$f_i = \frac{v}{p_i}. \tag{4.7}$$

A delay offset between primitive cells is given as

$$\tau_{c_i} = 2\frac{p_i}{v}. \tag{4.8}$$

where f_i is the center frequency of the primitive structure, τ_{c_i} is the impulse response length of the primitive cell, and v is the SAW velocity.

$$\tau_{p_i} = 2\frac{x_i}{v}. \tag{4.9}$$

where τ_{p_i} is the impulse response offset of the i^{th} primitive structure.

For a reflector, τ_{c_i} and τ_{p_i} are double of the physical dimension calculated delay, since this is a round trip reflection:

$$d_i = 0 \quad \text{(reference chosen)}, \tag{4.10}$$

and

$$a_i = \frac{p_i}{2}. \tag{4.11}$$

Equations (4.7) through (4.11) relate physical dimensions to time and then into SAW device layout parameters.

4.2 Noise-Like Reflector Structures

4.2.1 Devices

4.2.1.1 OFC Reflector Structures

The starting structure was an OFC reflector array consisting of 7 chips and the total number of electrodes is 182 [28]. Detailed parameters are described in Table 4.1. This device will be denoted by OFC7 in all future discussions.

4.2.1.2 Random Reflector Structures

The first random structure examined is based on the OFC7 reflector array where the primitive cells (electrode-gap pairs) were randomly shuffled as shown in Figure 4.2.

This structure has the same number of electrodes (182) that are placed one after another; therefore, time response length of the new device is the same as time length of the OFC device it was based of. In future discussions this device will be denoted as RND7.

4.2.1.3 Reflector Structures with PPM

Another way to produce a random device is to insert at random additional gaps of various lengths between the primitive cells. This technique can be recognized as pulse positioning modulation (PPM) [54].

Table 4.1: OFC Device Design Values

	Frequency (MHz)	**Number of electrodes**	**Position**
f_1	221.14	23	1
f_2	230.76	24	6
f_3	240.38	25	3
f_4 (f_0)	250.00	26	2
f_5	259.62	27	5
f_6	269.24	28	4
f_7	278.86	29	7

A random device design with PPM included the following parameters; at random one half of the primitive cells were assigned 0 and another half were assigned 1. Cells corresponding to 0 remained at $x_i = 0$, and cells corresponding to PPM code 1 had a value of $x_i = p_i/2$ as

$$x_i = \begin{cases} 0 & \text{if PPM code is 0} \\ p_i/2 & \text{if PPM code is 1} \end{cases} . \tag{4.12}$$

Such delay creates a π offset of the local frequency of the primitive cell with respect to its original position.

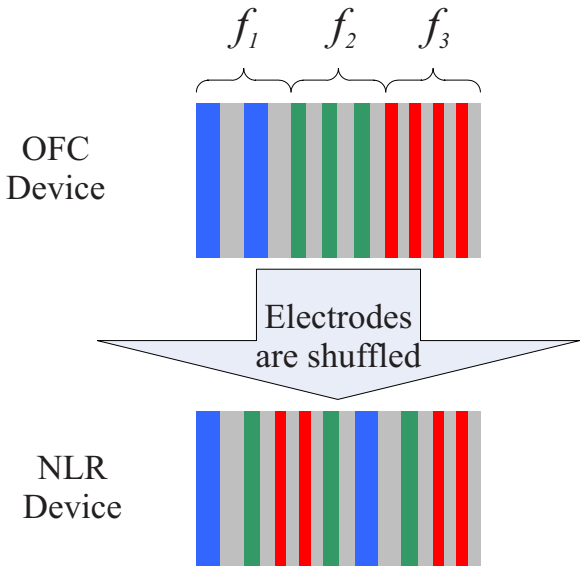

Figure 4.2: Schematic drawing of an OFC device (top) and an NLR device (bottom) which is based on the OCF device.

This modulation was applied to both OFC7 and RND7 reflector structures as demonstrated by Figure 4.3. Both structures have the same number of electrodes; however, the time response length was increased by approximately 25%, since the impulse response length of half of cells was increased by 50%. These devices will be referenced as OFC7-PPM and RND7-PPM in future discussions presented. The motivation for examining both of these structures is to determine whether there is an advantage in keeping the same size cells (as in case of OFC7-PPM grouped together) versus a completely random structure (RND7-PPM).

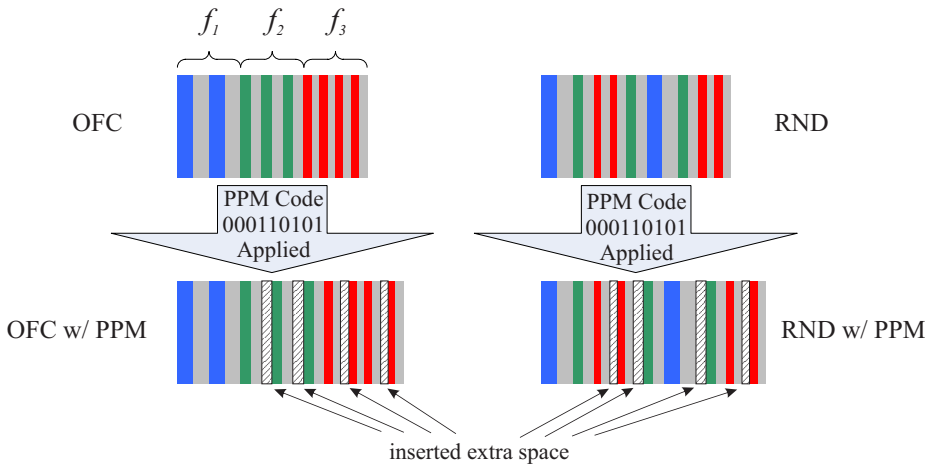

Figure 4.3: Pulse position modulation applied to an OFC (left) and NLR (right) devices.

4.2.2 NLR Structures Modeled using Ideal Reflector Model

Figure 4.4 is the simulated ideal reflector model frequency domain response of RND7, OFC7 and OFC7-PPM reflector structures. It can be seen that the RND7 device has the most narrow frequency response. Each electrode within the random array has frequency of $f_0 \pm \Delta f$, and since electrodes are randomly placed, the device looks like a poorly fabricated single frequency reflector grating with center frequency f_0. Therefore, its frequency response is expected to be narrow. The OFC reflector structure has the expected frequency response [28]. Reflector array OFC7-PPM, has the widest band response due to PPM. The reflected signal looks like a CDMA signal filling in envelope that resembles single electrode response with center frequency f_0 and ultra-wide bandwidth. A narrow band plot (band of interest) is shown in Figure 4.5, and highlights the spectral response.

Figure 4.6 shows auto-correlations of OFC7, RND7 and OFC7-PPM responses in the time domain. As expected, the wider the frequency domain response, the narrower the correlation peak. RND7 device produced widest (worst) correlation peak and OFC7-PPM produced the most narrow (best) one.

PPM coding was applied to both RND7 and OFC7 reflectors and Figure 4.7 compares the frequency domain responses. Both plots are similar and at this point

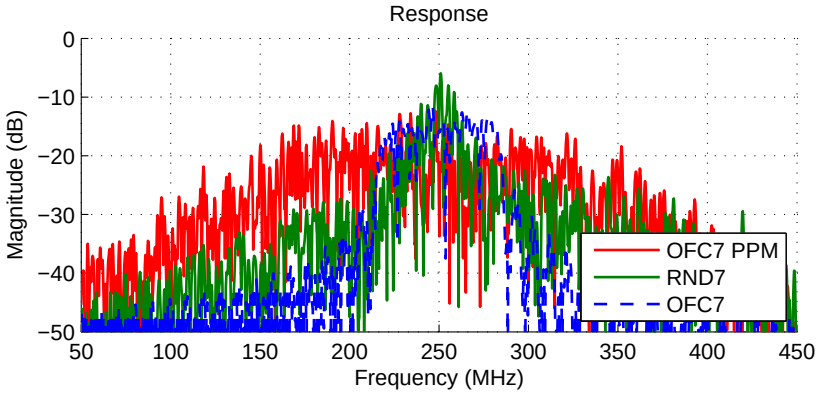

Figure 4.4: Comparison of spectrum spreading of OFC7, RND7 and OFC7-PPM reflector structures using the ideal reflector model.

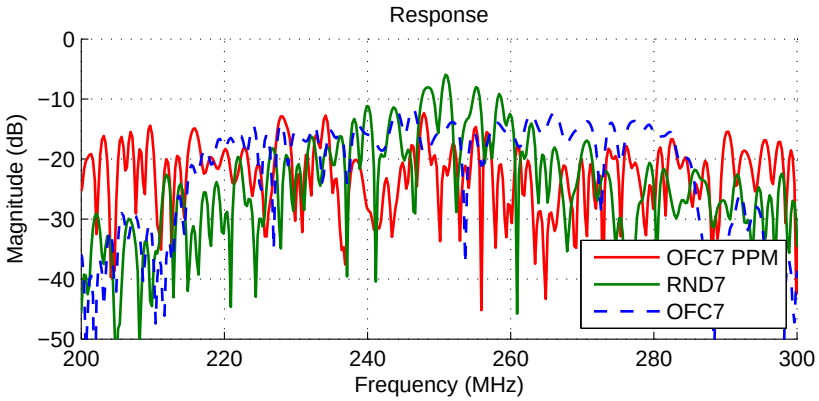

Figure 4.5: Comparison of signal distribution of OFC7 (blue), RND7 (green) and OFC7-PPM (red) reflector structures simulated from the ideal reflector model.

it is not clear whether having identical cells grouped together has any advantages over a completely random reflector structure. Figure 4.8 compares auto-correlations of RND7-PPM and OFC7-PPM. Again, there are no apparent advantages of one structure over another.

Reflector structures encoded with PPM lead to extremely wide band responses. Since transducers used with such reflectors are going to have narrower bandwidth, band-limiting effects on the correlation are examined. As part of this research, several different shapes and bandwidth transducers effects were examined. As a general rule, as bandwidth decreases the correlation peak becomes wider and smaller. However, the shape of the frequency domain response of the transducer effect is also important. Figure 4.9 demonstrates the effect for brick-wall shaped frequency domain response with 120 MHz bandwidth. One notices that OFC7 and RND7 do not show significant

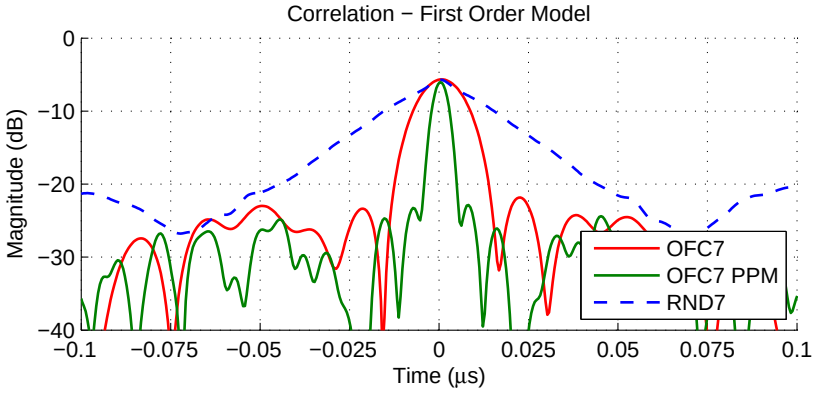

Figure 4.6: Comparison of ideal correlation peaks for OFC7, RND7, and OFC7-PPM devices, ideal reflector model.

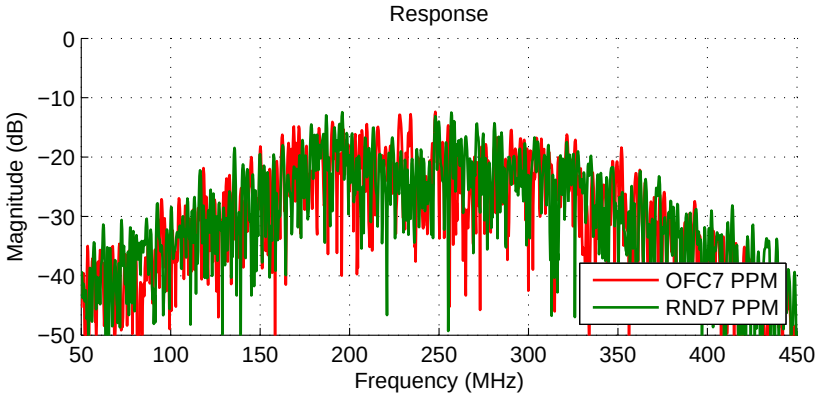

Figure 4.7: Comparison of frequency responses of OFC7-PPM and RND7-PPM, ideal reflector model.

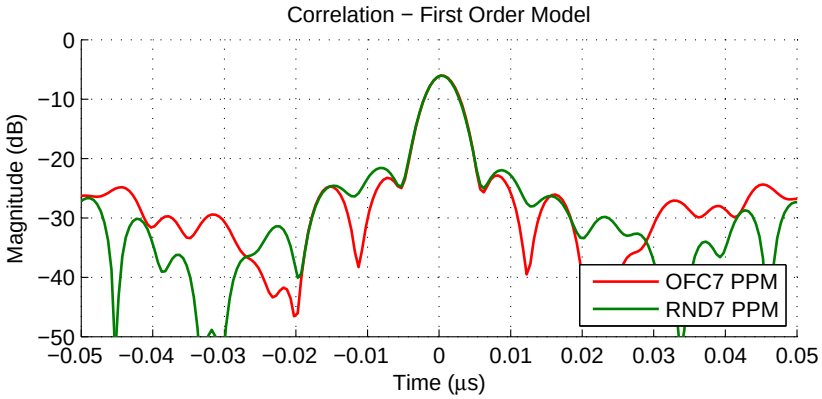

Figure 4.8: Comparison of ideal correlation peaks of OFC7-PPM and RND7-PPM, ideal reflector model.

changes after the transducer effect is applied; however, the OFC7-PPM correlation peak became wider and dropped by 3 dB. The transducer effects the overall frequency response, reducing the transducer-reflector effective bandwidth, which leads to a reduced correlation peak and wider compressed pulse width.

4.2.3 NLR Structures Modeled using COM Model

While the ideal reflector model is a good synthesis tool, for initial predictions, the COM model was used to simulate SAW reflector responses, including second order effects. For purposes of comparison of ideal reflector model results to COM model results, Figure 4.10 through 4.12 compare predictions of the ideal reflector model

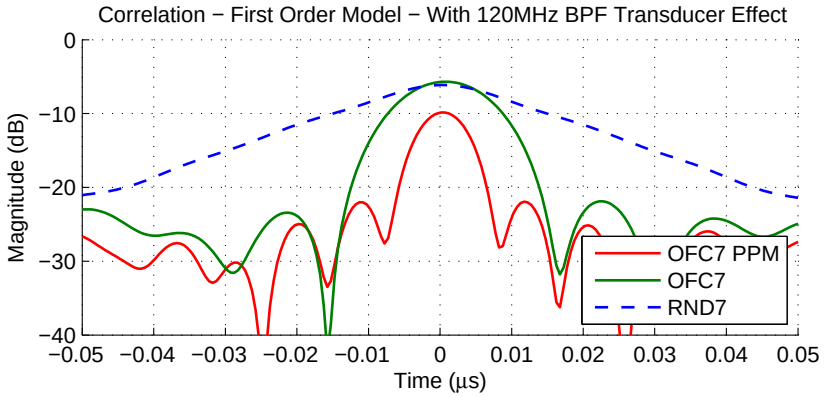

Figure 4.9: Comparison of band limiting effect of 120MHz brick wall band-pass filter (BPF) IDT on ideal correlations of OFC7, RND7 and OFC7-PPM devices, ideal reflector model.

to the COM model. Reflection predicted by the COM model was compared to the response simulated by the ideal reflector model. Figure 4.13 through 4.15 compare COM model correlations to the ideal ones. Both frequency domain responses and correlations of the two models agree well, which verifies that the ideal reflector model is a good synthesis tool.

4.2.4 Device Layout and Data Extraction

In order to be able to extract clean reflection data, test devices were built having two transducers on one side of a reflector as shown in Figure 4.16. S_{21} was measured from these two-port structures over the band of interest.

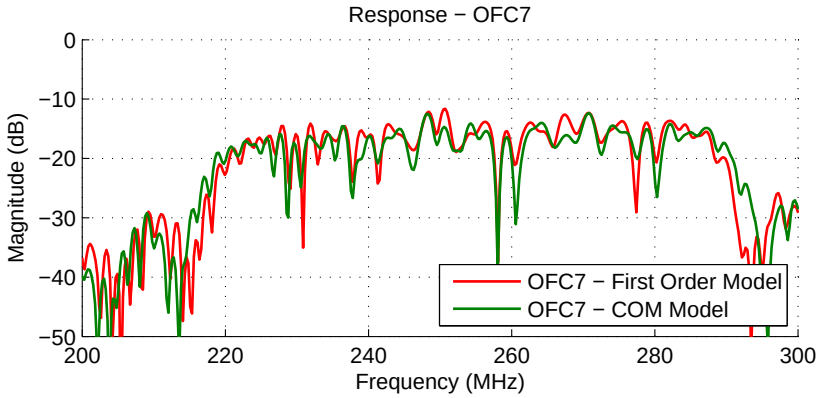

Figure 4.10: Comparison of OFC7 device frequency response predicted by ideal reflector model and COM model.

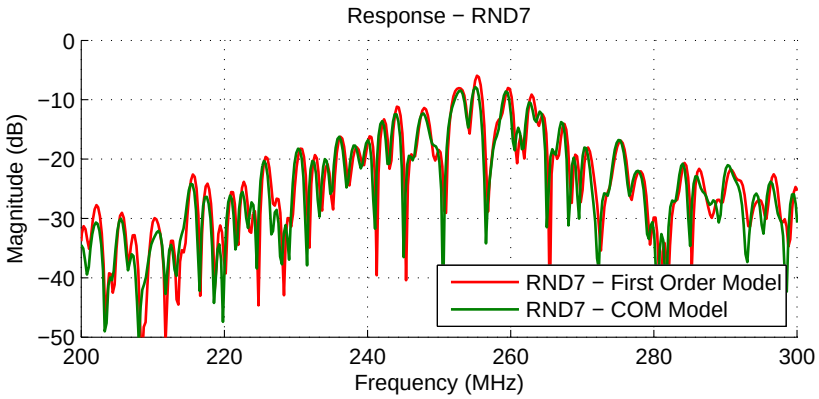

Figure 4.11: Comparison of RND7 device frequency response predicted by ideal reflector model and COM model.

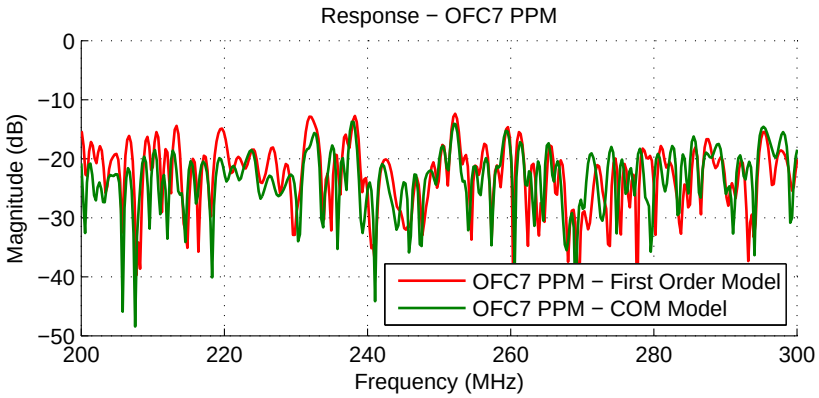

Figure 4.12: Comparison of OFC7-PPM device frequency response predicted by ideal reflector model and COM model.

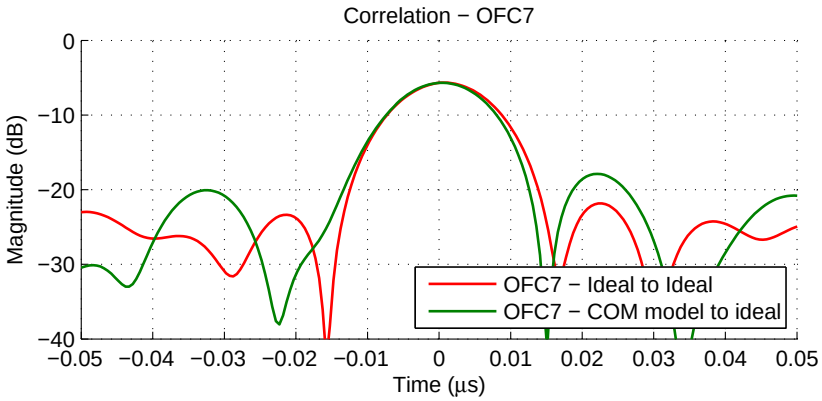

Figure 4.13: Correlation peak of ideal to ideal signal (red) compared to correlation peak of COM model to ideal signal (green) of OFC7 device.

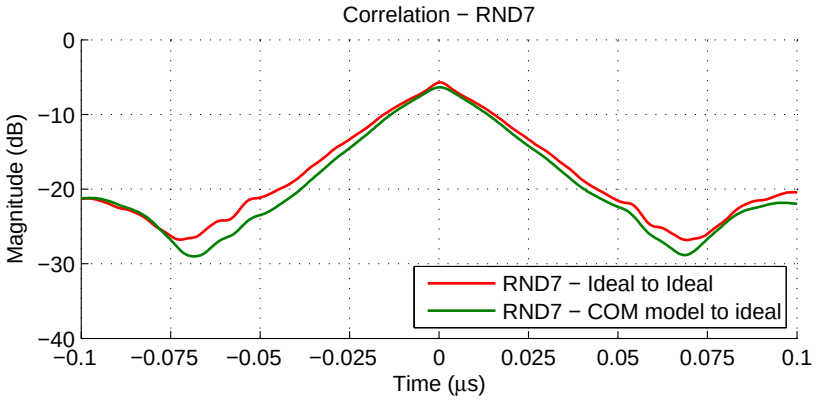

Figure 4.14: Correlation peak of ideal to ideal signal (red) compared to correlation peak of COM model to ideal signal (green) of RND7 device.

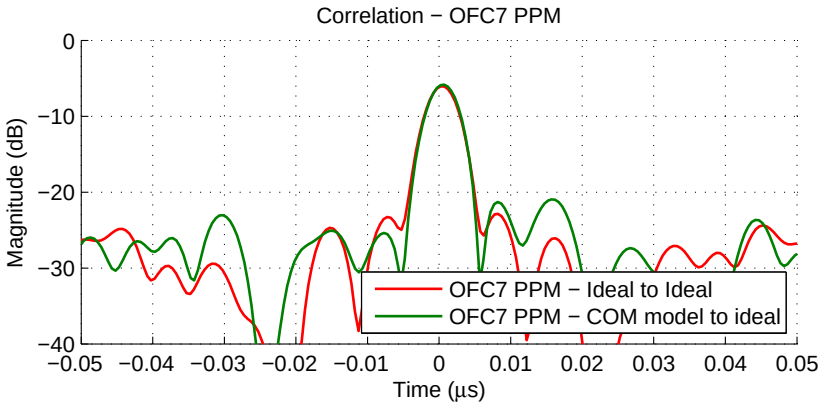

Figure 4.15: Correlation peak of ideal to ideal signal (red) compared to correlation peak of COM model to ideal signal (green) of OFC7-PPM device.

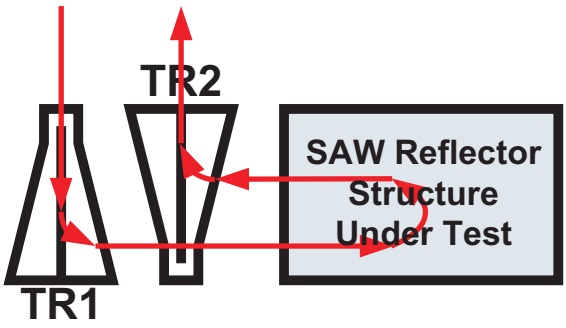

Figure 4.16: Device layout used for reflection measurement. SAW reflector structures used were OFC7, RND7 and OFC7-PPM.

The measured reflected signal is composed of two parts; the direct response (from one transducer to the other) and the reflected response (from one transducer to the reflector grating and then to the second transducer). The two signals can be separated by gating the time domain signal. Once gated, both parts were transformed back into frequency domain. The gated reflected response was then divided by the direct response in order to remove the transducer effect. A threshold was applied at approximately 70 dB below the peak signal to eliminate the noise floor. For this particular device implementation 70 dB threshold yields usable bandwidth of 80 MHz.

4.2.5 Experimental Results of NLR Structures

Figure 4.17 through 4.19 compare experimental data, with the transducer response removed, to the ideal (reflector model) response. Since the experimental data was acquired through a band-limiting transducer, data can only be compared over 80 MHz bandwidth. Remarkable agreement between the experimental data and the ideal reflector model further verifies that the latter is a good synthesis tool.

Figure 4.20 through 4.22 compare ideal auto-correlations to correlations of experimental data and ideal responses. In this case, the ideal transducer effect was

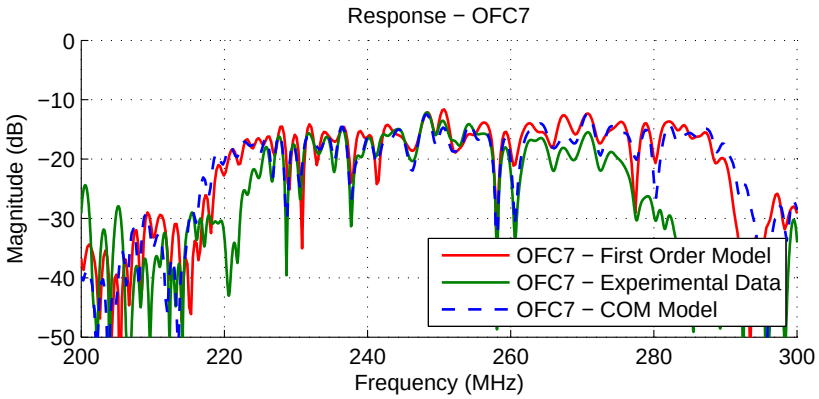

Figure 4.17: Comparison of experimentally measured frequency domain response of OFC7 structure to prediction from the ideal reflector model and COM model.

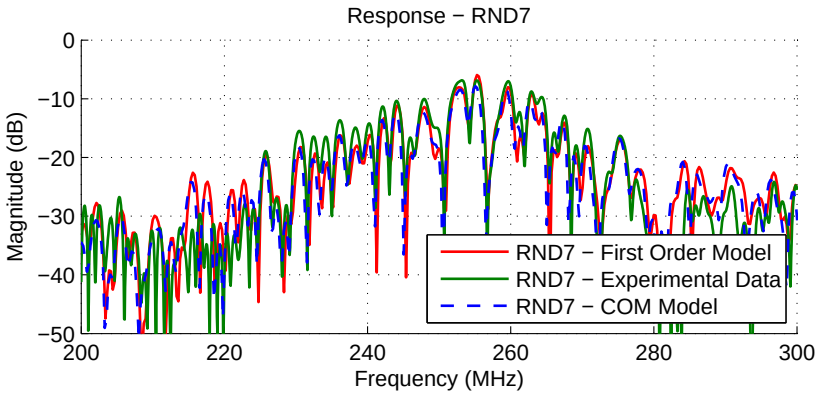

Figure 4.18: Comparison of experimentally measured frequency domain response of RND7 structure to prediction from the ideal reflector model and COM model.

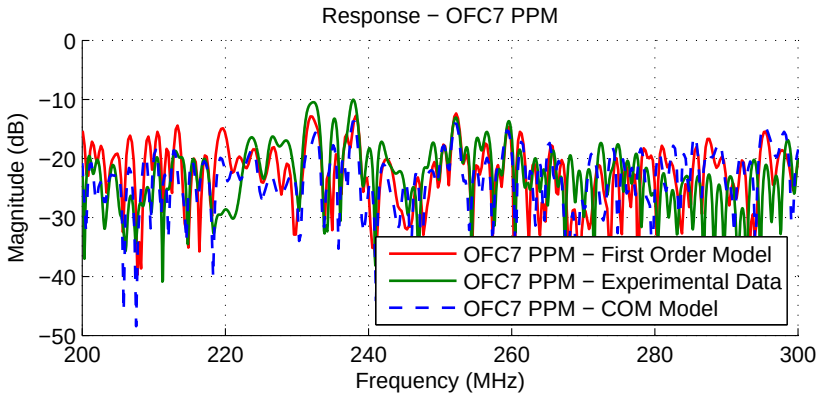

Figure 4.19: Comparison of experimentally measured frequency domain response of OFC7-PPM structure to prediction from the ideal reflector model and COM model.

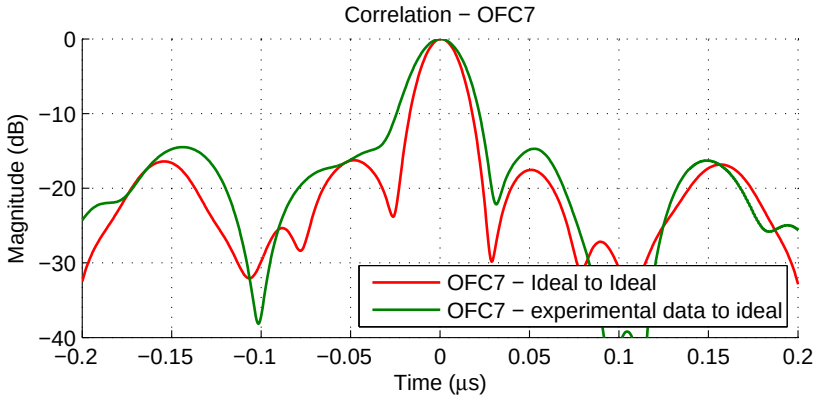

Figure 4.20: Comparison of ideal auto-correlation of device OFC7 to cross-correlation of measured response of device OFC7 and its ideal reflector response.

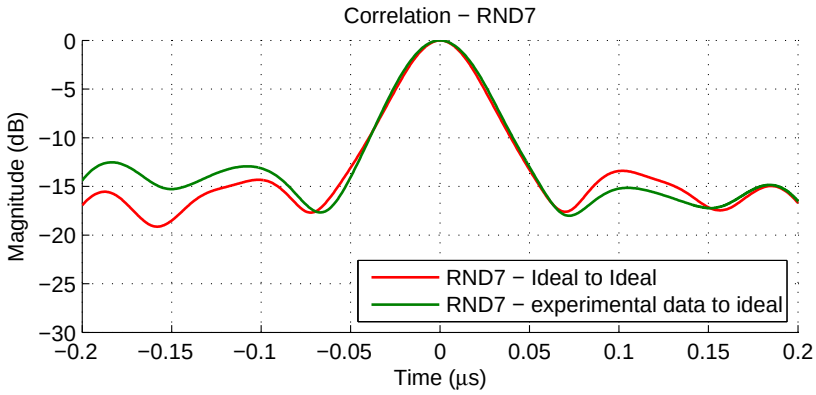

Figure 4.21: Comparison of ideal auto-correlation of device RND7 to cross-correlation of measured response of device RND7 and its ideal reflector response.

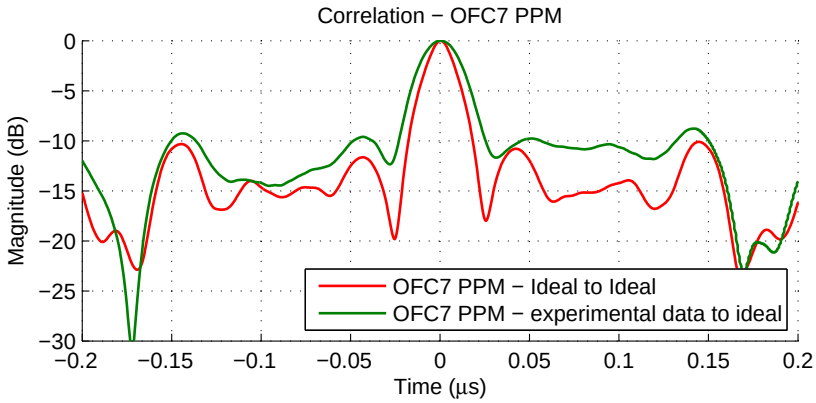

Figure 4.22: Comparison of ideal auto-correlation of device OFC7-PPM to cross-correlation of measured response of device OFC7-PPM and its ideal reflector response.

added to the ideal reflector model, in order to simulate correlation peak degradation. Figure 4.23 compares experimental correlation peaks degraded by transducer effect of the three reflector structures (OFC7, RND7 and OFC7-PPM). Correlation peaks were normalized for comparison purposes.

4.3 Repeating Structures

While NLR devices yield excellent correlation properties, their wide-band nature makes them impractical when considering transducer and interrogator requirements. Simply narrowing bandwidth down could result in significant reflectivity loss. In order to de-spread the reflector response in frequency and create more distinct frequency pass and reject bands, structures can be repeated.

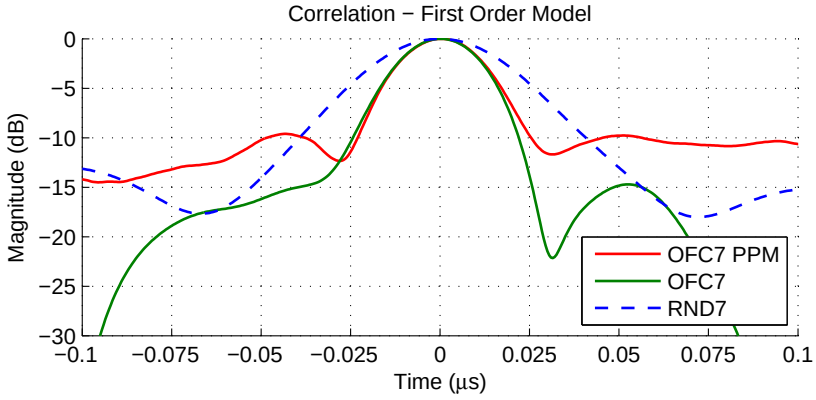

Figure 4.23: Comparison of correlation peaks of experimentally measured OFC7, RND7 and OFC7-PPM reflector structures.

4.3.1 Theory

A first order mathematical analysis is considered, which ignores the acoustic implementation effects. Given a unit cell structure with a time response $h(t)$, and a frequency response $H(f)$, having a time length τ_B and repeated N times, then $h_N(t)$ is given as

$$h_N(t) = \sum_{k=0}^{N-1} h(t + \tau_B \cdot k). \tag{4.13}$$

The frequency response $H_N(f)$ is

$$H_N(f) = \sum_{k=0}^{N-1} H(f)\, e^{-j(4\pi \cdot f \cdot \tau_B)k}. \tag{4.14}$$

Defining

$$\alpha(f) = 4\pi \cdot f \cdot \tau_B, \tag{4.15}$$

equation (4.14) can be reduced to

$$H_N(f) = H(f) \sum_{k=0}^{N-1} \left[e^{-j \cdot \alpha(f)}\right]^k. \tag{4.16}$$

The summation in equation 4.16 is recognized as a geometric progression and using the summation formula for such a progression, equation (4.16) yields [55]

$$H_N(f) = H(f) \cdot \frac{1 - e^{-j \cdot N \cdot \alpha(f)}}{1 - e^{-j \cdot \alpha(f)}}. \tag{4.17}$$

Factoring out the exponents, applying Euler's formula, and back substituting using equation (4.15), $H_N(f)$ can be expressed as a product, rewritten as

$$H_N(f) = H(f)\, e^{-j \cdot (N-1) \cdot 2\pi \cdot f \cdot \tau_B} \frac{sin(N \cdot 2\pi \cdot f \cdot \tau_B)}{sin(2\pi \cdot f \cdot \tau_B)}. \tag{4.18}$$

The peak frequencies occur when

$$2\pi \cdot f_{peak} \cdot \tau_B = n \cdot \pi, \tag{4.19}$$

where $n \in \mathbb{N}$, or

$$f_{peak} = \frac{n}{2 \cdot \tau_B}. \tag{4.20}$$

The relationship to the frequency nulls is

$$N \cdot 2\pi \cdot f_{null} \cdot \tau_B = m \cdot \pi, \tag{4.21}$$

where $m \in \left\{\mathbb{N} : \frac{N}{m} \notin \mathbb{N}\right\}$ and

$$f_{null} = \frac{m}{2 \cdot \tau_B \cdot N}. \tag{4.22}$$

The null bandwidth is given as

$$BW_{null} = \frac{N \cdot n + 1}{2 \cdot \tau_B \cdot N} - \frac{N \cdot n - 1}{2 \cdot \tau_B \cdot N} = \frac{1}{\tau_B \cdot N}. \tag{4.23}$$

$H_N(f)$ is expressed as a product of $H(f)$, which is the unit cell frequency response, a linear phase term of unity magnitude, and a real, modulating function. Figure 4.24 is an example response of $H_N(f)$, for $N = 2, 3, 4$ and $H(f) = 1$. Expressions for peak and null locations and peak bandwidth are given in equations (4.20), (4.22), and (4.23), respectively.

This simple analysis is applicable to idealized short reflector arrays. It assumes the inter- and intra-reflections are negligible and that the electrode reflection is approximately equal to a half-wavelength at the local carrier frequency, or where the period is $^1/_2$ wavelength. This is not always true, as will be demonstrated, but it

provides an understanding of what is expected and a direction for experimentation. As seen in Figure 4.24, a series of periodic stop bands will be produced due to the multiple periodic unit cells creating the super cell. This would correspond to the idealized reflector response of such a structure. By changing the unit cell and/or super cell, differing stop (reflection) and pass bands can be achieved.

4.3.2 Layout of Devices with Repeating Structures

A total of eight devices were modeled, built, and tested. All of the devices were one-port devices and had a $3 \cdot f_0$ apodized transducer which reduced second order transducer effects. To verify the theory developed in section 4.1, an OFC structure was initially chosen as a unit cell for its well behaved and slowly changing frequency response, $H(f)$. This response should give good verification of peak and null locations

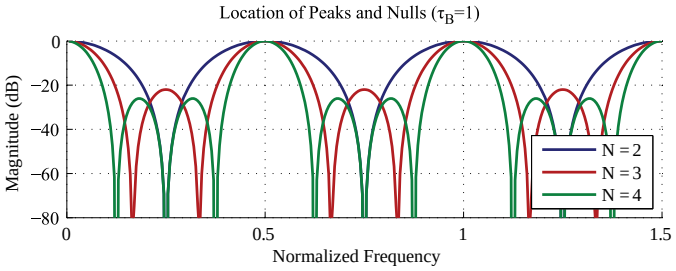

Figure 4.24: Example of normalized magnitude frequency response from the ideal reflector model calculations for super cells with 2, 3 and 4 unit cells. As N increases, the local stopband frequencies narrow. The effects of increased reflectivity and inter- and intra- reflector interactions are not predicted in the ideal reflector model.

Table 4.2: OFC Device Design Values for Repeating Structures Experiment

	Frequency (MHz)	**Number of electrodes**	**Position**
f_1	245.2	25	1
f_2 (f_0)	250.0	26	2
f_3	254.8	27	3

and predicted bandwidth. A 3-chip OFC structure was designed to have frequencies 245.2MHz, 250.0MHz, and 254.8MHz with 25, 26 and 27 electrodes respectively (as shown in Table 4.2). A shorter, 3-chip configuration was chosen as opposed to 5-chip devices in Section 4.2 to avoid having long devices and second order effects associated with them. Super cells were built from OFC bits repeated 1, 2, 3, and 4 times as shown in Figure 4.25. Devices were then labeled as OFC x1, OFC x2, and so on. Primitive structures were designed which have $p_i = 0.5\lambda_i$, $x_i = d_i = 0$, and $a_i = 0.25\lambda_i$, where λ_i is corresponding wavelength to each frequency.

Also, a random structure was used as a unit cell for a second set of four devices. This structure was built using the primitive cells from the previously described OFC structure. Primitive structures (electrode followed by free space each of quarter wavelength width) were randomly shifted within the unit cell, yielding the same total number of electrodes and length of the unit cell as described for OFC. This

unit cell was then repeated similarly to then OFC xN devices; 1, 2, 3 and 4 times as shown in Figure 4.26, and labeled RND x1, RND x2, and so on.

The second set of random and pseudo-random devices provided a unique reflectivity response and was also used to examine the accuracy of the COM model when simulating fast changing structures. The COM model has been shown to be accurate for slowly varying changes in electrode periodicity [7]. The random unit cell structure can have rapidly changing primitive cell characteristics, which may challenge the applicability of the COM model.

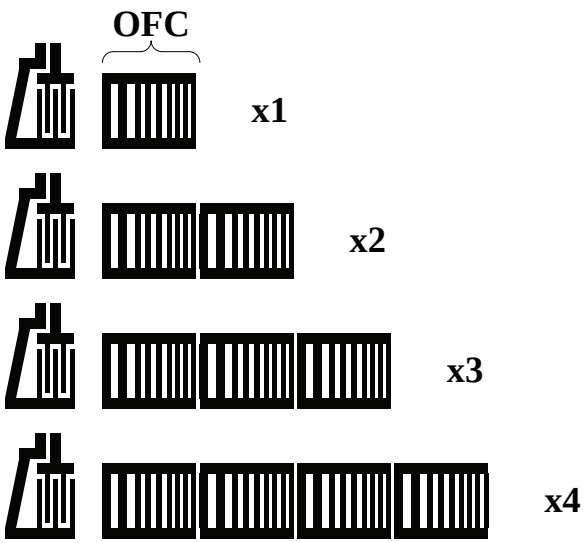

Figure 4.25: OFC bit device layouts (drawing is not to scale, nor does it show the correct number of electrodes), structures. Because there can be defined a unit cell, which is repeated within the structure, the structure is pseudo-periodic.

4.3.3 Modeled Results for Repeating Structures

Two models were used to design and predict the device response. The ideal reflector model was primarily used to provide an analytic design tool; it has simple equations and gives the ability to develop design algorithms. The reflector response is approximated by idealized time carriers dependent on the period of the electrode modeled. It does not take under consideration coupling, inter-reflectivity, and second order effects. Reflection is linearly proportional to the number of electrodes and does not model the stored energy in the device. For a more complete analysis, which includes

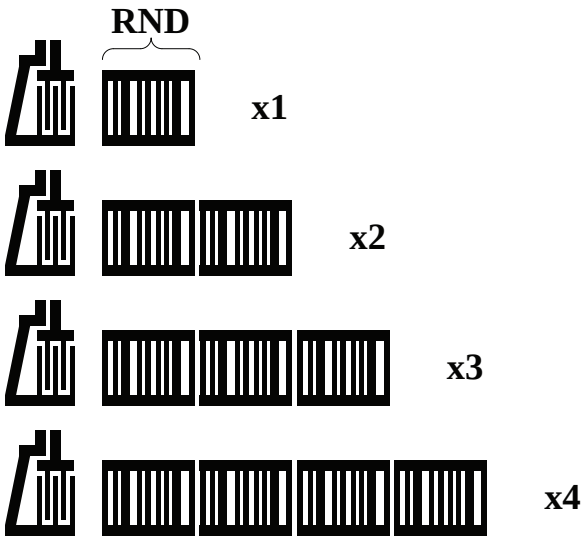

Figure 4.26: Random bit device layouts (drawing is not to scale, nor does it show correct number of electrodes). For device RNDx1, the unit cell consists of totally random primitive cells, but the super cells in the other devices are pseudo-random, consisting of RNDx1 periodically used in the super cell.

coupling, inter-reflectivity and second order effects, the COM model is applied to the structures [7].

Both models define one primitive structure (electrode) at a time. Also, both models produce the expected reflective S-parameter of the acoustic ports. Acoustic ports cannot be measured directly, which requires transducers for launching and receiving the SAW and their effect needs to be compensated when extracting the data.

Figure 4.27 shows the COM model predicted frequency response of OFC x1 through OFC x4 devices. Peaks, nulls, and bandwidth correlate well with theory developed in section 4.1. In this case the bit length τ_B is approximately .9μs. As expected, the unit cell response, OFC x1, defines the reflection band window in fre-

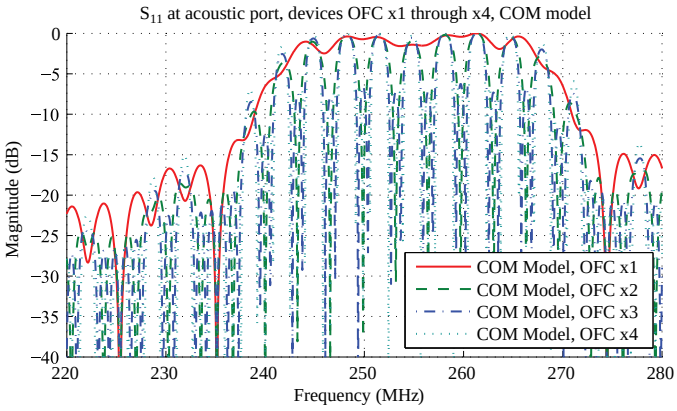

Figure 4.27: COM model predicted reflector frequency response of devices OFC x1 through OFC x4 (output is normalized for comparison).

quency. The periodic reflection bands are determined by the periodic unit cell delay and number of unit cells in the super cell.

Figure 4.28 shows a narrower frequency interval of the same response as shown in Figure 4.27, demonstrating the null bandwidth variations and the relative change in reflectivity as the super cell length increases. This plot can also be compared to the plot of Figure 4.24.

Figure 4.29 shows the COM model frequency response for the devices composed of the randomized unit cell. The general positions of peaks and nulls are close to those predicted by the ideal reflector model, but the peak around 255MHz is saturated due to the inter- and intra- reflectivity effects, which is not predicted by equation (4.23). The character of the reflector response is very diverse, owing to the uniqueness of the random structure of the unit cell. The periodicity is a function of the primitive cell delay offset.

4.3.4 Measurement of Repeating Structures

It is not possible to measure acoustic ports of reflector banks (super cells) directly. Data was acquired through a transducer using a network analyzer and then transformed into the time domain using the Fourier transform. The super cell reflection

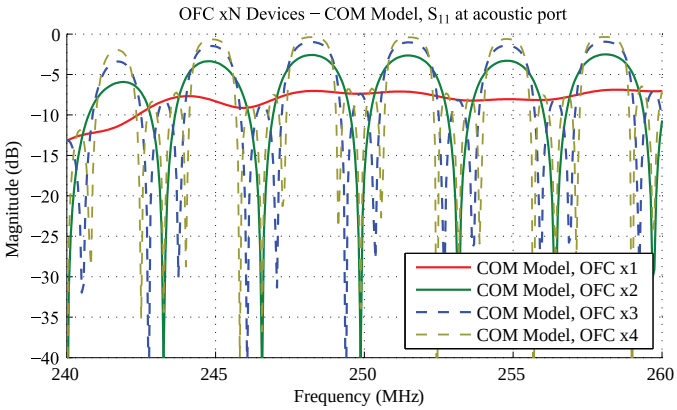

Figure 4.28: COM model predicted reflector frequency response of devices OFC x1 through OFC x4 (output is not normalized).

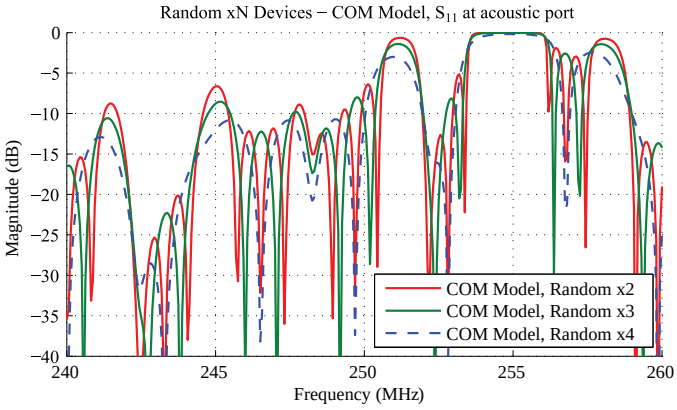

Figure 4.29: COM model predicted reflector frequency response of devices RND x1 through RND x4 (output is not normalized), with relative magnitudes.

has been gated out in the time domain and transformed back into the frequency domain. The transducer response has been measured separately and then compensated for in the response of the super cells. The experimental reflector responses have been compensated, eliminating the transducer response effect, providing the proper reflector magnitude frequency response.

The COM simulation parameters were adjusted slightly to align the frequency nulls (velocity change) and the reflectivity was fixed to match measurements made from test structures on the same wafer. These model parameters will need further study for these structures, but the transfer function is presently the parameter of interest.

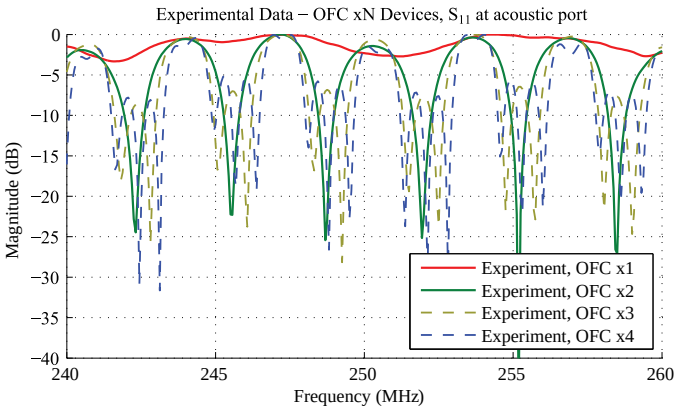

Figure 4.30: Experimental reflector frequency response of devices OFC x1 through OFC x4 (output is normalized). This result compares well to the predicted response of Figure 4.28.

Figure 4.30 shows the experimental frequency response of OFC x1 through OFC x4 devices. It can be noted that the number of peaks, their relative location, and bandwidths correlate well with ideal reflector model (Figure 4.24) and COM model simulations (Figure 4.28).

Figure 4.31 shows the normalized expanded frequency response of device OFC x1, which is a super cell consisting of just one OFC bit. This response represents the unit cell, $H(f)$ in section 4.1. Devices OFC x2, x3, and x4 are expected to generate the desired peaks and nulls within this frequency response window. For this device both models and the data correlate well.

Figure 4.32 shows the frequency response of a super cell consisting of two bits (2-unit cell). At this point both models and experimental data agree with an exception of the high frequencies where there appears to be a slight ripple.

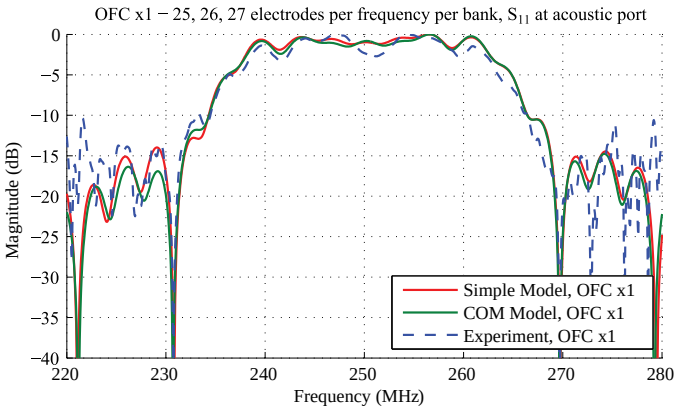

Figure 4.31: Predicted reflector frequency response of ideal reflector model and COM model compared to experimental data for OFC x1 device.

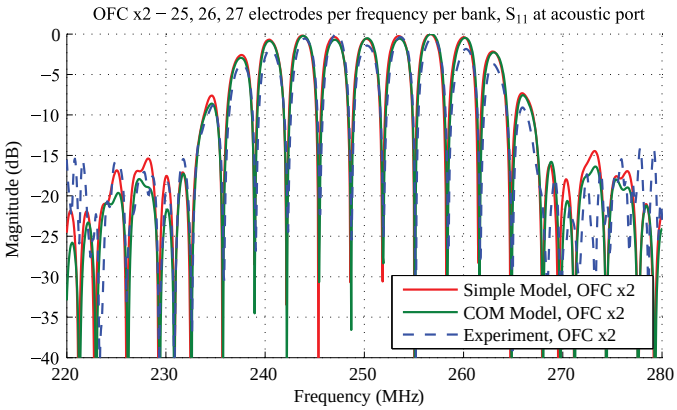

Figure 4.32: Predicted reflector frequency response of ideal reflector model and COM model compared to experimental data for OFC x2 device.

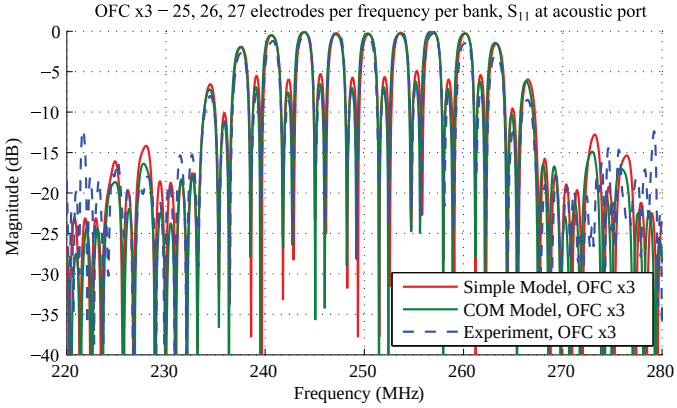

Figure 4.33: Predicted reflector frequency response of ideal reflector model and COM model compared to experimental data for OFC x3 device.

Figure 4.33 and Figure 4.34 show responses of super cells with 3 and 4 bits, respectively. The overall character of the frequency responses is predicted quite well, however, there is a ripple within the reflection bands. At this point it is not clear the reason the experimental devices have this ripple, but it may be due to the device layout, mode conversion, fabrication, or some other effect. Future research on long super cell structures is required to explain this effect.

Figure 4.35 shows the normalized frequency response of device RND x1, which is a unit cell consisting of random, different primitive cells. This corresponds to $H(f)$ in section 4.1. Again, the RND x1 response is expected to act as the frequency window as the super cell increases in length. The comparison of measured and predicted responses is quite good. The response has unique character dependent on the nature of the unit cell, demonstrating the results of the randomized primitive cells.

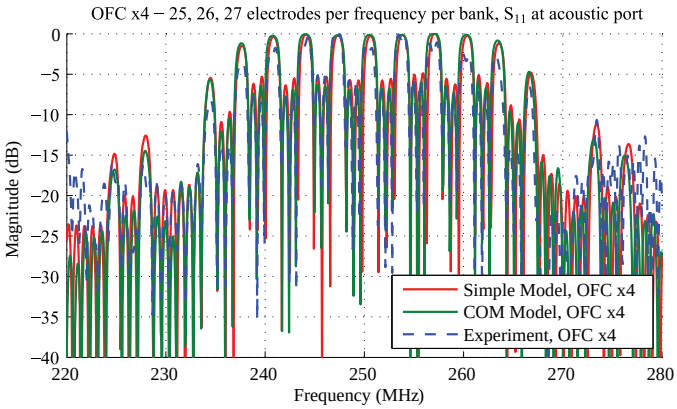

Figure 4.34: Predicted reflector frequency response of ideal reflector model and COM model compared to experimental data for OFC x4 device.

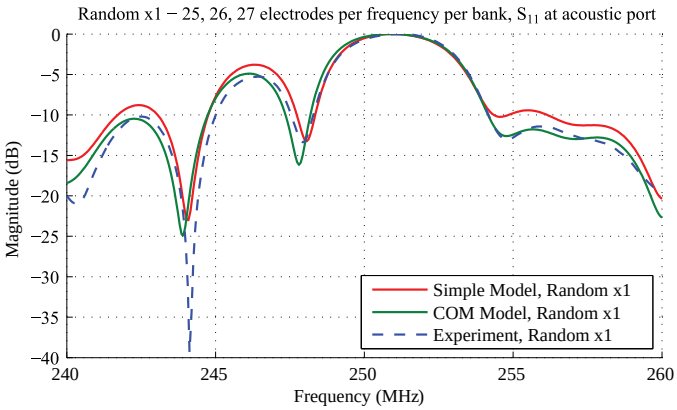

Figure 4.35: Predicted reflector frequency response of ideal reflector model and COM model compared to experimental data for RND x1 device.

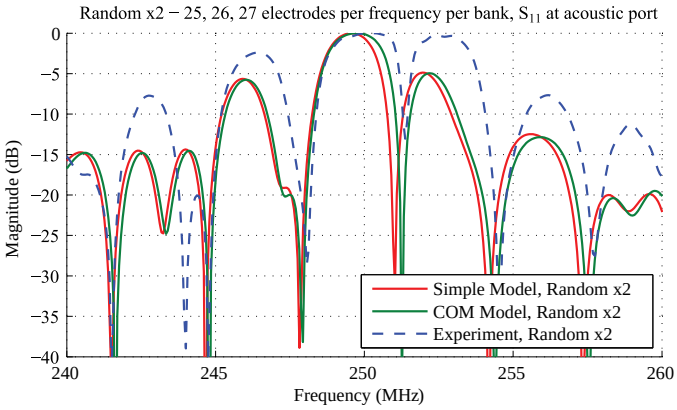

Figure 4.36: Predicted reflector frequency response of ideal reflector model and COM model compared to experimental data for RND x2 device.

Figure 4.36 shows modeled and measured frequency responses of a super cell consisting of two random unit cells. The nulls and peaks are predicted quite well, but the experimental data shows a much stronger reflectivity than predicted, evidenced by the higher side-lobes and broader stop bands.

Figure 4.37 and 4.38 show responses of super cells with 3 and 4 random unit cells, respectively. The general measured frequency response characteristics agree between predictions and measurements is evident; however, there is greater divergence between all the plots. The COM model is much closer to the experimental measurements than the simple model since strong reflectivity can be taken into account. It appears that the COM model reflectivity should be decreased, which would result in a narrowing of the null spacing and a smoothing of the peak frequency responses. COM model also does not take under consideration additional loss term

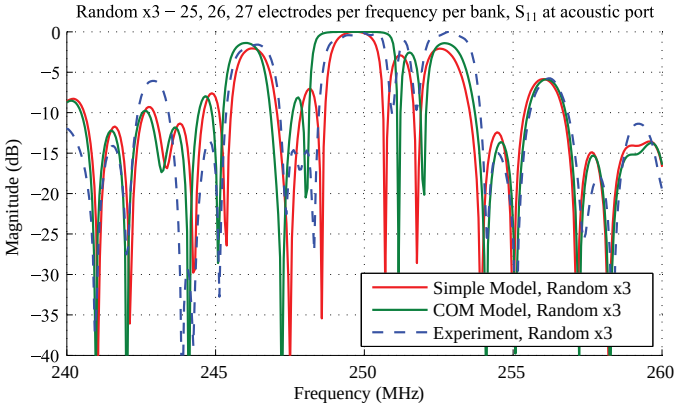

Figure 4.37: Predicted reflector frequency response of ideal reflector model and COM model compared to experimental data for RND x3 device.

associated with waves traveling underneath the reflector grating. This loss term may make reflectivity seem less and it becomes more prominent for long devices such as RND x4. The 4-cell reflector begins to show ripples, similar to that seen in the OFC 3- and 4-cell structures. At this point it is not clear the reason the experimental devices have this ripple. It may be due to the device layout, mode conversion, fabrication, or some other effect not included in COM model, again, future research on long super cell structures is required.

4.4 Cell-based Device Coding

In a typical digital communication system, a number of active components are designated to ensure that multiple devices do not conflict with each other. A base station

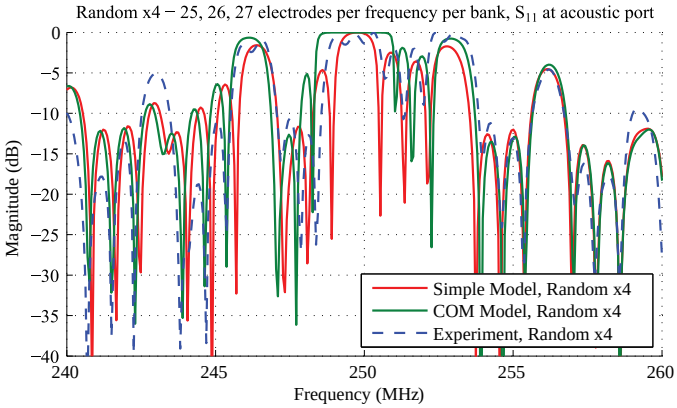

Figure 4.38: Predicted reflector frequency response of ideal reflector model and COM model compared to experimental data for RND x4 device.

typically tells the devices when to talk, when not to talk, how much power to output and which frequency to use. This is done through the handshaking and the ongoing monitoring of the devices within the environment. Also, when the received digital signal is correlated, shape and quality of the correlation peak is not as important as long as it is detectable and the phase can be determined.

4.4.1 Designing Codes for Multi-sensor System

In a passive wireless system, once the device is in place, it will use fixed frequencies at fixed times and output (reflected) power that cannot be controlled by the base station. Correlation of the sensor of interest is computed together with cross-correlations of all the other devices present in the system. In order to extract accurate data from a sensor, the auto-correlation peak must be unaffected by the presence of all the other cross-correlations. In other words, cross-correlations of other devices need to be minimal (ideally zero) in the proximity of the main auto-correlation peak.

Codes must be designed in such way that at any given time each sensor is either silent or occupies its own frequency band(s). An OFC device is composed of a number of OFC chips that are located in assigned time slots. For multiple OFC

devices operating without collisions, for any one given time slot OFC chip of a certain frequency can only be used in one device.

A relationship can be established between the number of chips used to make up one device (n), number of chips that are allowed to be used within the same time slot (m), number of devices required (N), and number of time slots (M) given as

$$M = \left\lceil N \cdot \frac{n}{m} \right\rceil, \tag{4.24}$$

based on the fact that the total number of chips in the system across all devices is

$$\text{Total Number of Chips} = N \cdot n = M \cdot m. \tag{4.25}$$

Figure 4.39 shows 16 codes for a 16-device system, that uses seven OFC chips. In the table each row is a code, each column is an OFC-chip length time slot. Cells with zeros are unused time slots of a particular code and cells with values 1-7 are time slots with OFC chips of orthogonal frequencies 1-7.

Figure 4.40 shows the schematic drawing of the first two codes of Figure 4.39 as implemented into actual devices. The 16-code system was then simulated using the first order model discussed in Chapter 3. In Figure 4.41 an auto-correlation of one device (blue) was compared to the correlation of the matched filter for that device

Device Number (N=16) \ Time Slot Number (M=16)	1	2	3	4	5	6	7	8	9	10	11	12	13	14	15	16
1	0	0	7	5	3	0	0	0	6	0	0	2	0	1	0	4
2	4	5	0	0	0	2	6	7	0	1	3	0	0	0	0	0
3	5	4	3	6	0	0	0	0	0	0	7	0	1	0	2	0
4	0	0	0	0	5	0	1	3	0	2	0	0	6	4	0	7
5	0	0	0	0	0	3	0	5	2	7	0	1	0	6	4	0
6	7	0	4	3	1	6	2	0	0	0	0	0	0	0	5	0
7	0	6	0	0	0	7	0	0	1	0	5	3	4	0	0	2
8	2	7	1	0	6	0	3	0	0	0	0	4	0	5	0	0
9	0	0	0	0	0	0	0	4	3	5	6	0	2	0	7	1
10	0	0	0	1	2	5	7	0	0	4	0	6	0	0	3	0
11	0	3	6	2	0	0	0	1	0	0	4	0	5	7	0	0
12	1	0	0	0	7	0	5	0	4	0	0	0	0	2	6	3
13	0	0	2	4	0	1	0	0	5	0	0	7	3	0	0	6
14	6	1	5	7	0	0	4	0	0	3	2	0	0	0	0	0
15	3	0	0	0	4	0	0	2	0	6	0	0	7	0	1	5
16	0	2	0	0	0	4	0	6	7	0	1	5	0	3	0	0

Figure 4.39: A sample set of 16 OFC devices using 16 time slots and 7 frequencies.

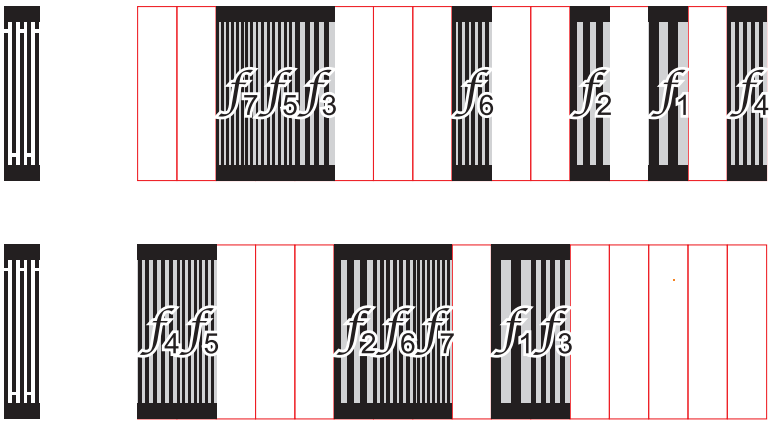

Figure 4.40: Two sample devices realized using codes 1 and 2 from Figure (4.39).

to the entire system with all the 16 codes (green). It can be noted that the main auto-correlation peak was not affected significantly by the presence of all the cross-correlations. Also note that even the two main side-lobes of the auto-correlation have not been affected significantly, which means that even if the location of the auto-correlation peak shifts due to a sensor parameter change, within a certain distance it still will not collide with the other cross-correlations. The amount by which the peak can change its position while being unaffected is one of the factors that will determine the dynamic range of the system and its physical spread in space. Even though only one device is demonstrated, this is representative of all the 16 devices. This cell-based approach to device coding produces codes with excellent anti-collision properties.

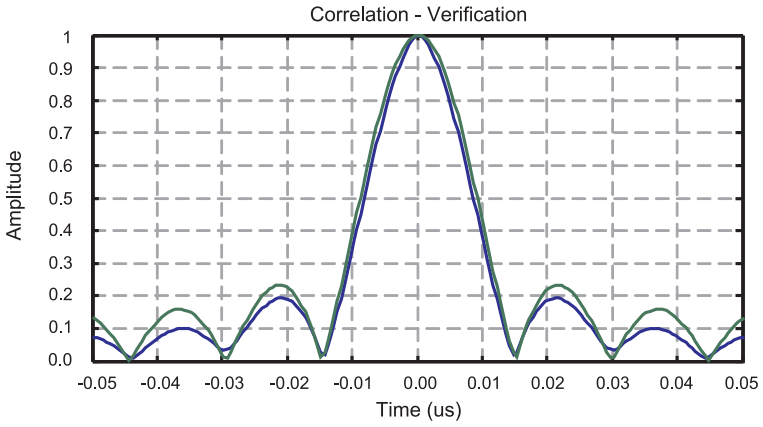

Figure 4.41: Comparison of auto-correlation of a single device to correlation of that device to the entire system (sum of 16 devices).

4.4.2 NLR Structures and Device Scaling

Previous work has shown that the noise-like reflector (NLR) structures are wide-band with random pass- and reject-bands and can produce codes with good auto-correlation and anti-collision properties [53]. At this time such reflectors are generated at random. Once a set of devices with NLR structures is generated, each cross-correlation needs to be examined for the anti-collision properties. If one or more of the cross-correlations do not have the desired anti-collision properties, the entire set has to be discarded and a new one is generated until all cross-correlations are satisfactory. For sets with large number devices and large number of electrodes this code set selection process could be time and resource consuming.

Proposed in this section is a new and novel approach for the code generation where instead of the OFC chips, NLR chips are used. The chips are much shorter than the entire code and fewer chips are needed to build up larger number of codes, which significantly reduces time and resources needed for good NLR chip selection.

First, it is important to establish how a NLR chip is constructed. Shown in Figure 4.42 is a diagram of a portion of a NLR chip. The NLR structure is created by taking a regular reflector bank and inserting free space (shown in blue) between electrode-gap pairs (shown in red and light red). As the amount of inserted free

space increases, anti-collision properties improve. In this particular case, quarter-wavelength electrodes are used, making an electrode-gap pair half-wavelength long. Inserted free space is an integer multiple (shown as K in Figure 4.42) of a quarter-wavelength, which makes electrodes randomly in-phase or 180° out of phase.

Two OFC chips with adjacent frequencies have cross-correlation lobes to main auto-correlation peak ratio of 0.32. Same ratio for two OFC chips with one over adjacent frequencies is 0.17, as described in Chapter 2.3. Since NLR chips are random, only probability of having cross-correlation lobes to main auto-correlation peak ratio below a certain level can be determined: analytical expression is difficult to calculate; it would have to factor in the electrodes representation as sine waves and the

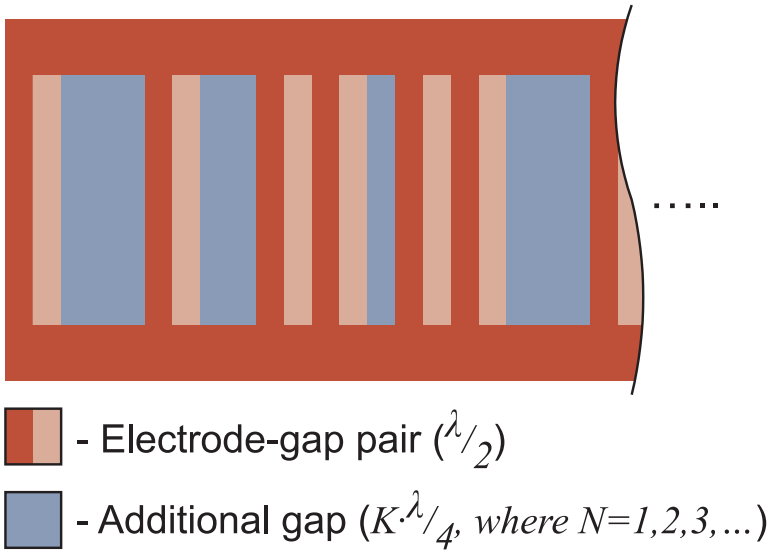

Figure 4.42: Construction of a NLR chip.

band-limiting transducer effect. It is, however, possible to determine this probability by analyzing large numbers of NLR chips sets. Shown in Figure 4.43 is chip collision analysis. Due to changes in temperature and spacial position, the auto-correlation peak will move within a certain time window (a dynamic range) (τ_{DR}),which is a parameter considered at the design time. Chip length (τ_{C-OFC} is generally an upper boundary for possible τ_{DR} values, but τ_{DR} is generally not a function of τ_{C-OFC}. For an OFC-based system, the auto-correlation will be affected by cross-correlation of other chips. For adjacent frequency chips, the maximum cross-correlation peak to auto-correlation lobe ration (MCAR) is 0.32 and for one over adjacent frequency MCAR is 0.17. In order to generate comparable NLR-based system, randomly generated NLR chips need to have MCAR value of 0.2 with in the τ_{DR}. The dynamic range window (τ_{DR}) for the OFC- and NLR-based systems is the same. However, NLR chip length is generally longer than an OFC chip length. MCAR is applied to all possible cross-correlations.

Figure 4.44 shows the probability finding two NLR chips with cross-correlation lobes below a certain level; each chip has 16 electrodes at 250MHz center frequency randomly distributed within 312 ns window with average integer multiple for inserted free space K=7.75 and a 150MHz null-bandwidth transducer.

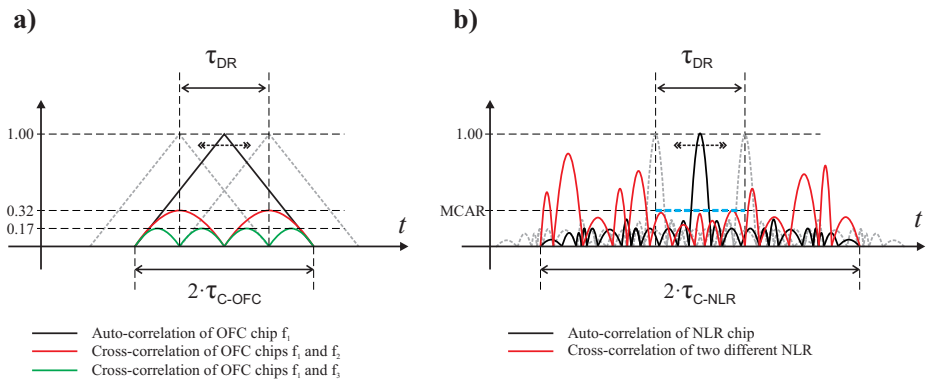

Figure 4.43: Demonstration of chip collisions: a) auto-correlation (black) and cross–correlations (red and green) of OFC chips, and b) auto-correlation (black) and cross–correlation (red) of NLR chips.

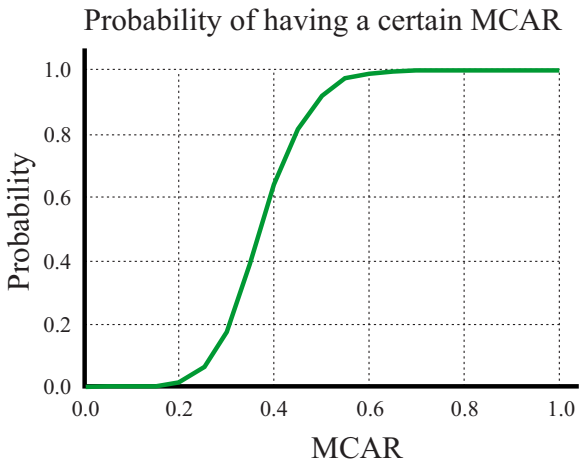

Figure 4.44: Probability of having a certain MCAR for a two NLR-chips with 16 electrodes semi-randomly (as shown in Figure 4.42) distributed within 312 ns.

From Figure 4.44, it can be noted that it is possible to generate two NLR chips with MCAR lower than 0.2, which is comparable to OFC chips. In order to compete with the OFC approach, more NLR chips are needed. For N NLR chips, the number of cross-correlations needed to be examined is $\frac{1}{2}(N^2 - N)$. After generating and analyzing numerous 4-NLR-chip sets a few sets were found where MCAR was just below 0.3 of the average of the four auto-correlation peaks of their respective NLR chip set.

The odds of finding good codes rapidly decreases with the number of codes needed. One way to produce more codes is to simply scale the physical dimensions of the reflector bank leaving the code the same. Figure 4.45 shows the maximum cross-correlation lobe when correlating one code with its scaled versions. If a code is scaled to 1.01 (by 1%) of its original physical dimensions, maximum cross-correlation is reduced to 10% of the auto-correlation peak. Scaling physical dimensions of a 250MHz device by factor of 1.04 produces a 260MHz device, similar to OFC chips. Bandwidth of the system does not change with reflector scaling and is dependent on the transducer of the SAW devices.

A 12-sensor system was designed using the NLR approach with scaling and simulated using the first order model discussed in section 3. Four unique NLR chips were randomly generated and selected based on having all cross-correlation lobes to main

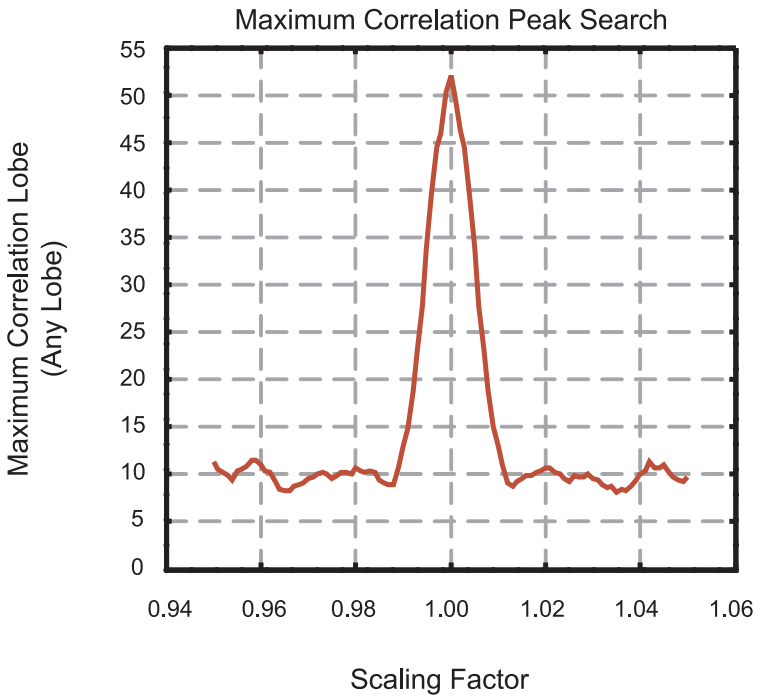

Figure 4.45: Highest correlation lobe of correlation of one NLR chip to the another NLR chip with the same code but scaled to a different frequency.

auto-correlation peak rations below 0.3. Each NLR chip consists of 16 electrodes at 250MHz center frequency randomly distributed within a 312ns window with an average integer multiple for inserted free space K=7.75. These codes where scaled to two more frequencies (240MHz and 260MHz), producing a total of 12 NLR-chips. An unapodized transducer with 150MHz null-bandwidth used in simulation and with four NLR chips per device were used. The number of time slots needed was determined to be 4 based on equation (4.2). The codes are shown in Figure 4.46, where each row is a code and each column is a time slot. In this case, each NLR-chip (cell) is denoted by two numbers (f, g), where f is the NLR code number 1 through 4 and g is an index of the frequency used: 1, 2 and 3 that correspond to 240MHz, 250MHz and 260MHz, respectively.

Shown in Figure 4.47 is the auto-correlation of one of the 12 codes compared to the correlation of that code to the entire system (sum of all the 12 codes). Shown is an average performing device in terms of the anti-collision properties. The main correlation peak of the code to the system shown in Figure 4.47 is approximately 4% lower than the auto-correlation of just that one code by itself, which is indicative of code collision, also the presence of the cross-correlation lobes close to the auto-correlation peak indicates potentially smaller dynamic range of the NLR-based

Device Number (N=12) \ Time Slot Number (M=4)	1	2	3	4
1	(4,2)	(2,2)	(4,3)	(2,1)
2	(1,2)	(1,3)	(2,3)	(3,1)
3	(1,3)	(3,3)	(4,1)	(1,1)
4	(4,3)	(2,3)	(1,3)	(3,3)
5	(2,2)	(2,1)	(1,1)	(1,2)
6	(4,1)	(4,2)	(2,2)	(3,2)
7	(3,2)	(3,1)	(3,3)	(4,3)
8	(3,3)	(4,3)	(2,1)	(2,3)
9	(1,1)	(3,2)	(1,2)	(4,1)
10	(2,1)	(1,2)	(3,2)	(1,3)
11	(3,1)	(1,1)	(4,2)	(2,2)
12	(2,3)	(4,1)	(3,1)	(4,2)

Figure 4.46: NLR-based code set, each NLR chip is denoted by two numbers (g, f), where g is NLR code number and f is an index of the frequency used.

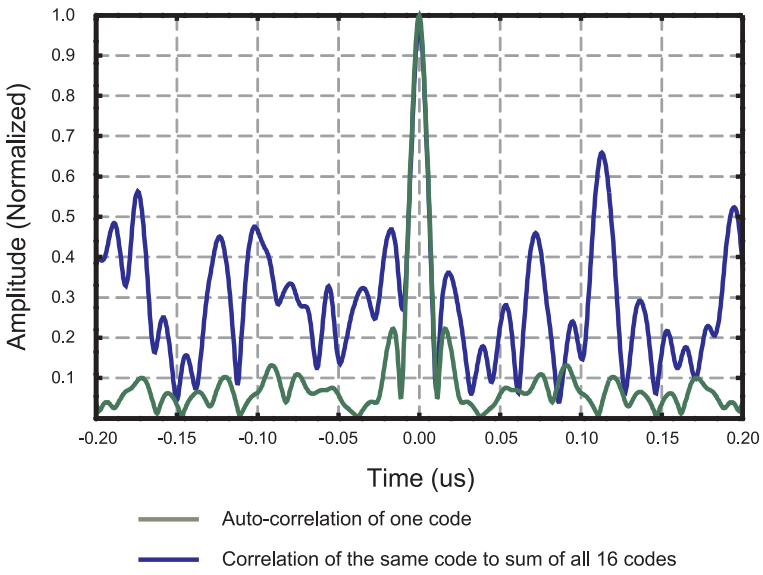

Figure 4.47: Comparison of auto-correlation of a single device to correlation of that device to the entire system (sum of 12 devices).

system than in the case of the OFC-based system. However, due to a higher number of possible codes, NLR-based system can be a viable approach for tag applications.

4.4.3 Experimental Devices and Cell-based Coding Technique

4.4.3.1 OFC-based System

In order to assess the differences in the performance of the NLR-based and the OFC-based approaches, the two code sets were designed to have as many parameters in common as possible. The OFC-based system was designed based on the NLR-based system described in section 4.4.2. The following parameters were used for both systems and as similar as possible: number of the electrodes per reflector bank, time length of each reflector bank, and a wide-band transducer. One of the possible solutions for the OFC-based system meeting these requirements consisted of three OFC chips (240MHz, 250MHz and 260MHz with 25, 26 and 27 electrodes respectively), each chip had time response length of $0.104\mu s$. In order to produce 12 codes, 12 time slots and 3 chips per device were used. Each device has 78 electrodes and on average approximately $1.04\mu s$ time response length. Codes used for the OFC-based system

are shown in Figure 4.48. Only three of the 12 devices were fabricated. Devices were fabricated on Y,Z $LiNbO_3$. One of the devices is demonstrated in Figure 4.52.

Since the temperature is most likely to vary as a function of time, this parameter was measured (temperature extraction was performed as described in Chapter 2.4). Figure 4.50 compares the correlation of the measured and the ideal responses and the auto-correlation of the ideal response. The plot shows very good agreement between the first order model and the experimental data. The two other devices were also measured and added to the first measured device. This sum was correlated against the ideal response of the first device and compared the ideal auto-correlation of that

Time Slot Number (*M=12*)

Device Number (*N=12*)	1	2	3	4	5	6	7	8	9	10	11	12
1	0	1	0	0	3	2	0	0	0	0	0	0
2	1	0	0	0	0	0	0	0	0	0	3	2
3	0	0	0	1	0	0	2	0	3	0	0	0
4	0	0	0	2	0	0	0	3	1	0	0	0
5	2	0	0	0	0	1	0	0	0	3	0	0
6	0	3	2	0	0	0	1	0	0	0	0	0
7	0	0	0	0	2	3	0	0	0	0	1	0
8	0	0	1	3	0	0	0	2	0	0	0	0
9	3	0	0	0	0	0	0	0	2	1	0	0
10	0	0	0	0	0	0	3	0	0	0	2	1
11	0	0	0	0	1	0	0	0	0	2	0	3
12	0	2	3	0	0	0	0	1	0	0	0	0

Figure 4.48: OFC-based code set, each cell with number 1, 2 or 3 corresponds to an OFC chip with center frequency 240MHz, 250MHz or 260MHz respectively, and each cell with zero corresponds to an unused time slot for that particular device.

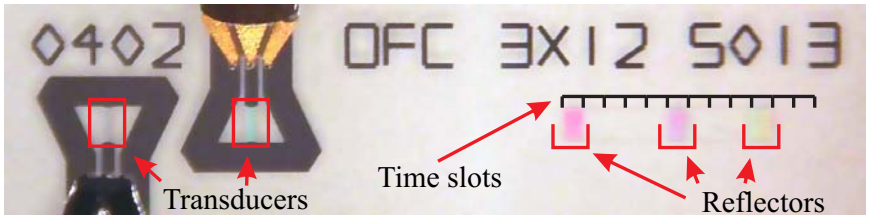

Figure 4.49: Fabricated device (device #5 of Figure 4.48) with 3 OFC chips coded using cell-based method with 12 time slots.

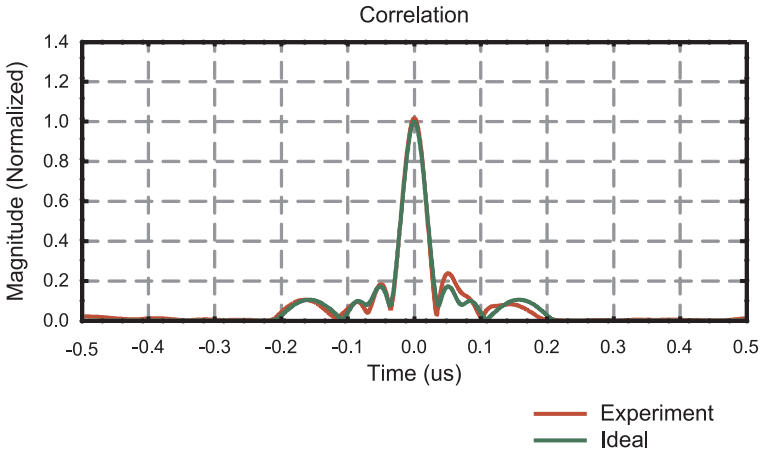

Figure 4.50: Comparison of auto-correlation of an ideal OFC device (green) to correlation of experimental data and the ideal reflector response (red).

device as shown in Figure 4.51. It can be noted that while the two adjacent lobes to the main peak did go up, the peak is not affected by the presence of the two other devices. This clearly demonstrates the anti-collision properties of the OFC-based devices coded using the cell-based approach.

4.4.3.2 NLR-based System

The NLR-based system was built using codes described in section 4.4.2. The electrode count per reflector bank is 64 and average time length response is approximately $1.2\mu s$. Three of the 12 devices were built on Y,Z $LiNbO_3$.

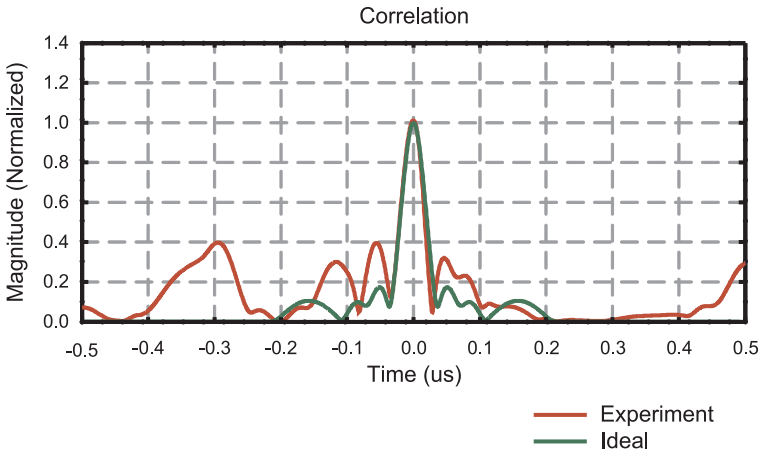

Figure 4.51: Comparison of auto-correlation of a single ideal OFC device response to correlation of ideal OFC device response and sum of 3 devices measured experimentally.

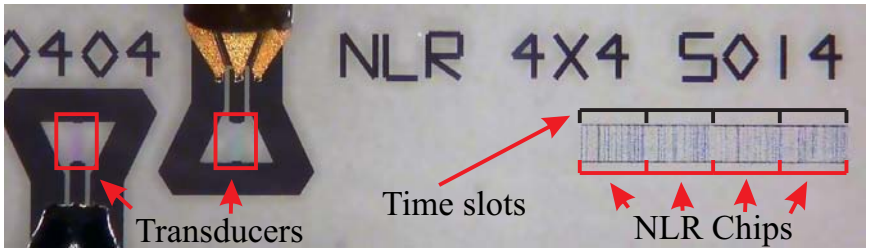

Figure 4.52: Fabricated device with 4 NLR chips coded using cell-based method (device #4 of Figure 4.46) with 4 time slots and total number of 12 of unique NLR chips available for codes

Photograph of one of the NLR-based devices is shown in Figure 4.52. Figure 4.53 compares the correlation of the measured with the ideal response, and the auto-correlation of the ideal response. Plot shows good agreement between the first order model and the experimental data. The two other devices were then measured and added to the first measured device. This sum was correlated against the ideal response of the first device and compared the ideal auto-correlation of that device as shown in Figure 4.54. It can be noted that the peak was not affected by the presence of the two other devices; however, a cross-correlation lobe appeared at the base of the auto-correlation peak. At fixed temperature, this device demonstrates that the NLR-based approach provides good anti-collision codes. It can also be noted, that the auto-correlation peak of the NLR device is narrower than the auto-correlation peak of the OFC device, which translates into higher sensitivity to a temperature change.

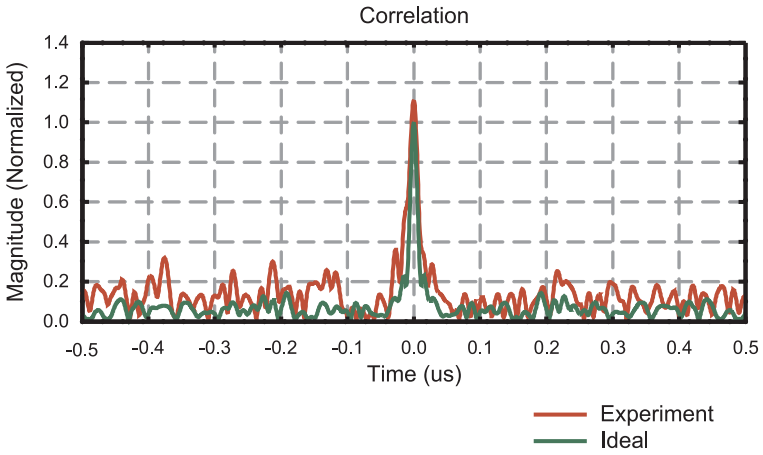

Figure 4.53: Comparison of an ideal NLR device (green) to correlation of experimental data and the ideal reflector response (red).

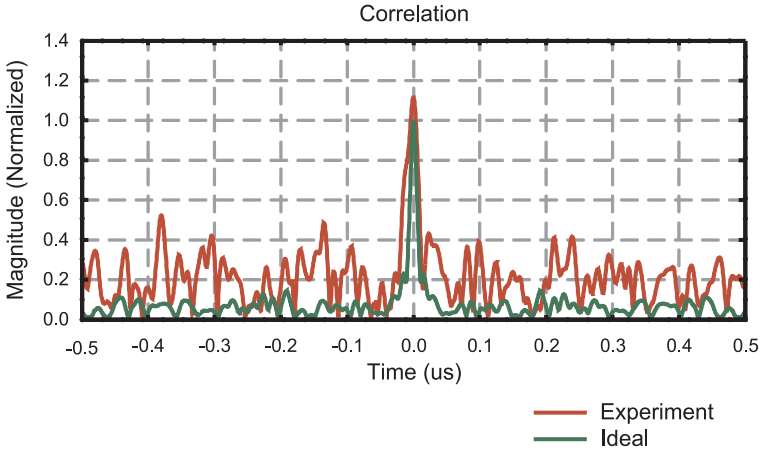

Figure 4.54: Comparison of auto-correlation of a single ideal NLR device response to correlation of ideal NLR device response and sum of 3 devices measured experimentally.

4.5 Summary

The purpose of this chapter was to present research into new and novel SAW noise-like-reflector (NLR) structures. This chapter presents some of the first embodiments that have been studied and tries to establish a framework for defining the structures implemented. It was shown that NLR-based approach is a successful alternative for wide-band coding. SAW reflector embodiments were demonstrated that had random properties in their structural design. Experiments conducted showed that it is possible to design and build structures with multiple stop-bands with near unity reflection. It has been demonstrated that the presented repeating structures can be used to de-spread the frequency response of NLR devices and introduced sharper pass- and -reject bands. Cell-based coding produces codes with excellent anti-collision properties. In case of the OFC chips, cross-correlation lobes in the proximity of the main auto-correlation lobe are generally very low resulting in a good dynamic range of the system. NLR chips along with chip scaling can produce even larger amount of codes in the system and are best suited for tag/RFID applications.

CHAPTER 5
DEVICE DESIGN: MULTI-TRACK DEVICES AND APODIZED REFLECTORS

The motivation for this work is to develop a device layout that reduces inter and cross deice chip collisions as well as provides flexible impedance matching characteristics. Multi-track CDMA tags have been previously studied, which helps to balance the tag reflectivity from chip-to-chip. Normally the IDT's beam extends over all tracks and the bandwidth is the same for all tracks, and there is no significant advantage over a single-track using this approach. Wideband tags using orthogonal frequency coding (OFC) can use multi-frequency chips subdivided into multi-tracks with low loss operation [5]. Each track has one or more chips, with each chip having a different chip frequency. The track-transducer is then designed to operate only over the required frequency bands; making each non-interacting track low loss. The overall transducer embodiment is now tailored for optimum performance for loss, coding and chip reflectivity. If all tracks are electrically in parallel, the overall transducer Q remains the same as a short wideband IDT, but the electrical reflection coefficient is

chosen for minimum loss or matching [42]. Several parallel track OFC S_{11} responses are measured where the reflection coefficient is nearly optimized for minimum unmatched insertion loss. In comparison, for a short wideband transducer of equivalent bandwidth, the reflection coefficient is close to unity with large unmatched loss.

5.1 Multi-track, Multi-transducer OFC SAW Devices

SAW OFC embodiments using multi-frequency Bragg reflectors increase design flexibility over CDMA single frequency Bragg reflector devices. Multi-track CDMA devices have been shown, and eliminate the pulse roll-off effect of a single in-line multi-chip structure. However, the multi-tracks increase insertion loss due to power division and recombining at the transducer. In comparison, OFC multi-track devices can be configured in many combinations with frequency selective tracks. The advantage is increased coupling and minimal inter-chip distortion. Since each track can be designed to couple energy at specific frequency bands, the inherent transducer insertion loss remains the same as a single track OFC device. The out-of-band parallel tracks simply add reactive loading, and the overall transducer Q is independent of embodiment, ignoring parasitic effects. Multiple tracks add further design flexibility for impedance matching and minimization of second order effects. There are many

possible transducer embodiments. A number of different types have been studied and proposed during these investigations and a few examples will be discussed.

5.1.1 Chip Collisions and Transducer Embodiments

A typical OFC tag has a wide band transducer with low number of electrodes. For any given bandwidth (including the total bandwidth of multi-track device) electrical Q is constant. A constant Q-arc is shown on the Smith chart given in Figure 5.1.a. One can move on that circle by adjusting the aperture of the transducer. In reality, apertures should be between 20 and 150 wavelengths long to avoid second order effects. This limits wide band transducer's possible impedance to the orange line segment Figure 5.1.d. In the case of a multi-track device, transducers can be electrically connected, mix and matching parallel and serial topologies. By picking the correct topology, it is possible to move along most of the Q-arc in the capacitive region of the Smith chart. For instance, for a 6-chip 60MHz device in order to -1 reflection coefficient (most left point on Smith chart) all parallel connections can be used as shown by the red line segment Figure 5.1.b.

Separating chips into multiple tracks can help to reduce chip collisions. An effective way to separate different chips is to ensure that any one track does not contain

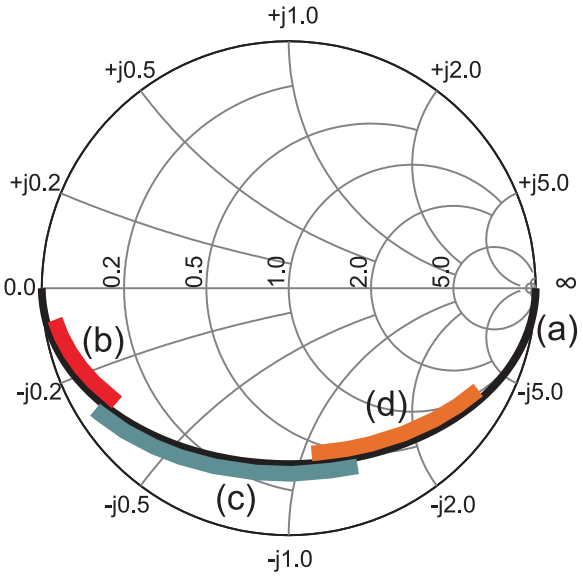

Figure 5.1: Reflection coefficient: examples of a constant Q arc (a) for: (b) all electrically parallel transducers, (b) three pairs of parallel connected transducers in series, and (d) all transducers electrically in series or a single wide band transducer is used.

two chips with adjacent OFC frequencies. Examples are shown in Figure 5.2 a, c, d, and e. Tracks can be connected electrically in parallel or in series. In-line transducers (i.e. transducers of the same track) can also be connected in parallel or in series to modify the impedance.

5.1.2 Transducer Impedance and Q

The transducer Q is a function of material coupling coefficient, parasitics, and required bandwidth given as

$$Q_{Transducer} < \frac{2 \cdot \%BW}{\pi k^2}. \tag{5.1}$$

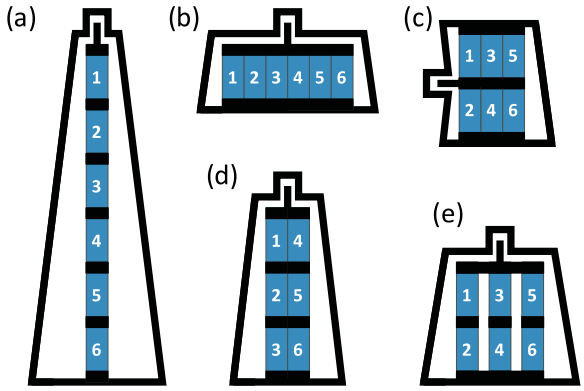

Figure 5.2: Examples of some of the possible transducer configurations for a 6-chip device: (a) all transducers electrically in series, (b) all in parallel in a single track, (c) all in parallel in two tracks, (d) three pairs of parallel connected transducers in series, and (e) three pairs of in series-connected transducers in parallel.

where the fractional bandwidth, $\%BW = N_{eff}^{-1}$. To first order the transducer Q is constant, independent of the embodiment. However, the transducer impedance (or admittance) elements are functions of the beam width and embodiment, and can be modified for optimum impedance. Possible embodiments include a simple IDT, a phase weighted IDT, in-line dispersive, parallel track OFC, and various combinations. Using these simple design principles provides a good first order design, but only works for non-reflecting transducers and provides a starting point for detailed analysis.

5.1.3 Performance evaluation

In order to evaluate and synthesize the multi-track transducer, the SAW COM model equations described in Chapter 3 are used. The transducer under test is put at a given distance from an ideal edge as shown in Figure 5.3. An ideal edge is a perfect reflector with no reflection loss and zero length.

This device is represented in a signal flow graph as shown in Figure 5.4. The solution is found using Mason's gain formula as [9]

$$G = P_{33a} + P_{13a} P_{12b} (-1) P_{21b} P_{31a}. \tag{5.2}$$

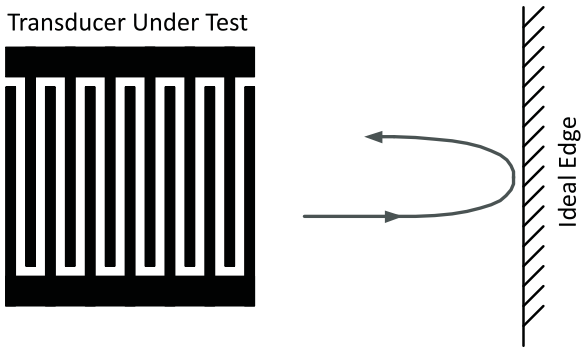

Figure 5.3: Transducer performance evaluation during initial tuning stages using ideal edge.

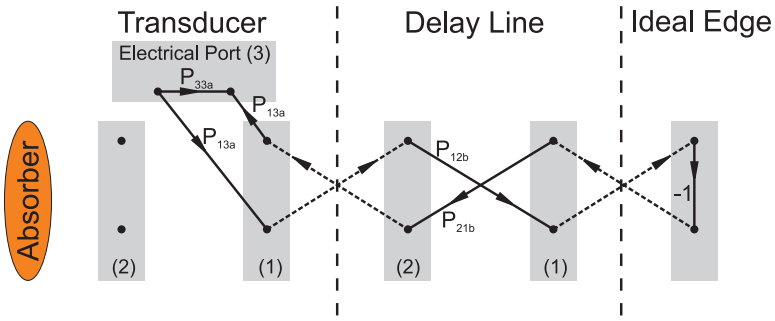

Figure 5.4: Signal flow graph of transducer performance evaluation during initial tuning using ideal edge.

Reflection of the edge can be gated in time and plotted in the frequency domain as shown in Figure 5.5.b. The Smith chart (Figure 5.5.a) is used as a predictor the device impedance. However, in order to make chips uniform in amplitude, the apertures of individual transducers are adjusted using the frequency response plot.

5.1.4 COM Model and Signal Flow Graph Analysis

The more exact coupling of modes (COM) model was used to simulate the devices. It has been shown that there is good correlation between the first order model, COM

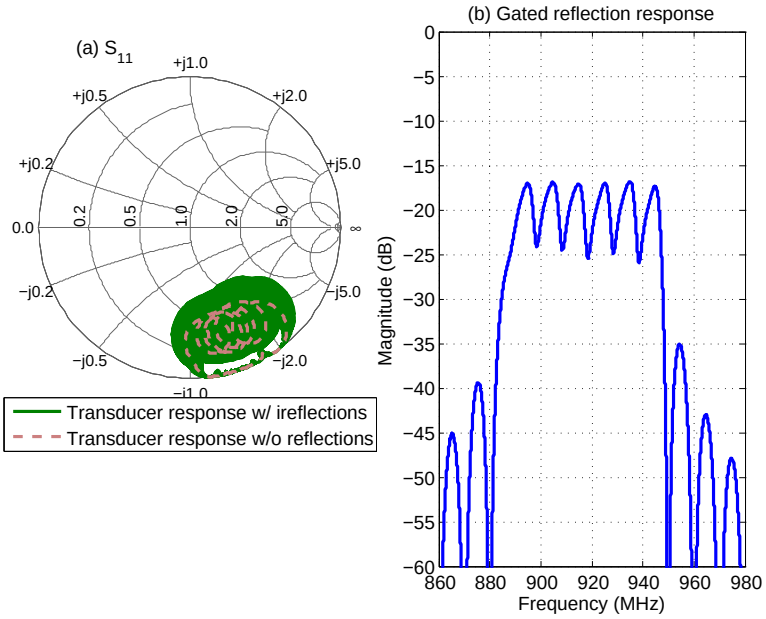

Figure 5.5: Transducer performance evaluation during simulation using an ideal edge and the signal flow analysis approach of Figure 5.4.

model, and experimental data for the structures designed and built for this chapter [7, 53, 8]. The simplified COM model predicts all higher order effects and multiple reflections.

Single track devices use the simple COM model. For multi-track or non-uniform track structures, signal flow graph theory was used in conjunction with the COM model to provide a completely flexible analysis and arbitrary electrical connections [9]. The three essential SAW components are represented as 2- or 3-port devices as shown in Figure 5.6.

Additionally propagation loss constants in equation 5.3 were changed from the values given by Morgan as shown in Table 5.1 to Morgan2007.

$$Loss = \alpha_1 f^{\alpha_2} + \alpha_3 f^{\alpha_4}, \tag{5.3}$$

where $Loss$ is loss in $dB/\mu s$, f is frequency in GHz and α_1 through α_4 are attenuation constants.

The COM material parameters have been previously extracted and used in the analysis. Bulk wave and propagation losses were empirically derived from experimental measurements and follow the general form given in Morgan, but with modified

Table 5.1: SAW Propagation Attenuation Constants

Constant	Morgan	Experimental Values
α_1	0.19	0.24
α_2	1.0	1.0
α_3	0.88	1.1
α_4	1.9	1.9

coefficients given in Table I [41]. Also an additional loss term was added for waves traveling underneath gratings and transducers of approximately 4.5 dB/μs.

5.2 Apodized Reflector Gratings

5.2.1 Apodization Profiles

The enabling technology behind OFC devices is that at each of the chips center frequency all other chips have nulls (i.e. are nearly transparent). However, there

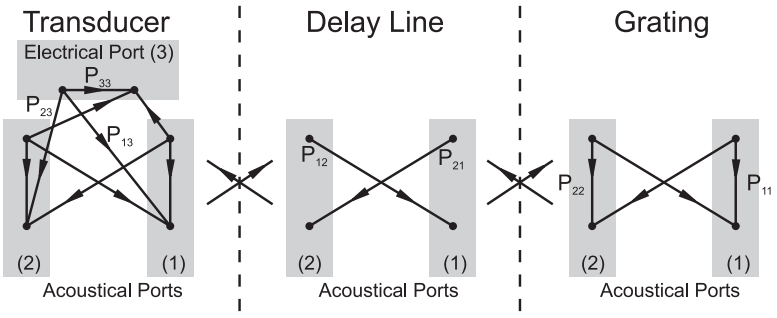

Figure 5.6: Signal flow graph representation of transducer, delay line and reflector.

is interaction between the chips within their bandwidth as highlighted in red for adjacent chips and in green for one over adjacent chips in Figure 5.7.

One of the ways to reduce this interaction is to apply a window function to a uniform reflector. A wide range of window functions is available with very side-lobes; however, typically, window functions with lowest side lobes have the longest time response length for the same bandwidth. Side-lobe attenuation has to be balanced against time response length. Truncated Sinc and Hamming window functions are good compromise of time length and side lobe levels. Shown in Figure 5.8 are ratios of cross-correlations of chip one to chips two through six to auto-correlation of chip

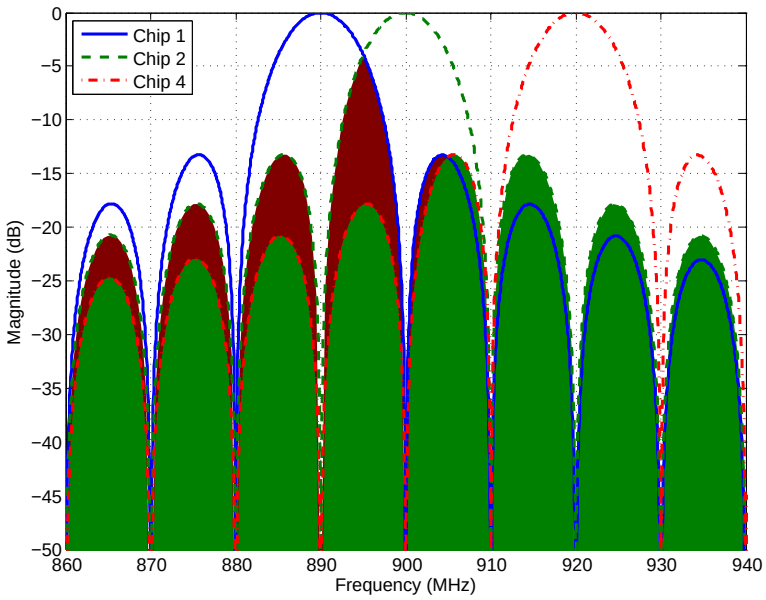

Figure 5.7: Overlap of frequency responses of adjacent and one over adjacent chips highlighted in red and green respectively.

one for following apodization window functions: uniform (blue), Hamming (green), and Sinc (red).

The Hamming window function has been chosen to be used with the devices for work presented in this chapter. Highlighted in Figure 5.9 in red is overlap of chips with adjacent OFC frequencies and in green - next adjacent OFC frequency, such as f1 to f3. Overlap in frequency is noticeably better for adjacent frequencies and dramatically better for the one over adjacent case.

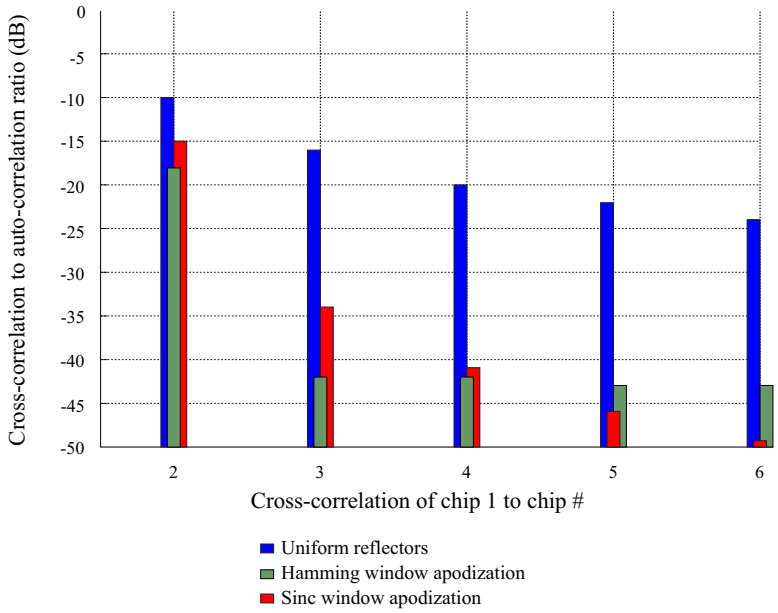

Figure 5.8: Ratios of cross-correlations of chip one to chips two through six to auto–correlation of chip one for following apodization window functions: uniform (blue), Hamming (green), and Sinc (red)

In a multi-sensor/-tag environment it is possible that a particular chip of a particular device will occupy the same time slot as one or more chips of other frequencies of one or more other devices. In order to reduce code collisions, cross-correlation of chips needs to be minimal. Cross-correlations for uniform and Hamming window function ideal chips are shown in Figure 5.10 and Figure 5.11 respectively.

Using COM model simulation, it has been found that the reflector grating with a specific window function can be built using following steps: apply window function to the grating, shift first half of the grating all the way down to the lower bus bar, and shift second half of the electrodes to the upper bus bar. Additionally, metalized

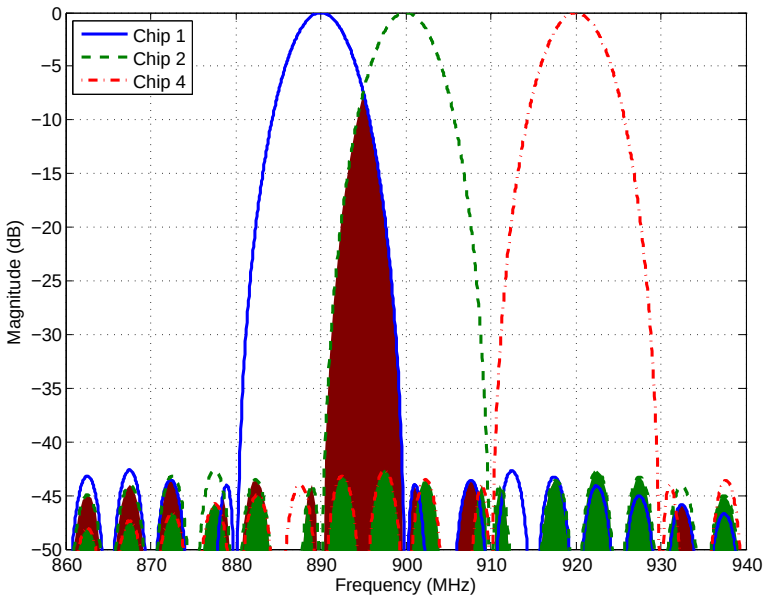

Figure 5.9: Overlap of frequency responses of adjacent and one over adjacent Hamming window chips highlighted in red and green respectively.

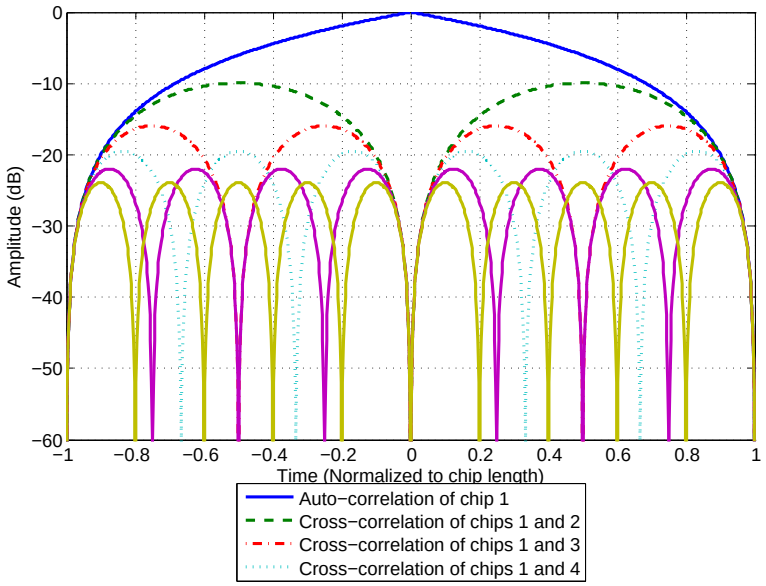

Figure 5.10: Auto-correlation of chip 1 and cross-correlations of chip one to other chips.

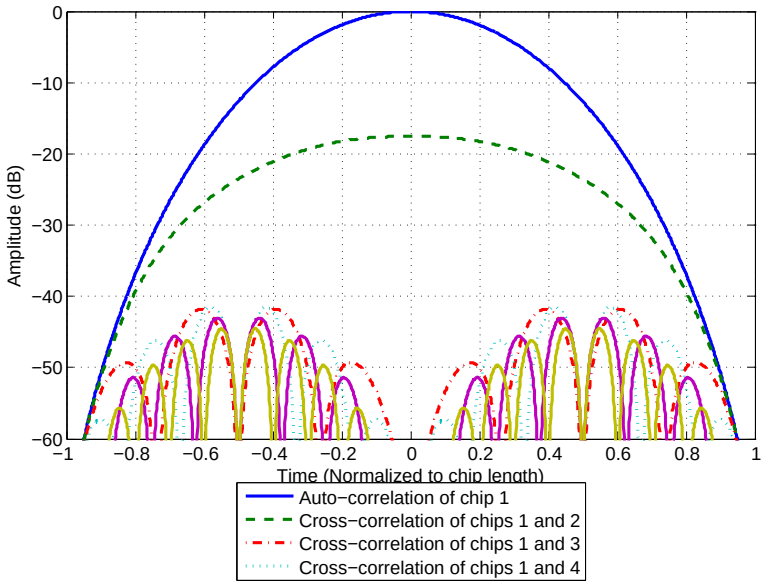

Figure 5.11: Auto-correlation of chip 1 with Hamming window and cross-correlations of chip 1 to other chips.

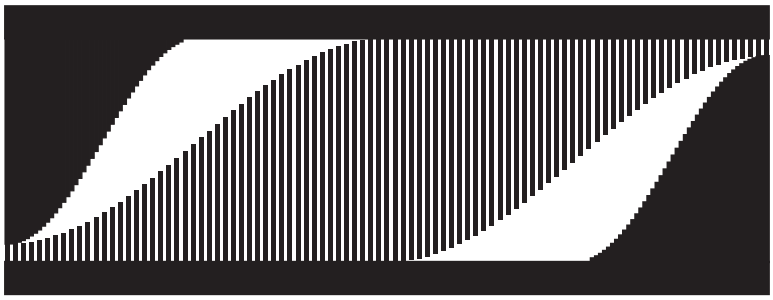

Figure 5.12: Reflector grating with Hamming window function apodization.

regions were added to remove any effects related to the difference in velocities in free and in metalized surfaces. Sample reflector grating with Hamming window apodization is shown in Figure 5.12.

Figure 5.13 shows a comparison of an auto-correlation of a six-chip device with uniform reflectors (blue) to an auto-correlation of a six-chip device with Hamming window reflectors (green). Two side lobes of Hamming-based device located half a chip away from main auto-correlation lobe are approximately 5dB higher than the side lobes of the typical OFC tag; however, majority of the lobes of the Hamming-based device are significantly lower.

5.2.2 Experimental Data of Apodized Reflector

A single chip device has been fabricated on Y,Z $LiNbO_3$ around 890MHz with 10MHz bandwidth, transducer operating at third harmonic and reflector grating operating

at second harmonic. Impulse response model, COM model and experimental data has then been compared in Figure 5.14. A good agreement between the models and the measured response has been shown, with side-lobes levels of approximately 40dB below the main response. Experimental data has shown one side-lobe (higher in frequency than the main response) that is higher in magnitude than predicted. This kind of non-symmetry is most likely due to the fact that there is still a phase difference between the sub-tracks.

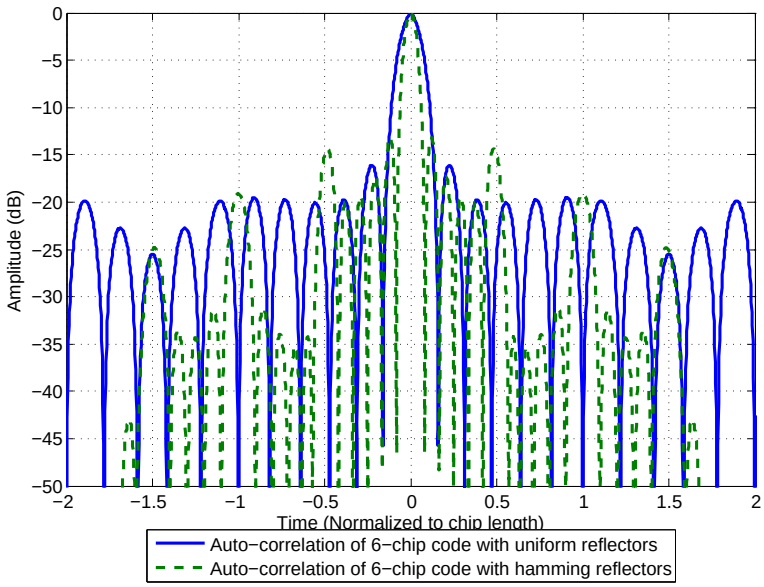

Figure 5.13: Comparison of auto-correlation of a 6-chip device (blue) to an auto-correlation of 6-chip device with Hamming apodized reflectors (green).

5.3 Devices

5.3.1 Layout Considerations

Longest and shortest paths traveled by waves of each of the transducer-reflector pairs is give in equations 5.4 and 5.5 as shown in Figure 5.15:

$$D_{Longest} = 2\left(L_{TX} + L + L_{GT}\right), \tag{5.4}$$

and

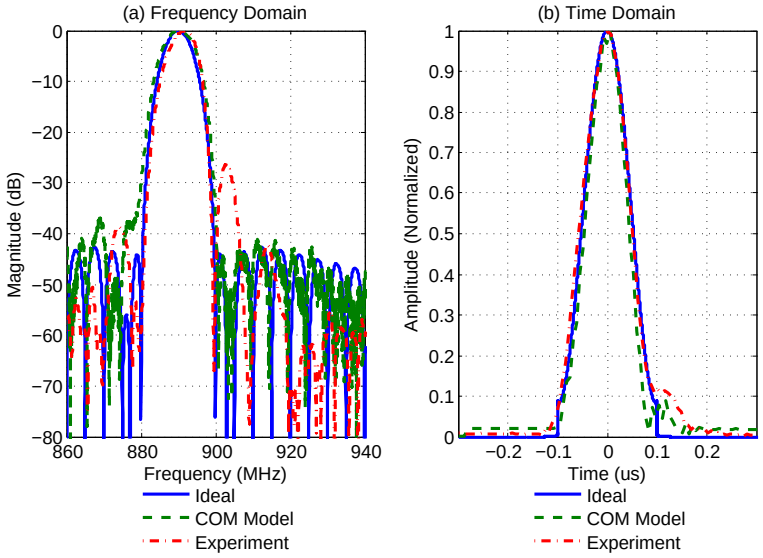

Figure 5.14: Comparison of an ideal (blue), COM (green), and experimental (red) single hamming window chip in (a) frequency and (b) time domains.

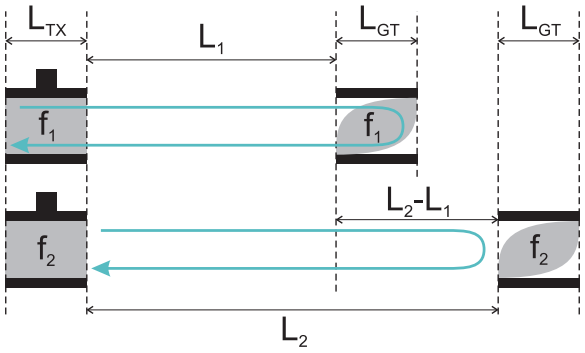

Figure 5.15: Illustration of reflector spacing considerations.

$$D_{Shortest} = 2L, \tag{5.5}$$

where L_{TX} is length of transducer, L_{GT} is length of reflector, and L is the distance measured from right edge of transducer to left edge of reflector.

In order for chips not to collide adjacently placed chips must satisfy

$$2L_2 \geq 2\left(L_{TX} + L_1 + L_{GT}\right). \tag{5.6}$$

For a smallest device foot print, L_1 and L_2 are expressed

$$L_2 - L_1 = L_{TX} + L_{GT}. \tag{5.7}$$

A cell based coding technique has been developed in Chapter 4. [36]. This technique requires that each chip to be assigned to a specific time slot with number of time slots equal to number of codes desired. Length of the entire reflector bank can then be represented by

$$L_{GTArray} = N_{Codes} \left(L_{TX} + L_{GT} \right). \tag{5.8}$$

If triple-transit is an issue, physical slots for the reflectors must start at a distance equal to the length of all allocated reflector slots, doubling the length of the device. Additionally, the input transducer also has to be factored in, its length must be multiplied by the number of in-line transducers (number of transducers per track). Finally, the full device length is given as

$$L_{Device} = 2N_{Codes} \left(L_{TX} + L_{GT} \right) + N_{InlineTX} L_{TX}, \tag{5.9}$$

where $N_{InlineTX}$ is number of transducers per track.

As an example, for a 60MHz-bandwidth device with six chips, six uniform transducers and hamming apodized reflectors on Y,Z $LiNbO_3$ $TX = L_{GT} \approx 381 \mu m$. For an 8-code set and two transducers per track total length of the device is approximately $1.2 cm$.

5.3.2 Experimental SAW Tag Device

A layout with 3 tracks connected in series and transducers within the tracks connected in parallel has been chosen as shown in Figure 5.16. The device was built on Y,Z $LiNbO_3$ at 915MHz and total bandwidth of 60MHz. Transducers were built with eighth wavelength electrodes to operate at third harmonic, and Hamming window apodized reflectors were designed to operate at second harmonic. Detailed design information is shown in Table 5.2.

Table 5.2: Experimental Device Parameters

Chip	**Transducer**		**Reflector**		**Aperture**	**Distance***
#	λ (μm)	N_p	λ (μm)	N_p	(μm)	(μm)
1	11.582	30	7.734	45	154.12	7976
2	11.430	30	7.671	45	123.29	11960
3	11.328	31	7.582	46	112.51	9017
4	11.201	31	7.493	46	154.12	12980
5	11.074	31	7.417	47	123.29	5969
6	10.947	32	7.341	47	112.51	6985

*Distance measured from right edge of transducer to left edge of reflector

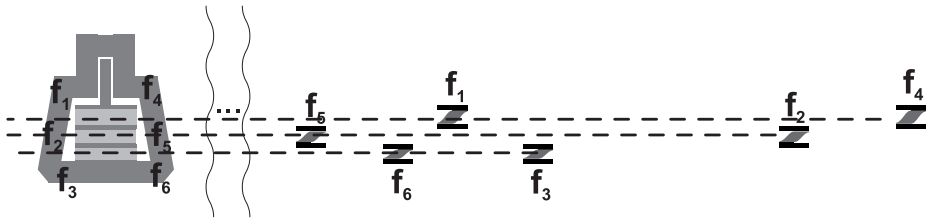

Figure 5.16: Experimental device: three tracks connected in series with two transducers per track connected in parallel.

5.4 Experimental Results of SAW Tag Device

Parasitics were added in the COM model with experimental data. Both Smith chart Figure 5.17 and time domain plots Figure 5.18 of COM and experimental data show good agreement.

Shown in Figure 5.19 are individual gated in time chips and plotted back to frequency domain. Chips 2 and 3 are the most attenuated because they travel under one transducer and one reflector. This additional propagation loss has not been included with the COM model this time. Other chips have either direct path or just one off-frequency element in the path of propagating wave. Note that for chips 1, 4, 5 and 6 side-lobe levels are 25-35 dB below the main response, which is a significant improvement over uniform reflectors that have side-lobe levels 15-20 dB below the main response.

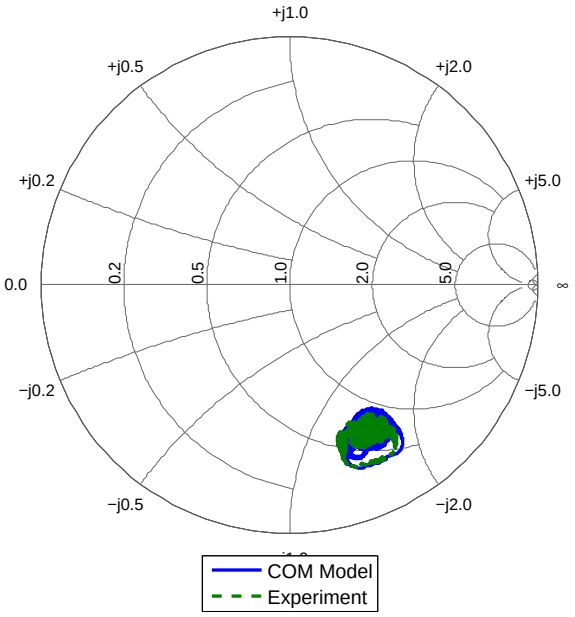

Figure 5.17: Smith chart of COM model simulation of reflection coefficient (solid blue line) compared to the measured reflection coefficient (dashed green line).

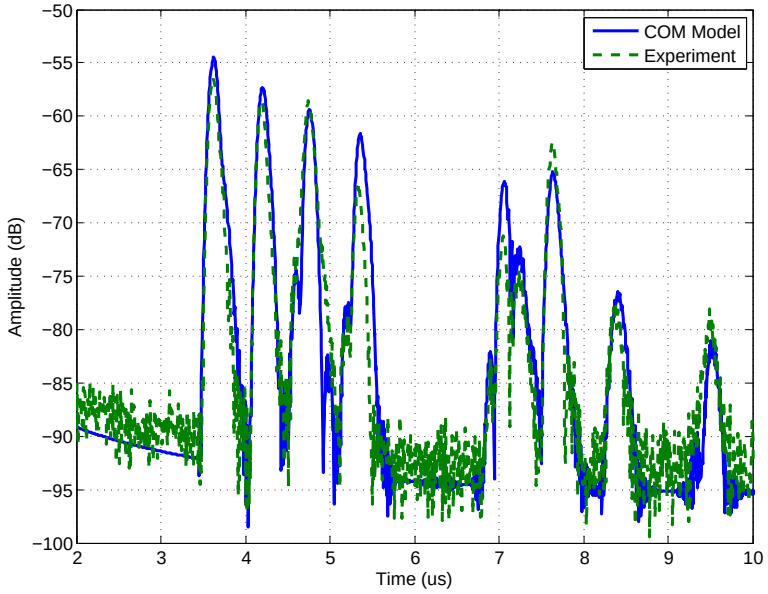

Figure 5.18: Time domain of COM model simulation (blue) compared to experimental data.

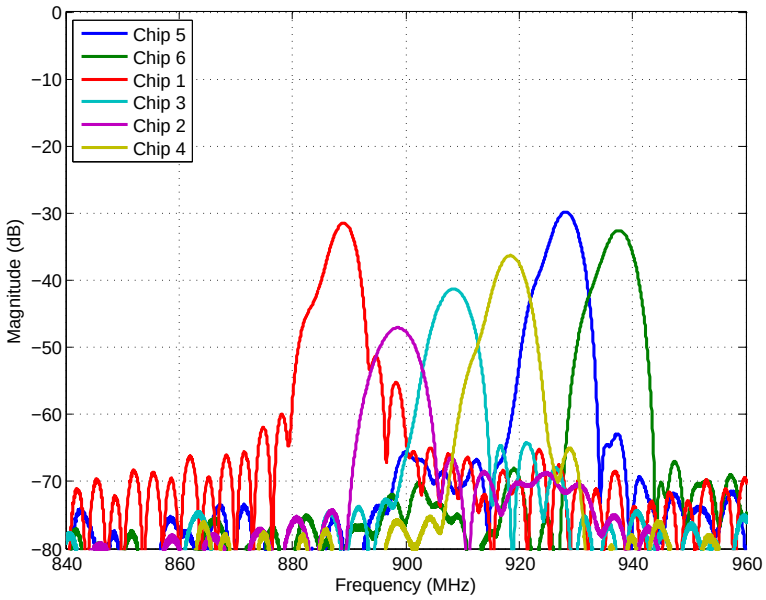

Figure 5.19: Individual chips gated out and plotted in frequency domain. In the upper left corner of the plot, legend has chips listed in the order in which they appear in time domain appear in time.

5.5 Experimental Multi-track Transducer-only Devices with Various Embodiments

Several device embodiments, shown in Figure 5.20.i, have been modeled using COM analysis as described in Chapter 3. Devices were modeled at several different center frequencies (250MHz, 500MHz, and 915MHz) with 60MHz bandwidth and apertures ranging from 15 to 150 wavelengths. Impedance ranges for those possible configuration are shown in Figure 5.20.ii, Figure 5.21.i, and Figure 5.21.ii for 915MHz, 250MHz, and 500MHz respectively.

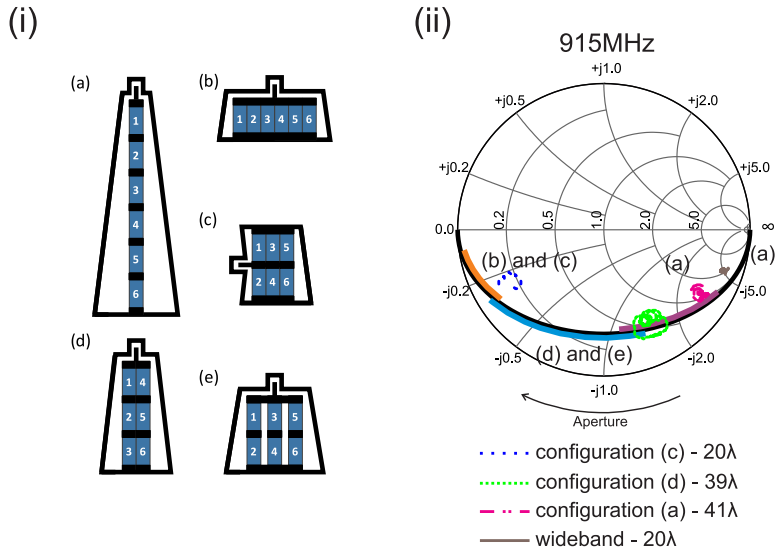

Figure 5.20: Various transducer configurations (i) and impedance ranges of their implementation with 15λ to 150λ, 915MHz center frequency and 60MHz bandwidth and select device responses (ii)

A sample set of transducer-only devices has been fabricated for various embodiments and aperture sizes and compared against predicted ranges and also plotted in Figure 5.20.ii and Figure 5.21. The purpose is to illustrate the impedance shifts due to different parallel series track embodiments. The constant Q regions are very useful for optimization of transducer and antenna matching for device integration. Experimental data has fallen well within the predicted ranges.

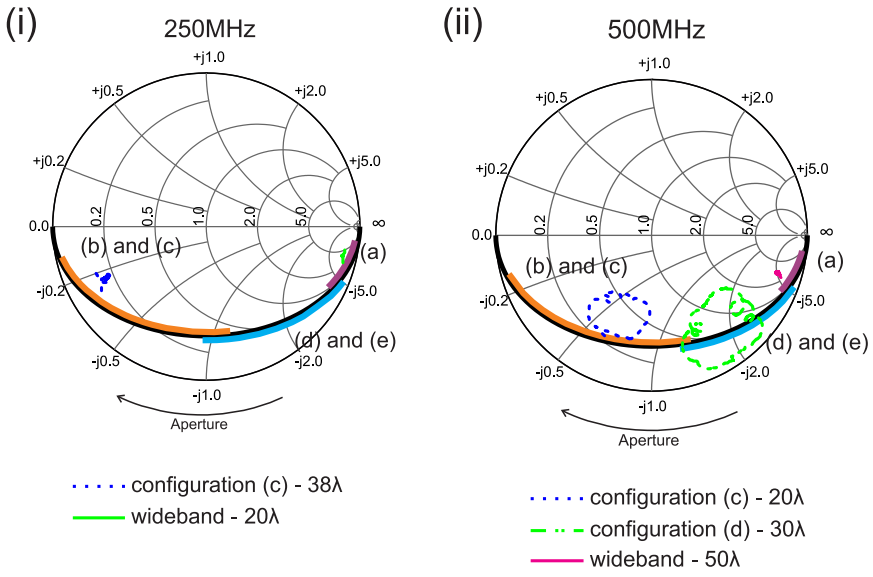

Figure 5.21: Input impedance ranges of various transducer configurations with 15λ to 150λ and 60MHz bandwidth and select device responses: (i) 250MHz and (ii) 500MHz center frequencies

5.6 Summary

The purpose of this chapter was to demonstrate a new and novel multi-track, multi-transducer OFC device design approach with reduced cross code collisions as well as lowered chip interactions within the devices for RFID and sensing applications. While Q for a specific bandwidth and specific substrate is fixed, the proposed multi-transducer approach allows flexibility of designing a device with reasonable aperture values almost anywhere on the constant Q-arc on the capacitive side of the Smith chart. It has been demonstrated that the flexible impedance design can provide optimal impedance matching which can reduce the size or completely eliminate the need for matching network. Due to nature of OFC chips, multiple transducer-reflector pairs can be combined within one track with minimal chip collisions without having to go to low reflectivity.

CHAPTER 6
SAW SENSOR CORRELATOR SYSTEM

Presented in this chapter is an interrogator for passive wireless SAW sensors. An RF burst interrogation technique was used for the system design. System implementation as well as its basic noise model are presented. Range analysis is performed and its relationship to noise is established. In addition, a simultaneous passive wireless operation of four 915 MHz OFC SAW sensors will be demonstrated.

6.1 System Overview

Several approaches have been suggested for realizing an interrogation system for passive wireless SAW sensors; a very simple approach to be discussed is the use of a pulsed RF-sinusoidal wave interrogation signal [21, 23, 24, 22]. Such system can be easily realized by either mixing up a DC pulse to a center frequency of the SAW sensors or by gating a continuous wave (CW). The system presented uses a gated CW interrogation signal, a synchronous transmitter and receiver, and a software

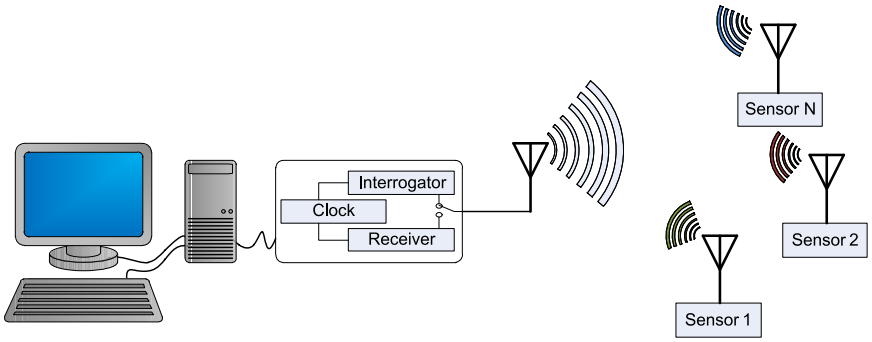

Figure 6.1: Block diagram of the 915 MHz correlator transceiver and sensor system.

radio based correlator receiver. Interrogator, receiver and ADC are controlled by the same reference clock to allow for coherent integration of multiple sweeps.

The block diagram of the 915 MHz OFC sensor system is shown in Figure 6.1. In its simplest form, the system is composed of multiple, passive, coded SAW sensors, a transceiver, and a post processing platform. The transceiver generates and transmits an RF burst that excites the sensors and also receives the reflected SAW signal, which is then mixed down to be digitized by an analog-to-digital converter (ADC) for post-processing in a computer. The system is composed of the following five modules: clock generator and phase locked loops (PLL), antenna duplexing switch, interrogator, receiver, and ADC/DSP module.

6.1.0.1 Clock generator and PLLs

A 10 MHz reference clock is used to control the ADC, digital circuit of the transmitter, and PPLs that generate a 915 MHz CW for interrogator. The same reference clock is also used to generate the 775 MHz local oscillator (LO) frequency to mix the received signal down to the 140 MHz intermediate frequency (IF) filter. The transmitter and receiver are synchronized by the master clock when coherent integration of multiple interrogation sweeps is needed to increase the signal-to-noise (SNR) ratio. A schematic representation of the transceiver module is shown in Figure 6.2.

6.1.0.2 Duplexing Antenna RF Switch

A Yagi antenna is shared by interrogator and receiver, via an RF duplex switch, and has 9 dB of gain and 50Ω impedance. RF switch provides 60 dB of isolation between interrogator and receiver parts of the system.

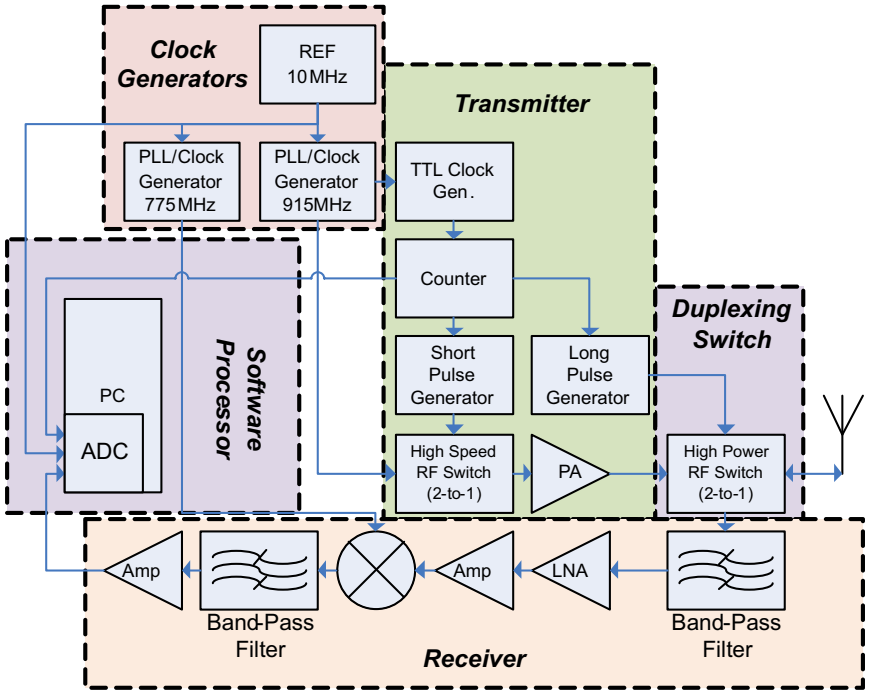

Figure 6.2: Block diagram of the 915 MHz system. There are 5 modules shown which are seperable from an analysis viewpoint: the RF clock and LOs, the duplexer and antenna, the RF transmitter, the RF receiver, and the ADC and digital post processor.

6.1.0.3 Interrogator

The interrogation burst is a gated 915 MHz, 10 ns sine wave with peak output power of 30 dBm into a 50 Ω load, with the total energy in the pulse of approximately 1 nJ. The interrogator controls the duplexing antenna RF switch for timing of transmit or receive mode.

6.1.0.4 Receiver

The receiver bandwidth is 95 MHz, the maximum gain is 47 dB, and the 1 dB compression point is 23 dBm. The received signal is mixed from 915 MHz down to a 140 MHz IF using a 775 MHz synchronized CW signal. The RF bandwidth of the ADC card is 300 MHz with a sampling rate of 2 Gsps. The ADC resolution is 8 bits and input voltage range is selectable from 400 mV to 8 V, and can be adjusted dependent on the level of the received signal.

6.1.0.5 ADC and DSP

Signal processing and sensor data extraction (for these sensors, temperature is the measured parameter) is performed within a standard computer platform using a software radio method developed with MATLAB®code. An adaptive filter is used for obtaining the matched filter response of each sensor as a function of temperature [36]. A single sensor can be interrogated up to 12 times per minute, and the current acquisition rate is limited by the post processing speed. The acquisition rate can be significantly increased with C coding and GPU utilization.

Since the SAW sensors are passive components, the tags will normally have a substantial amount of loss. Additionally, often gain of the antenna is compromised for its size, resulting in even higher loss of the returned signal, which can quickly result in the signal below the noise level. One technique to bring the signal out of the noise and improve SNR is to average multiple interrogation sweeps. If the reflected signal does not change and the noise is random, noise power will reduce by a factor of N, where N is the number of the averaged interrogation cycles. Phase lock between CW and the pulse is required for coherent integration. For example, when 100 sweeps are averaged, noise power is reduced by a factor of ten and the

range of operation is doubled [56]. Although the current receiver is synchronized, this chapter will only discuss results for single pulse mode operation.

6.2 SAW Temperature Sensor Parameters

A set of 4 sensors was designed using a time division approach [36]. OFC temperature sensors were built on Y,Z $LiNbO_3$ at 915 MHz center frequency. Each sensor has a unique OFC code with 5-chip reflector grating. Chips have time lengths of $\tau_{chip} = 54$ ns and are contiguous in time. The single chip bandwidth is $BW_{chip} = \tau_{chip}^{-1} = 18.5$ MHz with overall device bandwidth of $BW_{SAW} = 5 \cdot BW_{chip} = 93$ MHz. The SAW transducer is broadband, bidirectional, and has an aperture of 377 μm. Minimum delay between IDT and reflector is 1μs and varies with the device. The target antenna was a folded dipole on an FR-14 PC board and had approximately 2 dB gain[57, 58]. There was no intermediate matching network between the antenna and the device. Antenna design has been optimized such that the impedance of the antenna is nearly conjugately matched to the impedance of the SAW sensor. Target loss is approximately 22-24 dB, based on SAW sensor and antenna network analyzer measurements, with loss variance due to parasitic electrical effects of packaging and

connections of the SAW sensor and antenna. Photograph of one of the sensors used in the system is shown in Figure 6.3.

6.3 Experimental Setup and Results

6.3.1 Range Experiments

The range of the system depends on many parameters, including output power, transceiver antenna gain, receiver gain, noise figure and thermal noise of the receiver, interrogation signal power and energy, sensor antenna gain, SAW sensor bidirectional and propagation loss, SAW/antenna reflection loss and mismatch loss, and signal path loss. The receiver's ADC minimum-detectable-signal (MDS) and internal noise

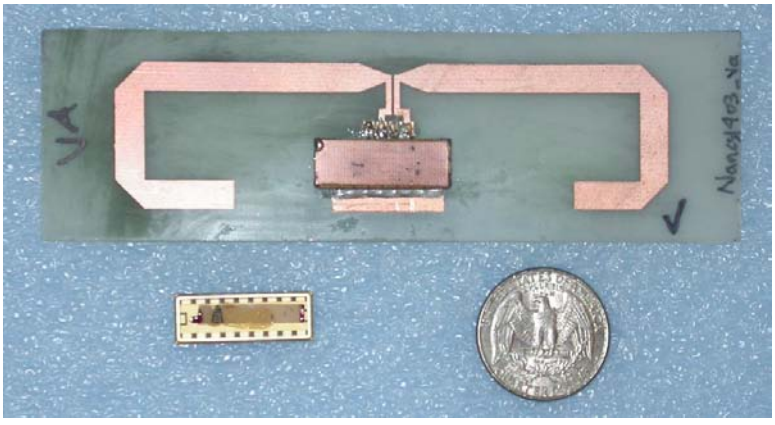

Figure 6.3: Packaged 915 MHz SAW OFC temperature sensor and antenna used on sensors.

are used as a measure of the predicted or expected range. Signal loss will occur at or near the ADC's MDS level, or if the signal to noise ratio (SNR) at the ADC becomes too small for detection. If the signal is above the MDS level but the S/N level is too low, coherent integration can be used and successful demodulation is still expected but this will not be discussed further. There are a number of noise sources which can degrade the signal integrity and can be divided into the following groups: internal noise of the receiver, inter-tag self-interference, and external signals that act as jammers. Post processing software simulates a correlator receiver for code demodulation and the device processing gain (PG) provides additional gain, but cannot be effectively utilized below the MDS level. If the noise floor is below the MDS level, then it is expected that the MDS level will be the approximate detection threshold, since the device PG cannot be used without a detectable signal.

For the following discussion, the MDS is defined as:

$$V_{MDS} = \Delta V = \frac{V_{Range}}{2^{N_{bits}}}, \tag{6.1}$$

where V_{MDS} is the minimum detectable signal, V_{Range} is ADC input voltage range and N_{bits} is resolution of the ADC in number of bits. In this case, MDS is the smallest voltage change in signal that can be detected in the worst case scenario. A

typical ADC is designed so that its internal noise is close to the value of the MDS, as defined in Equation 6.1 [59].

Data was taken to determine the receiver range and whether the MDS level is a good measure to predict the maximum range. Range experiments were conducted with a single device to eliminate inter-tag self-interference, and were performed in an open area where the external noise was at an acceptable level. The internal system noise is approximately 10 dB below the MDS level. For the system described, the receiver gain was 47 dB, the ADC input voltage range was 400mV, and the MDS level was 1.6mV (-42.9 dBm).

Figure 6.4 shows predicted and measured range versus input power at the ADC (left vertical axis) and extracted temperature error (right vertical axis). The reading error is defined as

$$Error = \frac{std\left(T_{out}\right)}{std_{max}}, \tag{6.2}$$

where the $std\left(T_{out}\right)$ is the standard deviation calculated based on 128 temperature readings, and the std_{max} is the standard deviation of the uniform distribution within the dynamic range of the system (maximum standard deviation of the output). For this experiment, 128 samples were recorded for each distance and power level. The

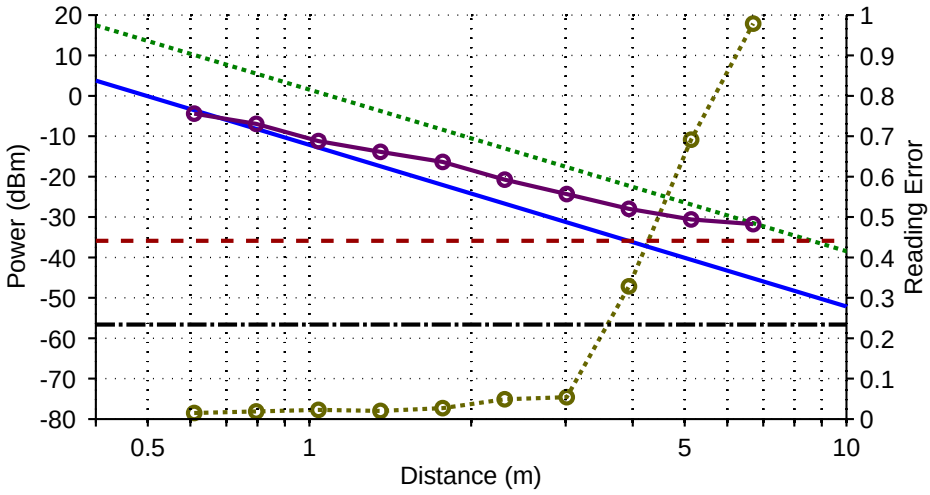

Figure 6.4: Comparison of predicted RMS power at the ADC (solid blue) and experimental data (solid purple line with circle data markers). Predicted reflected signal power at ADC with processing gain added (green dotted), system noise floor (red dashed), noise of the ADC card including quantization noise (black dash-dotted), and accuracy of the reading at corresponding distance (dark yellow dotted line with circle markers, right y-axis).

temperature dynamic range is 280°C (full scale). In the current implementation, the temperature extraction algorithm always returns a value within the dynamic range of the system. When the signal is stronger than any of the noise sources, the distribution of the extracted temperature values is approximately Gaussian. In the case when the signal to noise ratio is very small or the sensor is completely out of range, the extracted temperature will have an approximately uniform distribution within the dynamic range of the system. For example, for this system the dynamic temperature range is 280°C, which yields an 80.8°C standard deviation for uniformly distributed noise (std_{max}). Let's assume a 3 m distance, which yields a standard deviation of 5.5°C according to Figure 6.4. Based on equation 6.2, the error value is approximately 0.07. A cut-off error value of 0.07 was chosen based on the maximum value of the second derivative of the error curve, shown in Figure 6.4, which corresponds to the point where the rate of signal loss is greatest. In practical application, a cut-off error value would be determined based on the required accuracy.

From the predictions and measurements of Figure 6.4, it can be seen that the error increases dramatically as the measured signal level approaches the receiver noise level, as expected. The signal PG provides good detection accuracy, but its effect is lost as the signal approaches the receiver noise level.

6.3.2 Range Limits

As it has been mentioned in section 6.3.1, range in the presented system is limited by two key parameters: noise present in the system (both internal and external) and the minimum detectable by ADC signal, which is a function of both quantization and internal noise of the ADC.

Both thermal and external noise can be treated as one for range prediction purposes. Such noise can also be reduced by means of coherent integration as described in Section 6.1. In reality, successful signal detection at signal levels close to MDS would be limited by the internal ADC noise. In an ideal case, transition between detecting signal and loosing it would be sharp; however, in the real SAW system due to the fact that the chips are not uniform and roll off at high and low frequency is present, some of the chips will disappear sooner than others, which means that the signal will be lost gradually due to the MDS restrictions. Unlike with the regular noise, once the received signal falls completely below the MDS, coherent integration fails to bring the signal level up out of the noise [59].

A block diagram of a noise model of the presented system is shown in Figure 6.5. An attenuator was used to create conditions when the noise of the receiver and the

received signal is smaller than the ADC noise and the MDS. The received signal is given as

$$P^*_{SIG} = (P_{SIG} + P_{NSYS}) \cdot \beta + P_{NThrm} + P_{NADC}, \tag{6.3}$$

and

$$SNR^* = \frac{P^*_{SIG}}{P_{NSYS} \cdot \beta + P_{NADC} + P_{NThrm}} = SNR + 1, \tag{6.4}$$

where P^*_{SIG} is the signal power received at the ADC, P_{SIG} is the signal from the SAW sensor, P_{NSYS} is the internal noise of the receiver, P_{NThrm} is the thermal noise at the input to the ADC, P_{NADC} is the internal ADC noise (including the quantization noise), and β is attenuation value at the input to the ADC. The ADC noise has been calculated based on the specifications provided by the manufacturer. Noise of the receiver has been determined using spectrum analyzer measurements. Signal power has been determined based on oscillator measurements at a distance of 0.6 meters for 0 dB attenuation at ADC. It was assumed that the power decreases 40 dB per decade increment of the distance from the interrogator to the sensor.

Once the signal level is close to or below the noise level, it is only possible to estimate the signal power using the correlation peak value using the matched filter

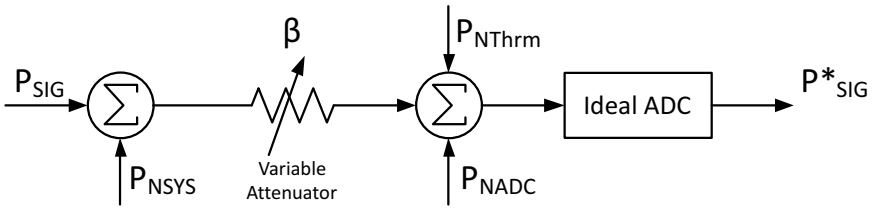

Figure 6.5: Block diagram of the noise model for system analysis. An additional variable attenuator, β, is added for test measurements.

technique. Since the adaptive matched filter approach is used, the algorithm will always produce a correlation peak, even if the sensor is out of range and the only signal acquired by the ADC is noise. It is impossible to measure true SNR when the signal level is low, so SNR* is used instead, as in Equation 6.3. Figure 6.6 illustrates SNR* for a system configured for -46 dBm MDS for multiple attenuation steps at the ADC. First three curves are nearly identical, which suggests that both signal and system noise are at the same level with respect to each other and the ADC noise is not making any impact. The last two curves are attenuated by 10 dB steps, indicate that the signal has decreased noticeably compared to the ADC noise, shown by the reduced range for SNR* approaching 0 dB.

Experimental data shown in Figure 6.7 agrees well with the model for SNR* values above 5 dB. Due to the fact that the signal strength is measured using the adaptive matched filter technique and also due to the fact that at low signal levels, quantization effects start to become significant, measured SNR* instead of converging

to 0 dB fan out up to ± 5 dB; however, as it will be demonstrated further, at these levels successful single sweep temperature extraction is not possible.

Shown in Figure 6.8 is SNR* and reading error from equation 6.2 versus distance versus attenuation values at the ADC. While the SNR* confirms the predictions of the noise model, error curves provide additional information about the noise effects on the reading. For a scenario when ADC noise is less than the receiver noise (three upper most SNR* curves of Figure 6.8), SNR* needs to be 10 dB or greater for the extracted temperature error to be less than 0.07. For SNR* values equal to or greater than 10 dB $SNR^* = SNR + 1 \approx SNR$. This experiment also shows that for this

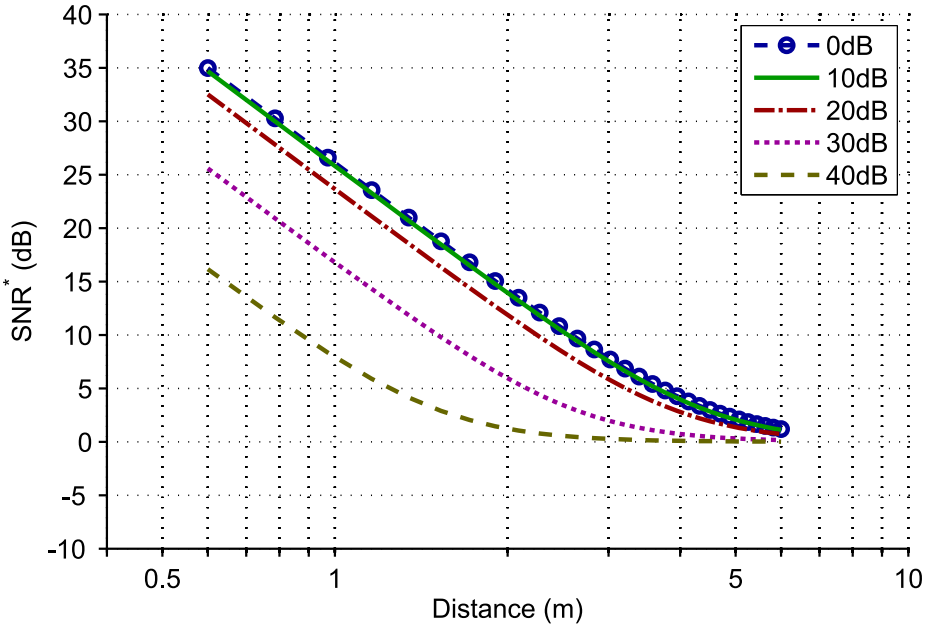

Figure 6.6: Model predictions for -46 dBm MDS: SNR* values for several attenuation steps at the ADC (0 dB to 40 dB) vs distance.

particular system, a gain of 27 dB would be sufficient to achieve maximum range provided that the receiver noise is proportional to the gain.

A typical ADC operation requires the input signal to be amplified to span the entire allowed ADC input voltage range to avoid effects associated with small input signal levels with respect to MDS. However, in the event that the needed amplification is not available, signal can still be extracted. For the bottom two SNR* curves of Figure 6.8, dominant noise is the ADC noise. For example, the SNR* curve corresponding to a 40dB attenuation at the ADC (most bottom SNR* curve) crosses

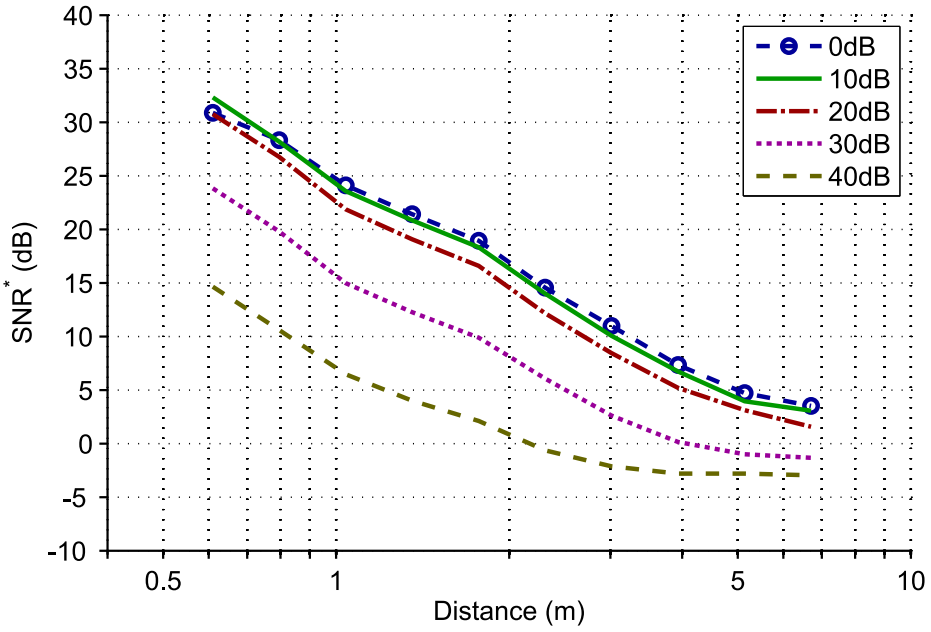

Figure 6.7: Range measurements for system configured for -46 dBm MDS: SNR* values for several attenuation steps at the ADC (0 dB to 40 dB) vs distance.

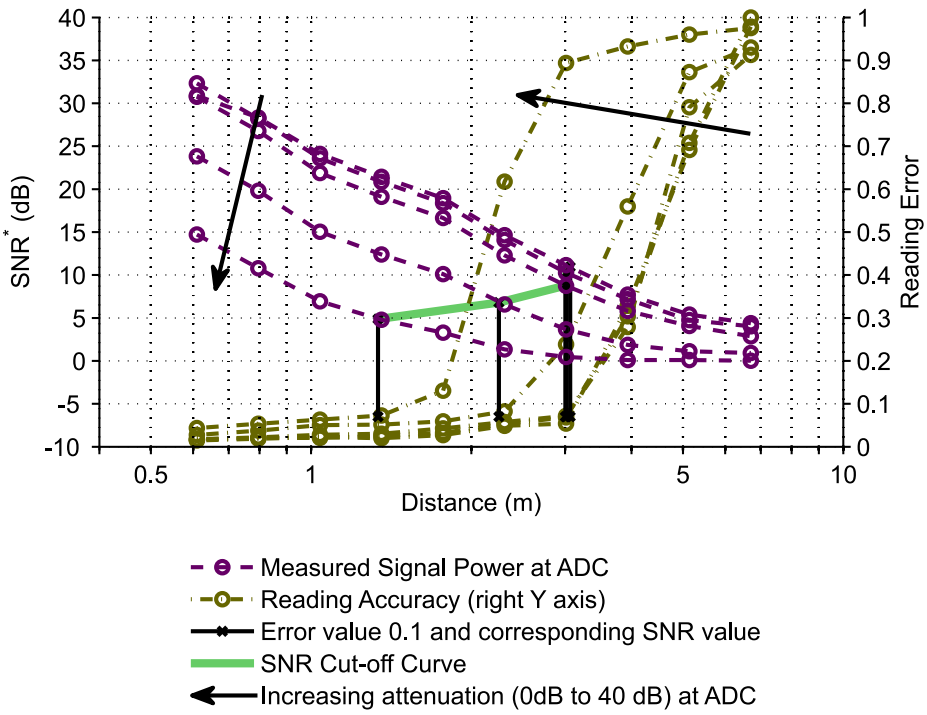

Figure 6.8: Range measurements for system configured for -46 dBm MDS: experimental SNR* data for multiple ADC attenuator values (dashed purple line with circle data markers) and reading error at corresponding distance (dark yellow dash dotted line with circle markers, right y-axis). Multiple data curves correspond to attenuator values (increments) at ADC increasing in the direction of arrow. Shown in thick solid green line is cut-off SNR*, lower SNR* values yield error 0.07 and higher.

the 4-dB mark when temperature error becomes more than 0.07. For SNR* values of 4 dB, SNR is approximately 1.5 dB, based on equation 6.4.

6.3.3 Multi-sensor Operation

As a demonstration of multi-sensor operation, the 915 MHz SAW OFC transceiver system with four OFC SAW sensors interrogated simultaneously is given, with results shown in Figure 6.9. The devices are located in close range to each other at a nominal distance of 0.8 to 1.2 meters, at this distance SNR* $\approx$ SNR $\approx$ 25 dB. Devices were cooled and heated using a refrigerant and heat gun, respectively, and were free running. Thermocouples (TC) were attached as close to the sensor devices as possible to achieve good thermal contact and electrical isolation, while minimizing interference to the antenna. Sensors NS402 and NS403 remained at room temperature; sensor NS401 was heated to 140°C and sensor NS403 was cooled to -130°C. Data was taken simultaneously from all four sensors, with a single "ping" and then temperature extracted in the correlator receiver software, with no post processing integration. The temperature was extracted using the adaptive filter approach. Power received from the sensors at the interrogator antenna is approximately 95 dB below power sent

to the antenna. The SAW sensors and thermocouple tracked to within ±3°C over nearly the entire range of temperature variation.

6.4 Summary

Single sensor operation has been demonstrated for up to 3 meters with 60% of extracted values within 3.5% range of the dynamic range of the system. A first order noise and signal strength model has been developed and showed good agreement when compared with measured results. With the first order range analysis it was determined that in order to successfully extract temperature an SNR of approximately 10 dB is required when noise received at the ADC is dominantly due to the receivers internal noise. SNR of 1.5 dB is sufficient when the internal ADC noise is greater than the noise of the receiver.

Multi-sensor passive wireless operation has also been demonstrated for four OFC SAW sensors located at approximately 1 meter away from the interrogator. A dynamic range of 280°C has been demonstrated with ±2.5% accuracy.

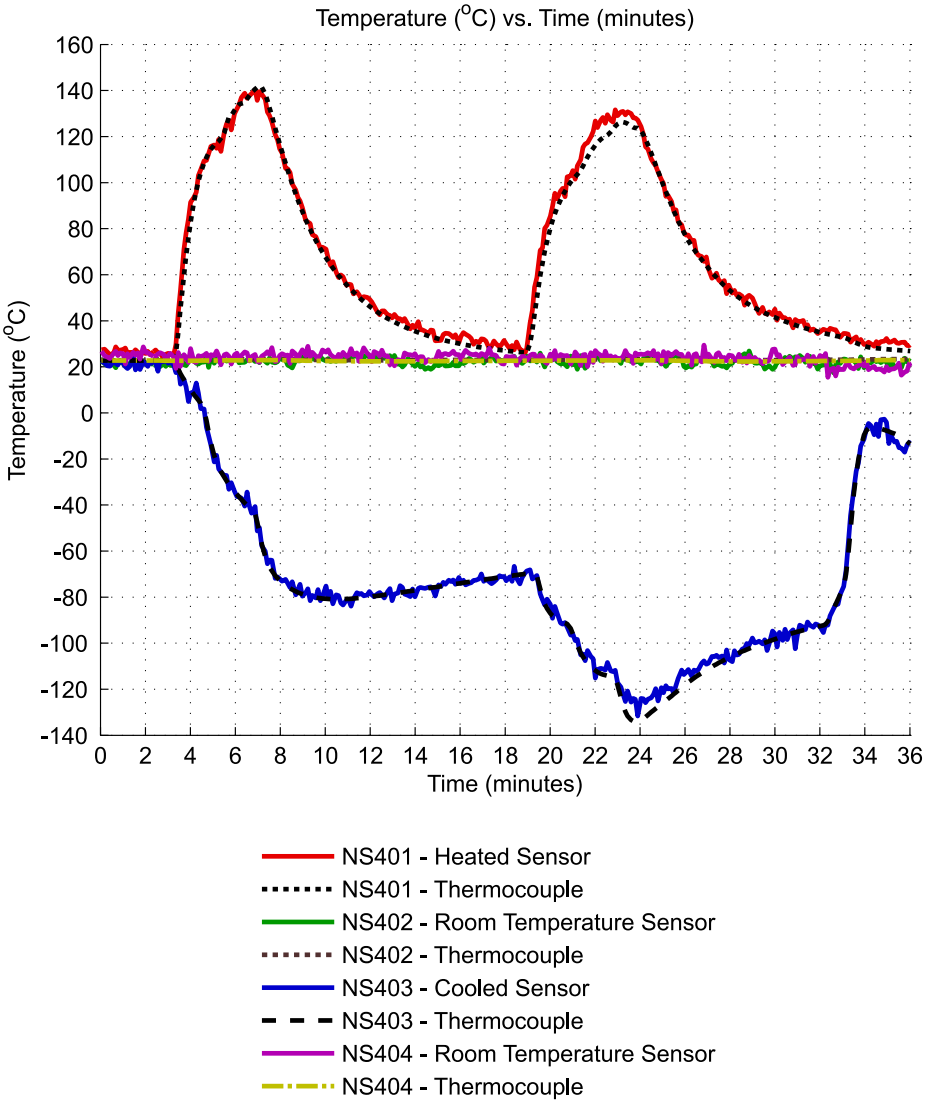

Figure 6.9: Results of the 915 MHz SAW OFC temperature sensor transceiver system. Four OFC SAW sensors are co-located in close range to each other at a distance of 0.8m to 1.2m; sensors NS402 and NS403 remained at room temperature, sensor NS401 heated to 140°C and sensor NS403 cooled to -130°C. Data was taken simultaneously from all four sensors and then temperature extracted in the correlator receiver software.

CHAPTER 7
CONCLUSION

As part of this dissertation, the first operational software correlator based transceiver for passive wireless OFC sensor system has been developed. An OFC TDM coding technique has been introduced for multiple sensors which are interrogated simultaneously with minimal code collisions. A unique multi-track, multi-transducer device configuration has been proposed that conjugately matches the SAW device to the antenna input impedance, and also spatially separates chips within the device further reducing inter-device code collisions.

In order to design and accurately simulate devices presented in this dissertation, the existing COM model analysis has been extended by using a signal-flow graph technique with elements expressed as hybrid P-matrices. This approach can be used to analyze diverse device configurations with unlimited number of ports and acoustically independent tracks. In current implementation, a new solution is computed for every track and P-matrix element. The computational complexity can be noticeably reduced by reusing previous solutions or parts of the solutions from one track to

another, since the track parameters are similar to each other; often have the same number and types of elements and their order. The model has also been expanded to analyze apodized reflectors that are separated into multiple tracks that contain only uniform portions of the reflectors. Reflectors with high number of electrodes result in high number of tracks. By rounding off the tracks and reducing the number of tracks to a fixed number with uniform width, accurate results can be obtained with as little as 25 tracks. The algorithm can be further improved by implementing grouped tracks when the two smallest tracks are merged together, until only 10-15 tracks remain. This enhancement should produce better and faster results. In addition to the COM model, a synthesis model has been created based on the hybrid P-matrices and signal-flow graphs. This model can be used to quickly and accurately design a multi-track, multi-transducer device. This model could be expanded to model the parasitic capacitance and resistance of the ground and signal pads as well as connections made between several transducers.

The cell-based (OFC with TDM) coding technique produces codes with excellent anti-collision properties. In case of the OFC chips, the cross-correlation lobes in the proximity of the main auto-correlation lobe are generally very low resulting in good dynamic range of the system. It was shown that the NLR structures can be a successful alternative for wide band coding and SAW reflector implementations were

demonstrated that had random properties in their structural design. Experiments conducted showed that it is possible to design and build structures with multiple stop-bands with near unity reflection. A system of devices with NLR chips instead of OFC chips was designed using cell-based coding. In future work, a relationship between systems dynamic range, spacial diversity, number of chips, devices and total bandwidth needs to be established. The drawback of the NLR-based approach is reduced dynamic range; it can, however, be successfully used in tag applications. The auto-correlation peak of NLR devices is narrower compared to OFC devices, which yields higher sensitivity. It is possible to use this approach on a substrate that is less sensitive to temperature change. The NLR-based approach has better security properties and on temperature compensated substrate can work well as an RFID tag or for sensors with small dynamic range (i.e. temperature sensors for homes). NLR codes are currently generated randomly until a good code set is found. The initial code is found using just "+1" and "-1", and then verified using the COM model. It was found that better codes can be achieved if each electrode-gap pair is modeled as a sequence "+1,-1", and the offset of an electrode-gap pair (to produce opposite phase) simply as "0". On the chip level, the NLR approach is similar to CDMA and perhaps, some of the device coding techniques available for CDMA should be used for generation of NLR chips. It has been shown that the bandwidth of the NLR chips

can be reduced using repetitions. However, long structures need to be examined for second order affects, which presented them selves as a ripple in the frequency domain response.

A new and novel multi-track, multi-transducer OFC device design approach has been demonstrated and showed reduced cross code collisions as well as lowered chip interactions within the devices for RFID and sensing applications. While Q is a function of device substrate and bandwidth, the described multi-transducer approach allows flexibility of designing a device impedance with reasonable aperture values (between 20 and 200 wavelengths) almost anywhere on the constant Q-arc on the capacitive side of the Smith chart. The flexible impedance design can provide optimal impedance matching; reducing the size or completely eliminating the need for a matching network. Due to the nature of OFC chips, multiple non-adjacent frequency transducer-reflector pairs can be combined within one track with minimal chip collisions for reflectors with even high reflectivity. Due to second order and parasitic effects, measured devices have typically 5-10 dB higher insertion loss than a typical wide-band single transducer device. In future research, this loss needs to be explained and modeled. An interesting sensor embodiment for future investigation has transducers electrically separate from each other and connected to their own narrow

band antennas, versus having to use a single wide band antenna that typically has lower gain.

It has been shown that the synthesis model is a good design and analysis tool. Possible impedance ranges have been calculated for 250MHz, 500MHz and 915MHz center frequencies, 60MHz bandwidth on Y,Z $LiNbO_3$ substrate. Three sets of devices at those frequencies have been built and measured and successfully compared against predicted impedance ranges. Apodization can extend the OFC approaches and reduce inter-chip collision and cross correlation energy. It also results in code collision reduction for multi-tags/-sensor systems. Multi-track, multi-transducer, OFC SAW sensors offer viable solution for multi-device applications.

The first operational passive wireless OFC SAW sensor RF burst interrogator has been demonstrated at 915MHz. A single sensor has been successfully interrogated at a distance of 3 meters. At 3-meter distance, 60% of the extracted values fell within a 10°C range of the actual temperature (measured with a thermocouple) which is 3.5% of the dynamic range of the system. A first order noise and signal strength model has been developed and showed to be in good agreement when compared with measured results. With the first order range analysis it was determined that a SNR of approximately 10 dB is required when noise is dominantly due to the receiver. An SNR of 1.5 dB is sufficient when the ADC noise source is dominant over

other sources. Multi-sensor passive wireless operation has also been demonstrated for four OFC SAW temperature sensors located at approximately 1 meter way from the interrogator. A dynamic range of 280°C has been demonstrated with ±2.5% accuracy. A future study needs to be performed for near field interaction of the sensors; the maximum range of operation decreased as the number of sensors in the system increased. One of the range limiting factors in the range experiment was the noise coming from the local interference such as cell phone towers, which resulted in noise higher than the internal noise of the system. A range measurement needs to be performed in a large anechoic chamber or in a field area with poor or no cell phone reception. Using an RF chirp instead of a short RF pulse can significantly increase the power of interrogation and therefore range. An RF chirp based system should be implemented as part of future work.

APPENDIX
PUBLICATIONS AND PATENTS

Kozlovski, N.Y.; Gallagher, D.R.; Malocha, D.C.; Hague, E., "Design of Mini-Modular Oscillators using RF and Microwave Design Techniques", *Frequency Control Symposium*, 2006

Malocha, D. C.; Gallagher, D. R.; Kozlovski, N. Y., "Ultra Wide Band Communication Systems Using Orthogonal Frequency Coded SAW Correlators", *Ultrasonics Symposium*, 2006

Kozlovski, N.Y.; Malocha, D.C.;, "SAW Phononic Reflector Structures," *Frequency Control Symposium, 2007 Joint with the 21st European Frequency and Time Forum. IEEE International* , vol., no., pp.1229-1234, May 29 2007-June 1 2007

Kozlovski, N.Y.; Malocha, D.C., "SAW noise-like coded reflector structures," *Frequency Control Symposium, 2008 IEEE International*, vol., no., pp.290-295, 19-21 May 2008

Malocha, D.C.; Pavlina, J.; Gallagher, D.; Kozlovski, N.; Fisher, B.; Saldanha, N.; Puccio, D., "Orthogonal frequency coded SAW sensors and RFID design principles," *Frequency Control Symposium, 2008 IEEE International*, vol., no., pp.278-283, 19-21 May 2008

Pavlina, J.M.; Santos, B.; Kozlovski, N.; Malocha, D.C., "SAW wireless, passive sensor spread spectrum platforms," *Ultrasonics Symposium, 2008. IUS 2008. IEEE*, vol., no., pp.1112-1115, 2-5 Nov. 2008

Malocha, D.; Kozlovski, N.; Santos, B.; Pavlina, J.; Belkerdid, M.A.; Mears, T.J., "Ultra wide band surface acoustic wave (SAW) RF ID tag and sensor," *Military Communications Conference, 2009. MILCOM 2009. IEEE*, vol., no., pp.1-7, 18-21 Oct. 2009

Pavlina, J.M.; Kozlovski, N.; Santos, B.; Malocha, D.C., "SAW RFID spread spectrum OFC and TDM technology," *RFID, 2009 IEEE International Conference on*, vol., no., pp.110-116, 27-28 April 2009

Wilson, W.C.; Malocha, D.C.; Kozlovski, N.; Gallagher, D.R.; Fisher, B.; Pavlina, J.; Saldanha, N.; Puccio, D.; Atkinson, G.M., "Orthogonal Frequency Coded SAW Sensors for Aerospace SHM Applications," *Sensors Journal*, IEEE , vol.9, no.11, pp.1546-1556, Nov. 2009

Kozlovski, N.Y.; Malocha, D.C., "SAW noise-like anti-collision code study," *Frequency Control Symposium, 2009 Joint with the 22nd European Frequency and Time forum. IEEE International*, vol., no., pp.616-621, 20-24 April 2009

Kozlovski, N.Y.; Malocha, D.C., "SAW passive wireless multi sensor system," *Ultrasonics Symposium (IUS), 2009 IEEE International*, vol., no., pp.1541-1544, 20-23 Sept. 2009

Kozlovski, N.Y.; Malocha, D.C., "Multi-track low-loss SAW tags with flexible impedance matching for passive wireless sensor applications," Frequency Control Symposium (FCS), *2010 IEEE International*, vol., no., pp.279-286, 1-4 June 2010

Kozlovski, N.Y.; Malocha, D.C., Weeks, A.R., "Wireless 915 MHz OFC SAW Multi-sensor Temperature System", *Sensors Journal*, 2011 (submitted)

Kozlovski, N.Y.; Malocha, D.C., Weeks, A.R., "A 915 MHz SAW Sensor Correlator System", *UFFC, Transactions on*, 2011 (submitted)

Patent

Malocha D, Kozlovski N, inventors; filed on Nov 13, 2009, "Surface Acoustic Wave Coding for Orthogonal Frequency Coded Devices." Application number 12/618,034, publication number US 2010/0117804 A1

LIST OF REFERENCES

[1] A. Abdollahi, Z. Jiang, and S. Arabshahi, "Evaluation on mass sensitivity of SAW sensors for different piezoelectric materials using finite-element analysis," *Ultrasonics, Ferroelectrics and Frequency Control, IEEE Transactions on*, vol. 54, no. 12, pp. 2446 –2455, 2007.

[2] M.-I. Rocha-Gaso, R. Ferna andndez Di andaz, A. Arnau-Vives, and C. March-Iborra, "Mass sensitivity evaluation of a love wave sensor using the 3d finite element method," in *Frequency Control Symposium (FCS), 2010 IEEE International*, june 2010, pp. 228 –231.

[3] B. Fisher and D. Malocha, "Study of the acoustoelectric effect for saw sensors," *Ultrasonics, Ferroelectrics and Frequency Control, IEEE Transactions on*, vol. 57, no. 3, pp. 698 –706, 2010.

[4] F. Seifert, W.-E. Bulst, and C. Ruppel, "Mechanical sensors based on surface acoustic waves," *Sensors and Actuators A: Physical*, vol. 44, no. 3, pp. 231 – 239, 1994.

[5] D. Malocha, D. Puccio, and D. Gallagher, "Orthogonal frequency coding for SAW device applications," in *Proc. IEEE Ultrasonics Symposium*, vol. 2, Montreal, Que., Canada, Aug. 2004, pp. 1082–1085.

[6] D. P. Morgan, *Surface-Wave Devices for Signal Processing*, ser. Studies in Electrical and Electronic Engineering. Elsevier Science Publishers, 1985, vol. 19.

[7] B. P. Abbott, "A coupling-of-modes model for SAW transducers with arbitrary reflectivity weighting," Ph.D. dissertation, University of Central Florida, 1989.

[8] D. Puccio, "Design, analysis and implementation of orthogonal frequency coding in SAW devices used for spread spectrum tags and sensors," Ph.D. dissertation, University of Central Florida, 2006.

[9] S. Mason, "Feedback theory-further properties of signal flow graphs," *Proceedings of the IRE*, vol. 44, no. 7, pp. 920 –926, july 1956.

[10] F. Duck, "The Electrical Expansion of Quartz by Jacques and Pierre Curie," *Ultrasound*, vol. 17, no. 4, pp. 197–203. [Online]. Available: http://dx.doi.org/10.1179/174227109X12500830049951

[11] L. Rayleigh, "On Waves Propagated along the Plane Surface of an Elastic Solid," *Proceedings of the London Mathematical Society*, November 1885.

[12] R. M. White and F. W. Voltmer, "Direct piezoelectric coupling to surface elastic waves," *Applied Physics Letters*, vol. 7, no. 12, pp. 314 –316, Dec. 1965.

[13] P. A. Hiltner and I. M. Krieger, "Diffraction of light by ordered suspensions," *The Journal of Physical Chemistry*, vol. 73, no. 7, pp. 2386–2389, July 1969. [Online]. Available: http://dx.doi.org/10.1021/j100727a049

[14] S. Wang, "Principles of distributed feedback and distributed bragg-reflector lasers," *Quantum Electronics, IEEE Journal of*, vol. 10, no. 4, pp. 413 – 427, Apr. 1974.

[15] R. Williamson, "Properties and applications of reflective-array devices," *Proceedings of the IEEE*, vol. 64, no. 5, pp. 702 – 710, may 1976.

[16] I. Shrena, D. Eisele, E. Mayer, L. Reindl, J. Bardong, and M. Schmitt, "SAW-properties of langasite at high temperatures: Measurement and analysis," in *Signals, Circuits and Systems (SCS), 2009 3rd International Conference on*, 2009, pp. 1 –4.

[17] X. Ren and X. Gong, "A wireless sensing technique using passive microwave resonators," in *Antennas and Propagation Society International Symposium, 2008. AP-S 2008. IEEE*, 2008, pp. 1 –4.

[18] J. C. Andle, S. Sabah, D. S. Stevens, S. J. Jumani, M. Baier, B. Wall, T. Martens, and R. Gruenwald, "Temperature monitoring system using passive wireless sensors for switchgear and power grid asset management," in *Transmission and Distribution Asset Management Workshop*, 2010.

[19] R. Steindi, C. Hausleitner, H. Hauser, and W. Bulst, "Wireless magnetic field sensor employing saw-transponder," in *Applications of Ferroelectrics, 2000. ISAF 2000. Proceedings of the 2000 12th IEEE International Symposium on*, vol. 2, 2000, pp. 855 –858 vol. 2.

[20] W.-E. Bulst, G. Fischerauer, and L. Reindl, "State of the art in wireless sensing with surface acoustic waves," in *IEEE Transactions on Industrial Electronics*, vol. 48, no. 2, 2001, pp. 265–271.

[21] F. Schmidt, O. Sczesny, L. Reindl, and V. Magori, "Remote sensing of physical parameters by means of passive surface acoustic wave devices ("id-tag")," in *Proc. IEEE Ultrasonics Symposium*, vol. 1, 1994, pp. 589–592 vol.1.

[22] A. Pohl, G. Ostermayer, L. Reindl, and F. Seifert, "Spread spectrum techniques for wirelessly interrogable passive SAW sensors," in *Proc. IEEE 4th International Symposium on Spread Spectrum Techniques and Applications*, vol. 2, 1996, pp. 730–734 vol.2.

[23] G. Ostermayer, A. Pohl, C. Hausleitner, L. Reindl, and F. Seifert, "CDMA for wireless SAW sensor applications," in *Proc. IEEE 4th International Symposium on Spread Spectrum Techniques and Applications*, vol. 2, 1996, pp. 795–799 vol.2.

[24] F. Schmidt, O. Sczesny, C. Ruppel, and V. Magori, "Wireless interrogator system for SAW-identification-marks and SAW-sensor components," in *Proc. IEEE International. Frequency Control Symposium 50th*, 1996, pp. 208–215.

[25] A. Pohl, "A review of wireless saw sensors," *Ultrasonics, Ferroelectrics and Frequency Control, IEEE Transactions on*, vol. 47, no. 2, pp. 317 –332, 2000.

[26] C. Hartmann, "A global saw id tag with large data capacity," in *Ultrasonics Symposium, 2002. Proceedings. 2002 IEEE*, vol. 1, 2002, pp. 65 – 69 vol.1.

[27] S. Harma, W. Arthur, C. Hartmann, R. Maev, and V. Plessky, "Inline saw rfid tag using time position and phase encoding," *Ultrasonics, Ferroelectrics and Frequency Control, IEEE Transactions on*, vol. 55, no. 8, pp. 1840 –1846, 2008.

[28] D. Malocha, D. Puccio, and D. Gallagher, "Orthogonal frequency coding for SAW device applications," in *Ultrasonics Symposium, 2004 IEEE*, vol. 2, 23-27 Aug. 2004, pp. 1082–1085Vol.2.

[29] J. Pavlina, N. Kozlovski, B. Santos, and D. Malocha, "SAW RFID spread spectrum OFC and TDM technology," in *Proc. IEEE International Conference on RFID*, 2009, pp. 110–116.

[30] J. H. Kuypers, S. Tanaka, M. Esashi, D. A. Eisele, and L. M. Reindl, "Passive 2.45 ghz tdma based multi-sensor wireless temperature monitoring system: Results and design considerations," in *Ultrasonics Symposium, 2006. IEEE*, 2006, pp. 1453 –1458.

[31] *Design of Global SAW RFID Tag Devices.* Second International Symposium on Acoustic Wave Devices for Future Mobile Communication Systems, Chiba University, March 2004.

[32] A. Pohl, G. Ostermayer, C. Hausleitner, F. Seifert, and L. Reindl, "Wavelet transform with a saw convolver for sensor application," in *Proc. IEEE Ultrasonics Symp.*, vol. 1, 1995, pp. 143–146.

[33] D. Malocha, N. Kozlovski, B. Santos, J. Pavlina, M. Belkerdid, and T. Mears, "Ultra wide band surface acoustic wave (SAW) RF ID tag and sensor," in *Military Communications Conference, 2009. MILCOM 2009. IEEE*, 2009, pp. 1 –7.

[34] D. Puccio, D. Malocha, D. Gallagher, and J. Hines, "SAW sensors using orthogonal frequency coding," in *Proc. 2004 IEEE International Frequency Control Symposium and Exposition*, 2004, pp. 307–310.

[35] D. Puccio, D. C. Malocha, N. Saldanha, D. R. Gallagher, and J. H. Hines, "Orthogonal frequency coding for SAW tagging and sensors," *IEEE Transactions on Ultrasonics, Ferroelectrics, and Frequency Control*, vol. 53, no. 2, pp. 377–384, 2006.

[36] N. Kozlovski and D. Malocha, "SAW noise-like anti-collision code study," in *Proc. Joint with the 22nd European Frequency and Time forum Frequency Control Symposium IEEE International*, 2009, pp. 616–621.

[37] H. Kogelnik, "Coupled wave theory for thick hologram gratings," *The Bell System Technical Journal, Vol.˜48, no.˜9, November 1969, pp.˜2909-2947*, vol. 48, pp. 2909–2947, November 1969.

[38] H. Kogelnik and C. V. Shank, "Coupled-Wave Theory of Distributed Feedback Lasers," *Journal of Applied Physics*, vol. 43, no. 5, pp. 2327–2335, 1972.

[39] H. Haus and P. Wright, "The analysis of grating structures by coupling-of-modes theory," in *1980 Ultrasonics Symposium*, 1980, pp. 277 – 281.

[40] D.-P. Chen and H. Haus, "Analysis of metal-strip saw gratings and transducers," *Sonics and Ultrasonics, IEEE Transactions on*, vol. 32, no. 3, pp. 395 – 408, May 1985.

[41] David Morgan, *Surface Acoustic Wave Filters*, 2nd ed. Academic Press, 2007.

[42] David M. Pozar, *Microwave Engineering*, 3rd ed. Wiley, 2004.

[43] C.-S. Kee, J.-E. Kim, H. Y. Park, K. J. Chang, and H. Lim, "Essential role of impedance in the formation of acoustic band gaps," *Journal of Applied Physics*, vol. 87, pp. 1593–1596, Feb. 2000.

[44] S. Yang, J. H. Page, Z. Liu, M. L. Cowan, C. T. Chan, and P. Sheng, "Ultrasound tunneling through 3d phononic crystals," *Physical Review Letters*, vol. 88, no. 10, pp. 104 301–+, Mar. 2002.

[45] V. Laude, M. Wilm, S. Benchabane, and A. Khelif, "Full band gap for surface acoustic waves in a piezoelectric phononic crystal," *pre*, vol. 71, no. 3, pp. 036 607–+, Mar. 2005.

[46] S. Benchabane, A. Khelif, J.-Y. Rauch, L. Robert, and V. Laude, "Evidence for complete surface wave band gap in a piezoelectric phononic crystal," *pre*, vol. 73, no. 6, pp. 065 601–+, Jun. 2006.

[47] A. Khelif, A. Choujaa, S. Benchabane, B. Djafari-Rouhani, and V. Laude, "Guiding and bending of acoustic waves in highly confined phononic crystal waveguides," *Applied Physics Letters*, vol. 84, pp. 4400–+, May 2004.

[48] T.-T. Wu, H.-T. Tang, Y.-Y. Chen, and P.-L. Liu, "Analysis and design of focused interdigital transducers," *Ultrasonics, Ferroelectrics and Frequency Control, IEEE Transactions on*, vol. 52, no. 8, pp. 1384–1392, Aug. 2005.

[49] Y. Nelin, "Apodized phononic crystals," in *Ultrasonics Symposium, 2005 IEEE*, vol. 1, 18-21 Sept. 2005, pp. 62–64.

[50] K.-B. Gu, C.-L. Chang, J.-C. Shieh, and W.-P. Shih, "Design and fabrication of 2d phononic crystals in surface acoustic wave micro devices," in *Micro Electro Mechanical Systems, 2006. MEMS 2006 Istanbul. 19th IEEE International Conference on*, 2006, pp. 686–689.

[51] V. Laude, L. Robert, W. Daniau, A. Khelif, and S. Ballandras, "Surface acoustic wave trapping in a periodic array of mechanical resonators," *Applied Physics Letters*, vol. 89, pp. 3515–+, Aug. 2006.

[52] L. Dhar and J. A. Rogers, "High frequency one-dimensional phononic crystal characterized with a picosecond transient grating photoacoustic technique," *Applied Physics Letters*, vol. 77, pp. 1402–+, Aug. 2000.

[53] N. Kozlovski and D. Malocha, "Saw noise-like coded reflector structures," in *Proc. IEEE International Frequency Control Symposium*, 2008, pp. 290–295.

[54] J. Flood, "Crosstalk in time-division-multiplex communication systems using pulse-position and pulse-length modulation," *Proceedings of the IEE - Part IV: Institution Monographs*, vol. 99, no. 2, pp. 64 –73, April 1952.

[55] H. S. Hall and S. R. Knight, *Higher Algebra: a Sequel to Elementary Algebra for Schools*. Adamant Media Corporation, 2001.

[56] J. K. Patel and C. B. Read, "Handbook of the normal distribution," 1982.

[57] B. M. C. Santos, "SAW reflective transducers and antennas for orthogonal frequency coded SAW sensors," Master's thesis, University of Central Florida, 2009.

[58] M. Gallagher, B. Santos, and D. Malocha, "Wireless Wideband SAW Sensor - Antenna Design," in *Frequency Control Symposium (FCS), 2010 IEEE International*, 2010, pp. 291 –296.

[59] J. B. Y. Tsui, *Digital techniques for wideband receivers*, 2nd ed. Norwood, MA, USA: Artech House, Inc., 2001.